

JAERI-Research
95-070



PHYSICS DESIGN OF AN ICRF SYSTEM FOR ITER

November 1995

Haruyuki KIMURA, Tsuneyuki FUJII, Atsushi FUKUYAMA*, Mikio SAIGUSA
Shinichi MORIYAMA and Kiyotaka HAMAMATSU

日本原子力研究所
Japan Atomic Energy Research Institute

本レポートは、日本原子力研究所が不定期に公刊している研究報告書です。

入手の間合わせは、日本原子力研究所技術情報部情報資料課（〒319-11 茨城県那珂郡東海村）あて、お申し越してください。なお、このほかに財団法人原子力弘済会資料センター（〒319-11 茨城県那珂郡東海村日本原子力研究所内）で複写による実費頒布をおこなっております。

This report is issued irregularly.

Inquiries about availability of the reports should be addressed to Information Division, Department of Technical Information, Japan Atomic Energy Research Institute, Tokai-mura, Naka-gun, Ibaraki-ken 319-11, Japan.

© Japan Atomic Energy Research Institute, 1995

編集兼発行 日本原子力研究所

印刷 ㈱原子力資料サービス

Physics Design of an ICRF System for ITER

Haruyuki KIMURA, Tsuneyuki FUJII⁺¹, Atsushi FUKUYAMA*
Mikio SAIGUSA⁺², Shinichi MORIYAMA⁺¹
and Kiyotaka HAMAMATSU⁺³

Department of ITER Project
Naka Fusion Research Establishment
Japan Atomic Energy Research Institute
Naka-machi, Naka-gun, Ibaraki-ken

(Received October 4, 1995)

The fast wave current drive performance is studied in detail both for the in-blanket antenna and the in-port antenna for ITER, using a variety of full wave codes (Task-W1, Task-WM, etc.). The low frequency scenario ($f = 20 \text{ MHz} < f_{ce}$) with the in-blanket antennas suffers from the $N_{||}$ upshift because of a weak damping per pass and an insufficient directivity even with the 18 strap array. The current drive efficiency can be improved with increasing safety factor at the expense of the damping per pass. On the other hand, the high frequency scenario ($f \sim 60 \text{ MHz} \geq 2f_{ce}$) shows better current drive performance because of a strong damping per pass and much more narrow current spectrum, in spite of a loss of certain amount of power to ions ($\sim 20\%$). The in-port antenna with 'tangential access' is proposed, aiming at compatibility of high performance on the current drive and easy maintenance. 8 strap array with total toroidal extension of about 3 m is possible with reasonable power injection capability, i.e., a total injection power of 100 MW using 6 ports. The current drive figure of merit is calculated to be $\sim 0.2 \times 10^{20} \text{ AW}^{-1} \text{ m}^{-2}$ by 1-D code or $\sim 0.3 \times 10^{20} \text{ AW}^{-1} \text{ m}^{-2}$ by 2-D code taking account of realistic ITER plasma equilibrium in ignition. The current drive efficiency is comparable to that of the in-blanket antenna using the low frequency scenario. Conceptual drawing of the in-port antenna which utilizes ridged waveguide supports for central conductors is presented.

⁺¹ Department of Fusion Facility

⁺² Department of Fusion Engineering Research

⁺³ Department of Fusion Plasma Research

* Okayama University

Keywords: ITER, ICRF, Fast Wave Current Drive, In-blanket Antenna, In-port Antenna, Full Wave Code, Current Drive Efficiency, Plasma Equilibrium, Ridged Waveguide Support, Antenna Array

ITERのためのICRFシステムの物理設計

日本原子力研究所那珂研究所 ITER開発室

木村 晴行 ・ 藤井 常幸⁺¹ ・ 福山 淳* ・ 三枝 幹雄⁺²
森山 伸一⁺¹ ・ 浜松 清隆⁺³

(1995年10月4日受理)

ITERの二つのICRFアンテナ概念、即ちブランケット内アンテナ及びポート内アンテナについて速波電流駆動の性能が種々の波動解析コード(Task-W1, Task-WM等)を用いて詳細に検討される。ブランケット内アンテナに対する低周波数シナリオ($f = 20\text{MHz} < f_{ce}$)は弱い波動吸収による N_{\parallel} アップシフトと18素子のアンテナアレイによってさえも不十分な方向性により悪影響を受ける。電流駆動効率はトカマクの安全係数を上げることににより波動吸収率は犠牲になるものの改善が可能である。一方、高周波数シナリオ($f \sim 60\text{MHz} \geq 2f_{ce}$)はある程度($\sim 20\%$)のイオンへのパワー損失はあるものの、強い波動吸収とよりシャープなアンテナ電流スペクトルにより、むしろ良好な電流駆動性能が得られる。高性能な電流駆動特性と保守の容易さの両立を狙った‘接線アクセス’によるポート内アンテナが提案される。トロイダル方向の全幅3mの8素子のアンテナアレイが可能であり、6ポート当り100MWと妥当な電力入射性能を有する。電流駆動効率は1次元コードで $\sim 0.2 \times 10^{20} \text{AW}^{-1} \text{m}^{-2}$ 、ITERの自己点火時のプラズマ平衡を取り入れた2次元コードで $\sim 0.3 \times 10^{20} \text{AW}^{-1} \text{m}^{-2}$ と計算される。中心導体のリッジ導波管支持を適用したポート内アンテナの概念設計図が示される。

那珂研究所：〒311-01 茨城県那珂郡那珂町向山801-1

- +1 核融合装置試験部
- +2 核融合工学部
- +3 炉心プラズマ研究部
- * 岡山大学

Contents

1. Introduction	1
2. Physics Design on Current Drive	3
2.1 Calculation Method	3
2.2 Calculation Parameters	6
2.3 Operating Frequency	8
2.4 In-blanket Antennas	10
2.4.1 Low Frequency Scenario	10
2.4.2 High Frequency Scenario	23
2.4.3 Summary	38
2.5 In-port Antennas	39
2.5.1 Optimum Frequency for FWCD	39
2.5.2 Antenna Configuration	42
2.5.2.1 Perpendicular Access	42
2.5.2.2 Tangential Access	47
2.5.3 Current Drive in OH Conditions	52
2.5.4 Effect of Triton Tail Formation	54
2.5.5 Two-dimensional Calculation	57
2.5.6 Concept of Antenna Structure	64
2.5.7 Antenna-plasma Coupling Calculation	69
2.5.8 Summary	75
3. Concluding Remarks	76
Acknowledgment	77
References	78

目 次

1. 序 論	1
2. 電流駆動に関する物理設計	3
2.1 計算モデル	3
2.2 計算パラメータ	6
2.3 運転周波数	8
2.4 ブランケット内アンテナ	10
2.4.1 低周波数シナリオ	10
2.4.2 高周波数シナリオ	23
2.4.3 ま と め	38
2.5 ポート内アンテナ	39
2.5.1 速波電流駆動のための最適周波数	39
2.5.2 アンテナ配位	42
2.5.2.1 垂直アクセス	42
2.5.2.2 接線アクセス	47
2.5.3 OH条件での電流駆動	52
2.5.4 三重水素の高エネルギーテイル形成の効果	54
2.5.5 2次元計算	57
2.5.6 アンテナの概念構造	64
2.5.7 アンテナープラズマ結合計算	69
2.5.8 ま と め	75
3. 結 語	76
謝 辞	77
参考文献	78

1. Introduction

Physics requirements of the Ion Cyclotron Range of Frequencies (ICRF) Heating and Current Drive System for ITER were defined at the technical meeting on RF Heating and Current Drive held in Garching Co-center in October, 1993. On the basis of the requirements, ICRF heating and current drive scenarios were selected, such as bulk plasma heating via tritium second harmonic heating, central current drive via electron Landau damping and transit time magnetic pumping (TTMP), local current profile control via minority ion current drive, etc.. Then a wide frequency range, i.e., 20-70/90 MHz, was recommended to fulfill them. The frequency range was similar to that of the ITER CDA ICRF design [1]. The lower limit of the frequency band (20MHz) was determined by the requirement for the current drive, because such a low frequency can exclude any ion cyclotron resonance layer inside the plasma cross-section and was believed to give the best current drive efficiency. The upper limit of the frequency band (90MHz) was determined by the requirement for heating non-reacting plasmas. Between them, several important frequencies for heating and current drive exist.

According to the choice of the frequency band, an interesting proposal for the antenna concept, so called 'violin antenna' [2], was presented from Europe at the meeting mentioned above. The antenna concept utilizes a half wavelength resonance at 20MHz to give a sufficient antenna-plasma coupling even at such a low frequency. Higher harmonics can be used for upper important frequencies for heating and current drive. Although a size of the current strap should be very large (3m in length) for this purpose, the current strap is mechanically fixed to the antenna casing at both top and bottom ends and so it can be strong enough against electromagnetic forces at plasma disruptions. In order to have a sharp N_z spectrum for the current drive, a number of current straps should be arranged in the toroidal direction with equal spacing. For this purpose, the antennas are installed not only in horizontal ports but also in blanket segments. Accordingly, the antenna concept is called as 'in-blanket antenna'. Outline design of the in-blanket antenna was presented by the ITER Joint Central Team (JCT) at the 4th meeting of the Technical Advisory Committee [3] and at the 15th IAEA Conference in Seville [4]. It was reported that the current drive figure of merit γ is not so high ($\gamma=0.15\sim0.3\times10^{20}\text{AW}^{-1}\text{m}^{-2}$) even with the 18 strap array [3].

The first half of this report deals with the physics study on the in-blanket antennas, aiming at optimization of the current drive. Both the low frequency scenario (20MHz) and the high frequency scenario (~65MHz) are discussed. It is found that the current drive efficiency of the low frequency scenario is improved with increasing safety factor, but that the high frequency scenario has better current drive performance for the 18 strap array.

Recently, the design of the blankets has been changed to consist of poloidally segmented modules. This implies that the in-blanket antenna concept mentioned above is no longer applicable. Also maintainability of the antennas has been a matter of primary concern. Thus an in-port antenna concept, such that an antenna plug can be installed through a horizontal port for easy maintenance, has come up in stead of the in-blanket antenna. The current drive scenario is restricted to the high frequency, because the directivity of the in-port antenna with limited toroidal width is too poor at 20MHz. In CDA, a high-frequency ICRF system that utilizes an in-port antenna concept was proposed from Japan with emphasis on the maintainability [1,5]. Japan has also a lot of experiences on design, construction and operation of in-port antennas on JT-60 [6,7] and JT-60U [8-12].

In the latter half of this report, physics study on the in-port antenna is presented. First, current drive and heating characteristics of the in-port antenna based on the JCT proposal are evaluated. Then new proposal for the in-port antenna of 'tangential access' is presented for improving both current drive efficiency and controllability in heating. It is shown that the current drive efficiency comparable with those of the in-blanket antenna can be obtained with the in-port antenna of tangential access. Conceptual drawing of the antenna structure which utilizes ridged waveguide supports for central conductors is presented. Preliminary study on the antenna-plasma coupling is also made.

2. Physics Design on Current Drive

2.1 Calculation method

To obtain the driven current by fast waves, we must estimate a wave electric field in a plasma, which is described by the following equation,

$$\nabla \times \nabla \times \mathbf{E} - \frac{\omega^2}{c^2} \tilde{\epsilon} \mathbf{E} = i \omega \mu_0 \mathbf{J}_{\text{ext}}, \quad (2.1-1)$$

where \mathbf{E} is the wave electric field vector, $\tilde{\epsilon}$ is the dielectric tensor and \mathbf{J}_{ext} is the external current flow in an antenna current strap. We can solve the wave electric field as a boundary value problem. Then we estimate the absorbed power by electrons, and therefore the driven current by multiplying the absorbed power by the current drive efficiency. Here we use the expression for the current drive efficiency given by D. A. Ehst [13], which is presented as a function of the ratio of phase velocity to the electron thermal velocity, the inverse aspect ratio and the poloidal angle. We use three codes to solve the electric field with different plasma models, where the parallel wave-particle interaction is described exactly with the plasma dispersion function and the perpendicular interaction (finite Larmor radius effect) is approximated with the perpendicular wave number which is calculated from the cold plasma dispersion. One code is a one-dimensional (1-D) full wave code for a slab plasma [14], in which inhomogeneous toroidal field is taken account of as the following expression,

$$B(x) = B_0 / (1 + x/R_0), \quad (2.1-2)$$

where B_0 is the magnetic field strength on the axis and R_0 is the major radius. This code has been combined with a Fokker-Planck code by K. Hamamatsu et al. [15] so that we can estimate ion tail formation by ICRF heating or calculate ICRF power absorption by high energy ions generated in fusion reactions.

But this 1-D code may not treat the focusing of the electric field due to the wave refraction and the change in the poloidal wavelength. Then A. Fukuyama et al. have developed a two-dimensional (2-D) full wave code for a toroidal plasma in the cylindrical coordinates (R ,

Z, ϕ) [16], and further they have improved it to employ the toroidal coordinates (r, θ, ϕ) for a toroidal plasma with a circular cross section. The magnetic field components are given as

$$B_\phi(r, \theta) = B_0 / (1 + r \cos\theta / R_0) \quad (2.1-3)$$

$$B_\theta(r, \theta) = -r B_\phi(r, \theta) / R_0 q(r), \quad (2.1-4)$$

where the safety factor is assumed to be parabolic

$$q(r) = (q_0 - q_a) \{1 - (r/a)^2\} + q_a. \quad (2.1-5)$$

Here q_0 is the central safety factor and q_a is the surface safety factor. In this 2-D code, the change in parallel wavelength in the poloidal cross section due to the toroidal effect, which substantially changes the current drive efficiency, is taken into account by the expansion on the poloidal mode number. So that we expand the wave electric field and the external current in a Fourier series as

$$\mathbf{E}(r) = \sum_m \mathbf{E}_m(r) \exp[i(m\theta + n\phi)], \quad (2.1-6)$$

$$\mathbf{J}_{\text{ext}}(r) = \sum_m \mathbf{J}_{\text{ext},m}(r) \exp[i(m\theta + n\phi)], \quad (2.1-7)$$

where m is the poloidal mode number and n is the toroidal mode number. Substituting Eqs. (2.1-6) and (2.1-7) into Eq. (2.1-1), we have a series of differential equations and we solve them by the difference method or the finite element method. In a cylindrical plasma, the dielectric tensor is independent of θ so that no coupling between the modes with different poloidal mode number. But we must solve the wave equation for all the poloidal modes simultaneously for a toroidal plasma.

In the third model, we employ the magnetic surface coordinates (ψ, χ, ϕ) in order to describe a toroidal plasma with a non-circular cross section. We can analyze the fast wave

propagation and current drive for plasma configurations that are estimated by an equilibrium code. The data of the magnetic surface $\psi(R, Z)$ are calculated by the equilibrium code and transferred to the 2-D code. Then the cylindrical coordinate (R, Z, ϕ) is transformed into the magnetic surface coordinate (ψ, χ, ϕ) in the 2-D code in order to calculate the fast wave propagation.

2.2 Calculation parameters

Calculation parameters used for estimate of the current drive efficiency are listed in Tables 2.2-1 and 2.2-2, corresponding to CD phase and OH phase, respectively.

In the 1-D code the number of meshes in the x-direction is 400 so that its space resolution is fairly sufficient.

In the 2-D code, the number of meshes is 100 in the radial direction and 32 in the poloidal direction. The poloidal mode number is from -15 to 15 so that the number of poloidal modes is 31 modes. The antenna position in the poloidal direction is from -15° to 15° for an in-port antenna and from -55° to -8.5° for an in-blanket antenna.

Table 2.2 -1 Calculation parameters for CD conditions

major radius	8 m
minor radius	3 m
antenna position	3.2 m
wall position	3.5 m
toroidal field on axis	5.81 T
central electron temperature	27 keV
central ion temperature	27 keV
temperature profile	$T(r) = (T_0 - T_s) \{ 1 - (r/a)^2 \}^2 + T_s$
edge temperature	0.3 keV
central electron density	$1.4 \times 10^{20} \text{ m}^{-3}$
central deuterium density	$0.518 \times 10^{20} \text{ m}^{-3}$
central tritium density	$0.518 \times 10^{20} \text{ m}^{-3}$
central helium density	$0.14 \times 10^{20} \text{ m}^{-3}$
central beryllium density	$0.014 \times 10^{20} \text{ m}^{-3}$
density profile	$n(r) = (n_0 - n_s) \{ 1 - (r/a)^2 \}^{0.15} + n_s$
edge electron density	$0.6 \times 10^{20} \text{ m}^{-3}$
effective charge (Z_{eff})	1.32
central safety factor	1.0
surface safety factor	3.0

Table 2.2 -2 Calculation parameters for OH conditions

major radius	8.1 m
minor radius	3 m
antenna position	3.2 m
wall position	3.5 m
toroidal field on axis	5.74 T
central electron temperature	9.25 keV
central ion temperature	8.75 keV
temperature profile	$T(r) = (T_0 - T_s) \{ 1 - (r/a)^4 \}^3 + T_s$
edge temperature	0.3 keV
central electron density	$0.25 \times 10^{20} \text{ m}^{-3}$
central deuterium density	$0.0829 \times 10^{20} \text{ m}^{-3}$
central tritium density	$0.166 \times 10^{20} \text{ m}^{-3}$
central beryllium density	$0.00125 \times 10^{20} \text{ m}^{-3}$
density profile	$n(r) = (n_0 - n_s) \{ 1 - (r/a)^2 \}^{0.15} + n_s$
edge electron density	$0.15 \times 10^{20} \text{ m}^{-3}$
effective charge (Z_{eff})	1.46
central safety factor	1.0
surface safety factor	3.0

2.3 Operating frequency

Figure 2.3-1 shows various ion cyclotron resonance positions for ITER plasmas against frequency for $B_t = 5.81$ T at $R_0 = 8$ m. There is no ion cyclotron resonance below 20 MHz so that this low frequency range is one of suitable frequency for the fast wave current drive. We call this current drive scheme as 'the low frequency scenario'. But the single pass power absorption is predicted to be relatively small in the low frequency range. One of strong on-axis heating schemes is 45 MHz of the fundamental deuterium resonance. In a frequency range of 30 - 50 MHz the mode conversion from the fast wave to the ion Bernstein wave can occur at off-axis region so that it is one of possible schemes for the current profile control. The second harmonic tritium resonance is located near on-axis for a frequency range of 60 MHz. As discussed in section 2.5, however, this frequency is quite effective for the fast wave current drive with relatively low parallel refractive index, $N_{||} = 2 - 3$ for CD conditions because most of wave power is absorbed by electrons in calculations by both the 1-D and the 2-D codes. Thus, this higher frequency range of 60 MHz is favorable for both the in-port antenna and the in-blanket antenna. We call this current drive scheme as 'the high frequency scenario'. The second harmonic deuterium resonance, however, appears at the low field side above 65 MHz, and it shifts to the magnetic axis at about 90 MHz. The resonance is also the α particle second harmonic resonance so that the main species of the wave power absorption rapidly changes from electrons to high energy α particles. As it is the hydrogen fundamental resonance, a frequency range of 90 MHz is an effective on-axis heating scheme for deuterium plasmas and hydrogen plasmas (non-reacting plasmas).

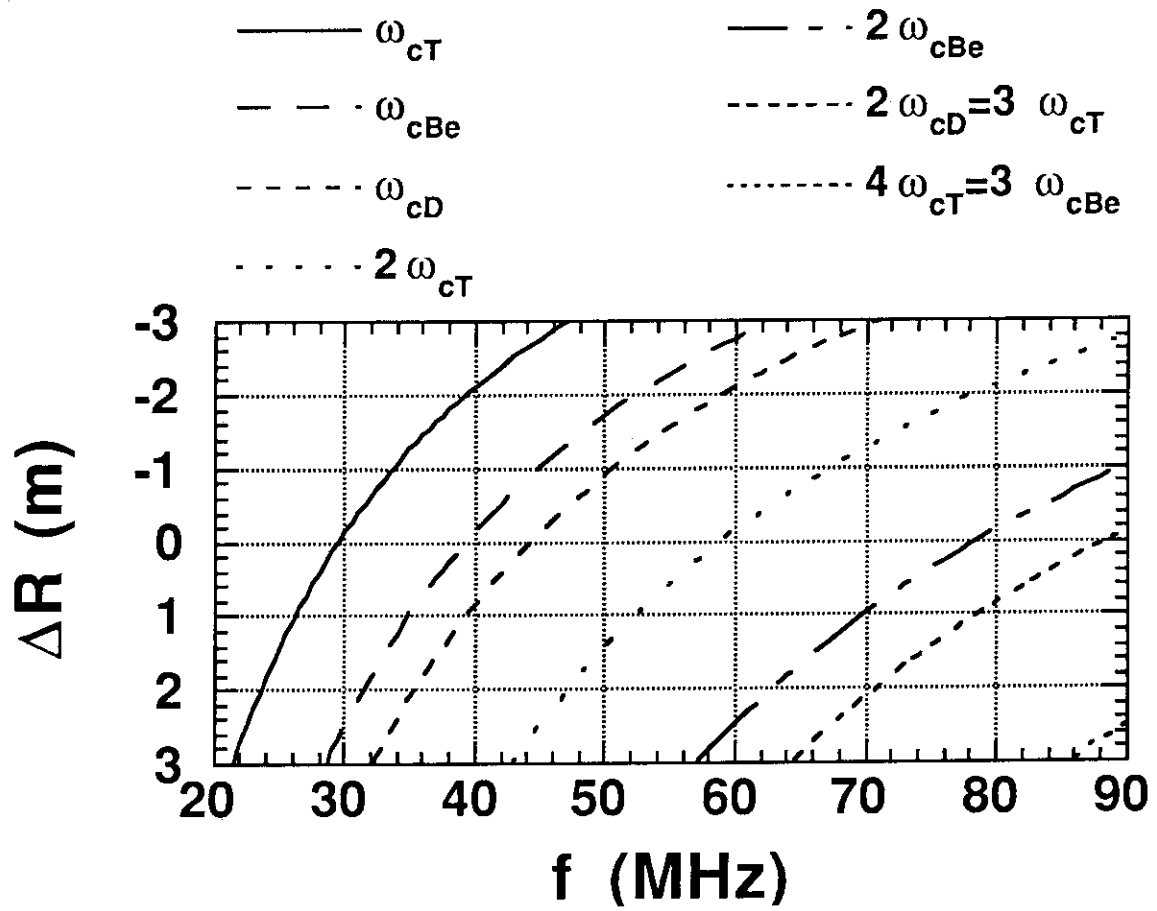


Figure 2.3-1 Ion cyclotron resonance layer position against frequency for ITER. The toroidal field is assumed to be 5.81T at the plasma center ($R_0 = 8\text{m}$).

2.4 In-blanket antennas

2.4.1 Low frequency scenario

Propagation and absorption of fast waves, and resultant power deposition and driven current profiles are investigated for the low frequency scenario ($f=20\text{MHz} < f_{cT}$). Then methods of optimizing the current drive efficiency are pursued. It is found that broadening density profile and increasing safety factor improve the current drive efficiency significantly.

Calculation model

Here, we employ the 2-D full wave code assuming a circular plasma cross-section and a parabolic profile of the safety factor,

$$q(r) = (q_0 - q_a) (1 - (r/a)^2) + q_a \quad (2.4-1)$$

The electron density profile is given by

$$n_e(r) = (n_{e0} - n_{es}) (1 - (r/a)^2)^{\alpha_N} + n_{es} \quad (2.4-2)$$

We take $q_a=5$, $q_0=1$ and $\alpha_N=2$ as a standard parameter set for CD conditions (see Table 2.2-1) here.

The trapped electron effect on the current drive efficiency is taken into account by employing the fitting formula proposed by Ehst et al. [13]. The poloidal angle of the in-blanket antenna (off-midplane launching) is assumed to be from -55° to -8.5° . We also calculate in some cases with midplane launching for comparison. In this case, the poloidal angle extends from -23° to 23° . The current drive figure of merit γ is defined by $\gamma = I_{CD} \langle n_e \rangle R / P_{IC}$, where I_{CD} is the driven current, $\langle n_e \rangle$ the volume average electron density, R the major radius and P_{IC} the ICRF power. In calculations, number of the radial mesh and poloidal mode numbers are taken to be 100 and $-15 \sim 15$ (in total, 31 modes), respectively.

Wave propagation and absorption

Figures 2.4.1-1~3 show the calculation results for $n=5$ (toroidal refractive index $N_z=1.5$) and off-midplane launching. The parallel refractive index $N_{||}$ is given by

$$N_{||} = (n + m/q) c / (\omega R) \quad (2.4-3)$$

where ω is the angular frequency. With increasing poloidal mode number, $N_{||}$ increases and the electron power absorption becomes stronger. If m is negative, then $N_{||}$ decreases and the electron power absorption becomes weaker. Near the plasma center ($q \sim 1$), no electron absorption occurs for $-9 < m < -3$ because of $|N_{||}| < 1$. A spatial profile of the wave electric field (E_θ) and its mode distribution are shown in Fig. 2.4.1-1. As the wave absorption is weak because of low $N_{||}$, standing waves are formed due to multi-reflection. It is shown that low $N_{||}$ components are excited in the peripheral region by the antenna and that $N_{||}$ becomes larger in propagating toward the central region. A spatial profile of the electron power absorption and its mode distribution are shown in Fig. 2.4.1-2. It is found that $N_{||} \sim 2$ components are absorbed near the center where the electron temperature is the highest. Radial profiles of the electron absorption power and the driven current are shown in Fig. 2.4.1-3. The driven current profile is more peaked than the absorption power profile, because the current drive efficiency is higher near the center due to higher temperature and less trapped particle effect. An affect of the standing waves appears even in the radial profile averaged over a magnetic surface. A value of γ is $0.3 \times 10^{20} \text{ AW}^{-1} \text{ m}^{-2}$ in this case. We also calculated for the case of midplane launching. A difference is very small (a few percent in γ) between the midplane launching and the off-midplane launching. We have not yet checked whether it is due to the circular plasma cross-section adopted here.

Dependence on the toroidal mode number

Figure 2.4.1-4 shows γ as a function of the toroidal mode number. γ increases with decreasing n down to $n=6$ and it is almost constant for $n=4 \sim 6$. The reason is due to $N_{||}$ upshift associated with increase in the poloidal mode number m , because the wave absorption is weak. The $N_{||}$ upshift occurs over a wide range of the minor radius, resulting in broadening of the

electron power absorption profile. Then the current drive efficiency is degraded by the trapped electron effect in the outer region.

Improvement of the current drive efficiency

In order to improve the current drive efficiency, $N_{||}$ upshift should be avoided. Possible countermeasure is to increase the safety factor as understood from Eq. (2.4-3). Figure 2.4.1-5 shows γ as a function of q_a with q_0 fixed at 1. Circles represent a case of $\alpha_N=2$ and triangles a case of $\alpha_N=0.15$. γ increases monotonically with increasing q_a . Values of γ with $\alpha_N=0.15$ are about 20% higher than those with $\alpha_N=2$. Thus, higher safety factor and broader density profile make the current drive efficiency be improved significantly. Figure 2.4.1-6 indicates how γ increases with broadening the density profile. Here, the density profile peaking factor $n_{e0}/\langle n_e \rangle$ is given by

$$\frac{n_{e0}}{\langle n_e \rangle} = \frac{(1 + \alpha_N)n_{e0}}{n_{e0} + \alpha_N n_{es}} \quad (2.4-4)$$

Although the density profile changes, the power absorption profile changes only slightly. For example, peak position of the power deposition profile are $\sim 0.5\text{m}$ for $\alpha_N=2.0$ ($n_{e0}/\langle n_e \rangle=1.62$) and $\sim 0.8\text{m}$ for $\alpha_N=0.15$ ($n_{e0}/\langle n_e \rangle=1.08$). Therefore γ is improved with broadening the density profile.

γ is further improved with increasing q_0 . Figure 2.4.1-7 shows γ as a function of q_0 with fixed q_a . Circles represent a case of $q_a=7$ and triangles a case of $q_a=9$. The highest value of γ ($\sim 0.48 \times 10^{20} \text{AW}^{-1}\text{m}^{-2}$) is obtained at $q_a=7\sim 9$ and $q_0=2\sim 3$ with $\alpha_N=0.15$. The current drive efficiency of the low frequency scenario is thus optimized.

Calculation for the optimum condition (high -q)

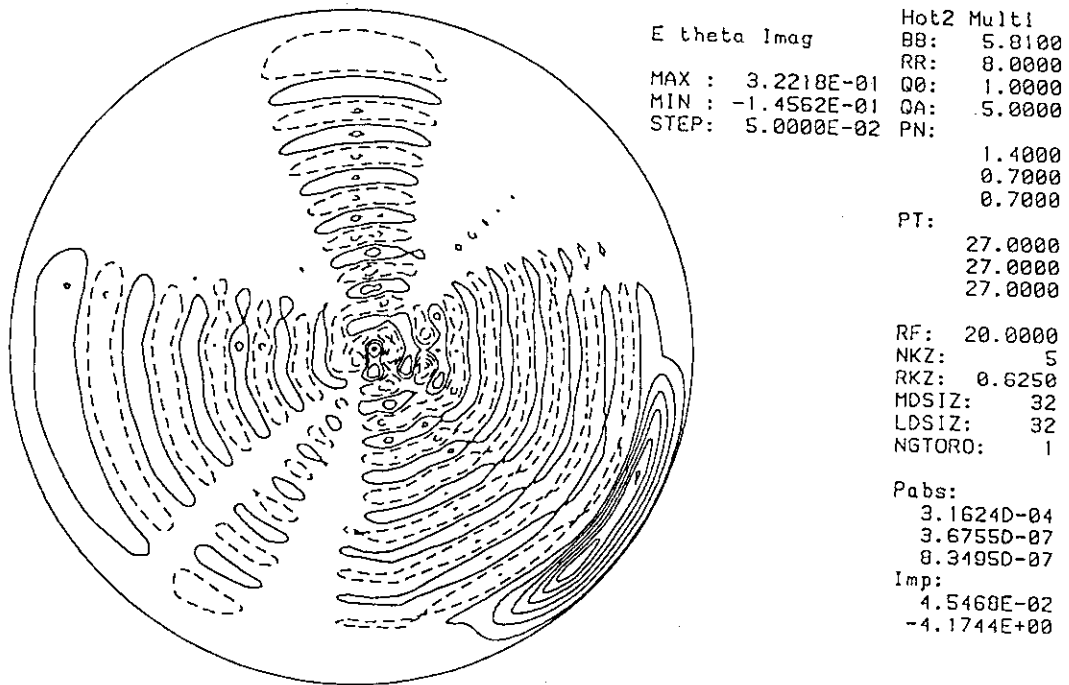
Figures 2.4.1-8~10 show the calculation results for the optimum conditions ($q_a=7$, $q_0=2.5$ and $\alpha_N=0.15$) with $n=5$ (toroidal refractive index $N_z=1.5$) and off-midplane launching. Because of minimization of $N_{||}$ upshift due to high q -value, standing waves are more prominently formed than those for the standard conditions. The absorbed power and driven current profiles are more narrower than those for the standard conditions although the electron

density profile is much broader. The γ value is $0.48 \times 10^{20} \text{AW}^{-1} \text{m}^{-2}$, which is about 60% higher than that for the standard conditions. In this scheme, the current drive efficiency is optimized at the expense of the single pass absorption. More prominent undulation due to the cavity resonance is seen in the radial profile of the electron power absorption and the driven current (Fig. 2.4.1-10). The current drive efficiency takes the maximum when the cavity resonance appears. The frequency feedback control would be necessary to track the cavity resonance and to maximize the current drive efficiency [17].

Antenna current spectrum

In the above analyses, the current drive efficiency is evaluated with a single toroidal mode number. The antenna current spectrum of the 18 strap array of the in-blanket antenna at 20MHz with a peak position of the main lobe of $N_z=1.5$ is shown in Fig. 2.4.1-11. The spectrum is not sufficiently sharp for the current drive operation at 20MHz, since it extends largely below $N_z < 1$. If the antenna spectrum were taken into account, then reduction of γ would be about 25%.

(a)



(b)

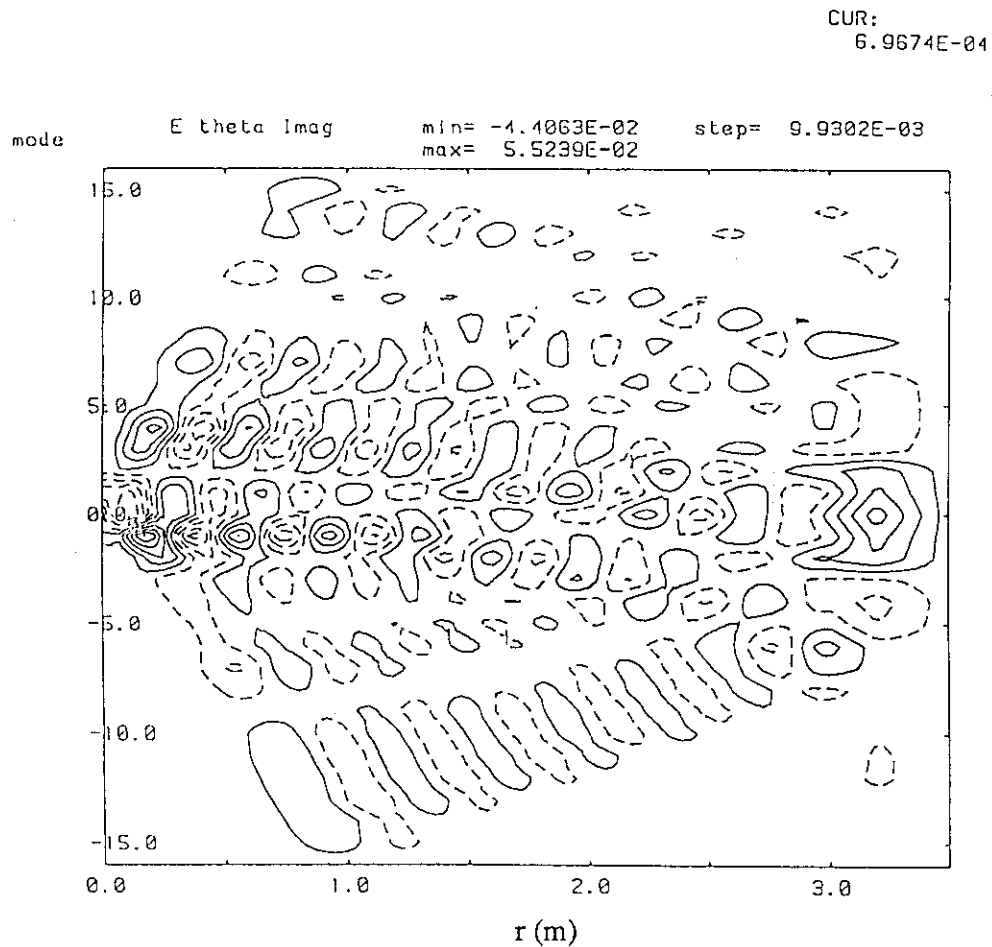
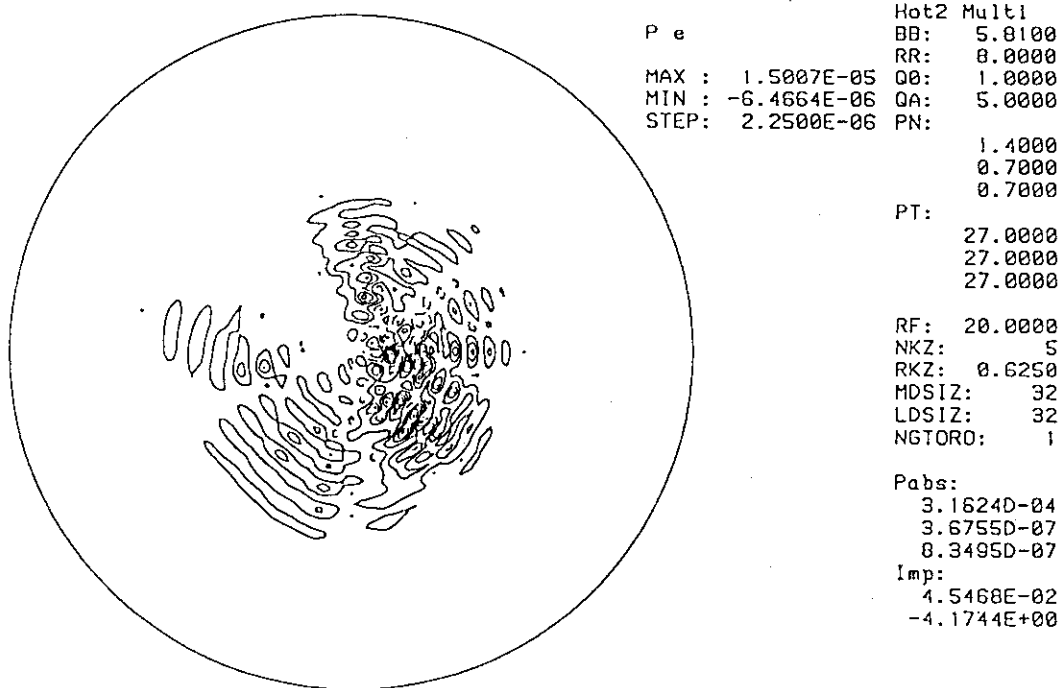
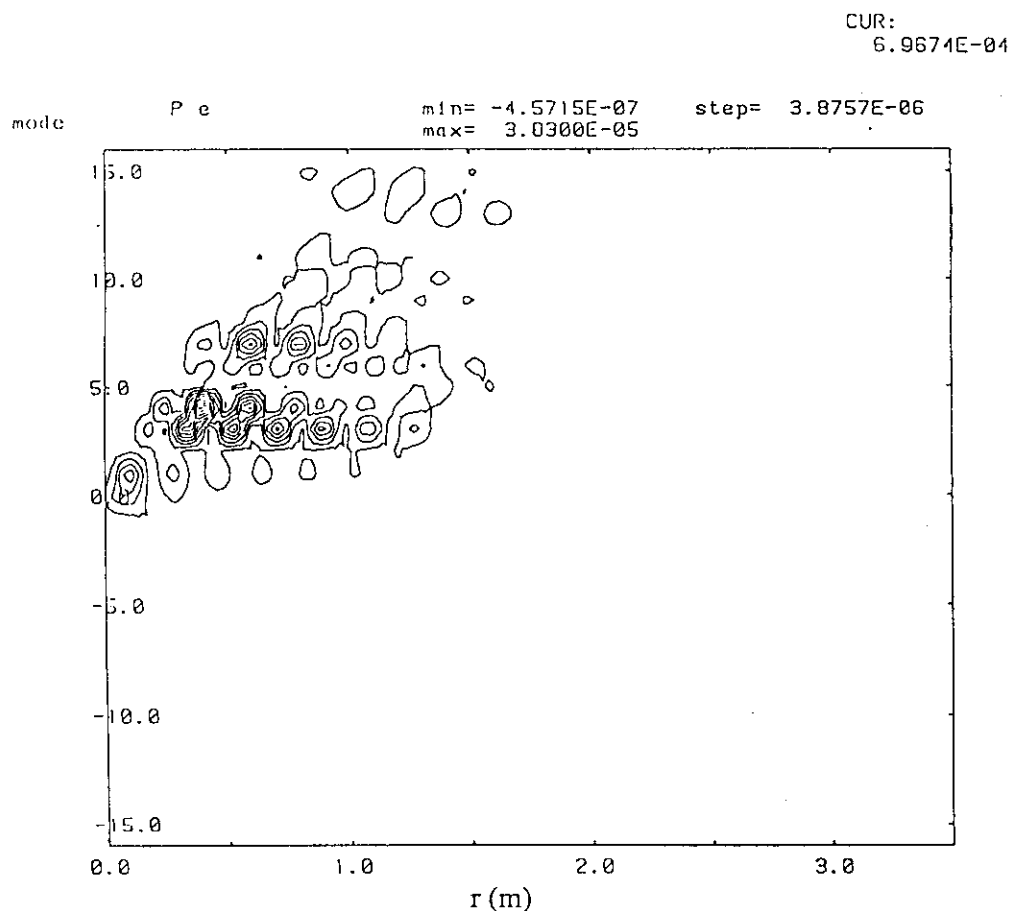


Fig. 2.4.1-1 Contour plots of the wave electric field (E_θ) (a) in the poloidal cross-section and (b) in a plane defined by the poloidal mode number and the minor radius. 20MHz, $n=5$, $q_a=5$, $q_0=1$, $\alpha_N=2$, in-blanket antenna (off-midplane launching) and CD conditions.

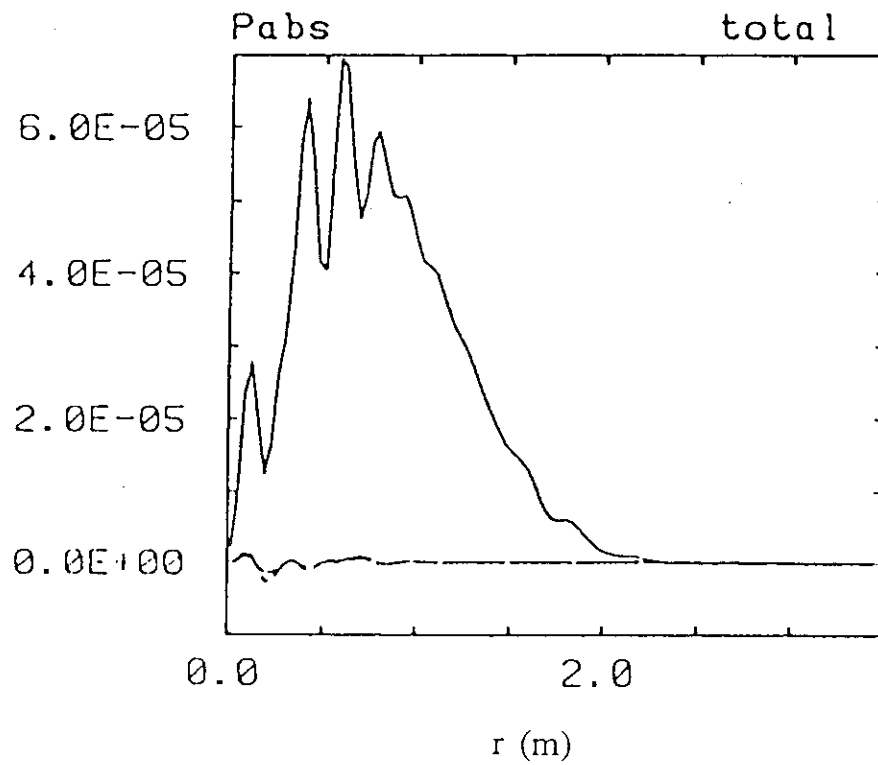


(b)



- 15 -

(a)



(b)

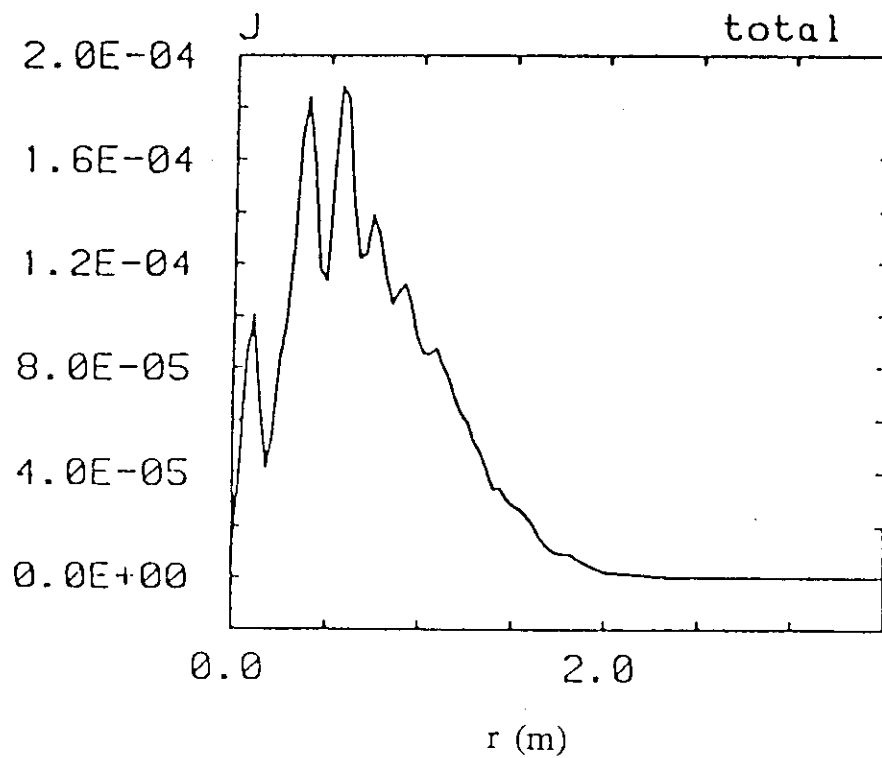


Fig. 2.4.1-3 Radial profiles of (a) the electron power absorption and (b) the driven current. 20MHz, $n=5$, $q_a=5$, $q_0=1$, $\alpha_N=2$, in-blanket antenna (off-midplane launching) and CD conditions.

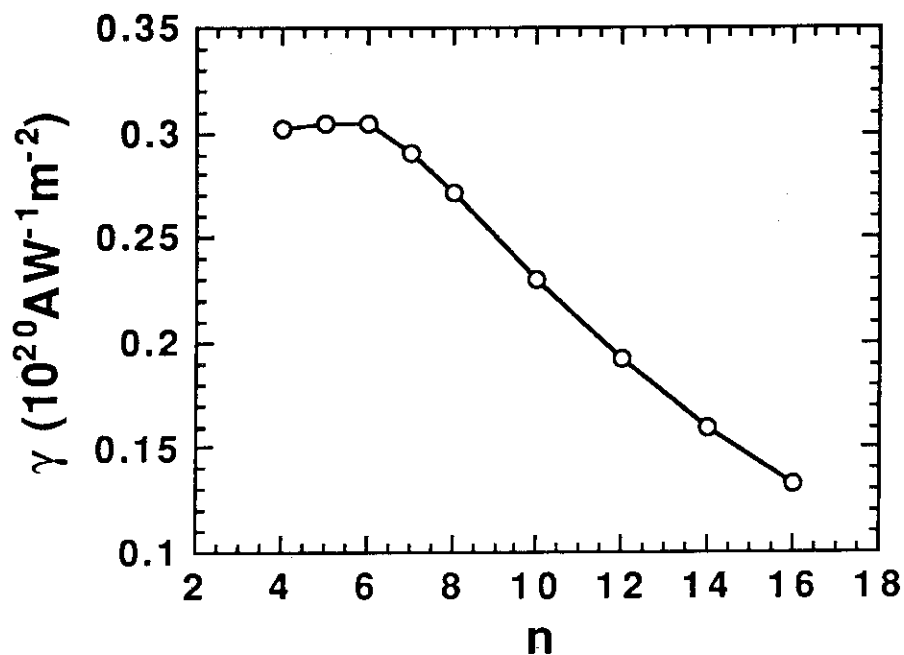


Fig. 2.4.1-4 The current drive figure of merit, γ , as a function of the toroidal mode number, n . 20MHz, $q_a=5$, $q_0=1$, $\alpha_N=2$, in-blanket antenna (off-midplane launching), CD conditions.

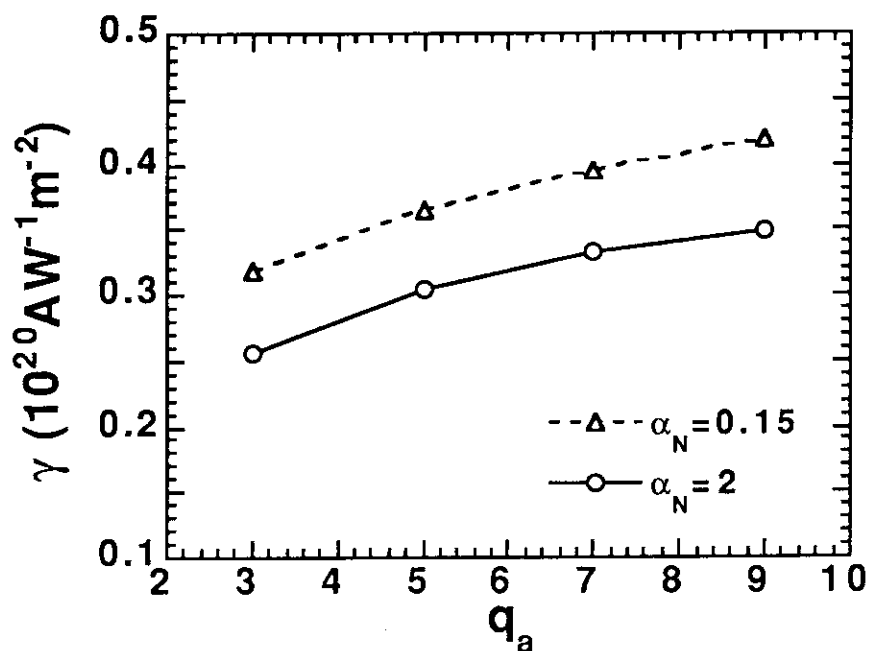


Fig. 2.4.1-5 The current drive figure of merit, γ , as a function of the edge safety factor, q_a . 20MHz, $n=5$, $q_0=1$, in-blanket antenna (off-midplane launching), CD conditions.

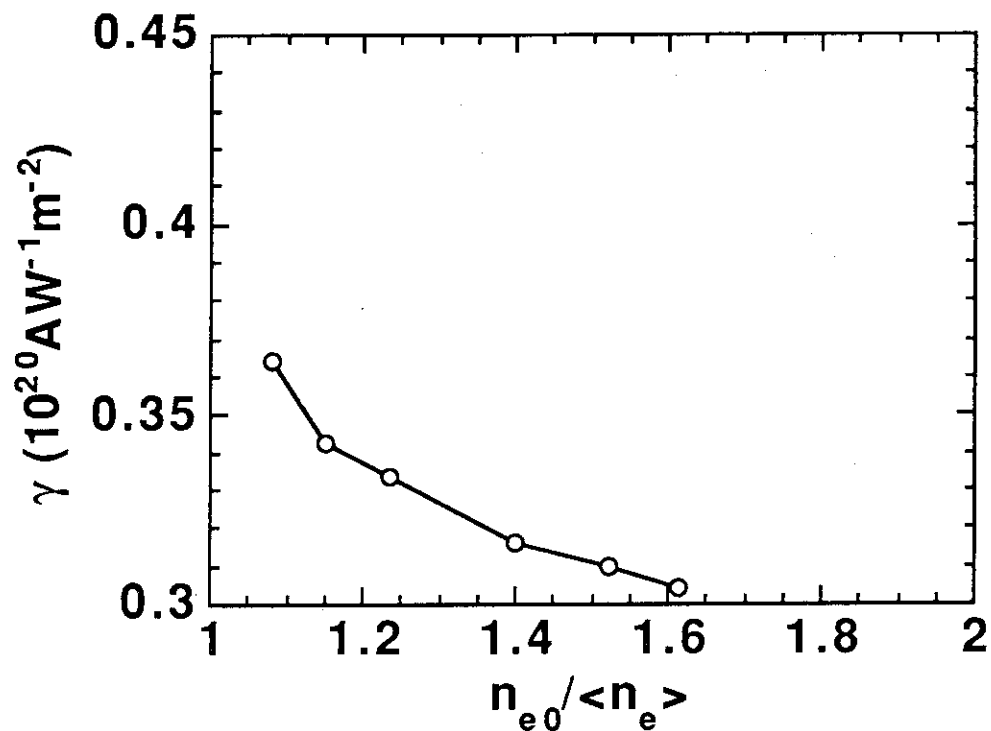


Fig. 2.4.1-6 The current drive figure of merit, γ , as a function of the electron density peaking factor, $n_{e0}/\langle n_e \rangle$. 20MHz, $n=5$, $q_a=5$, $q_0=1$, in-blanket antenna (off-midplane launching), CD conditions.

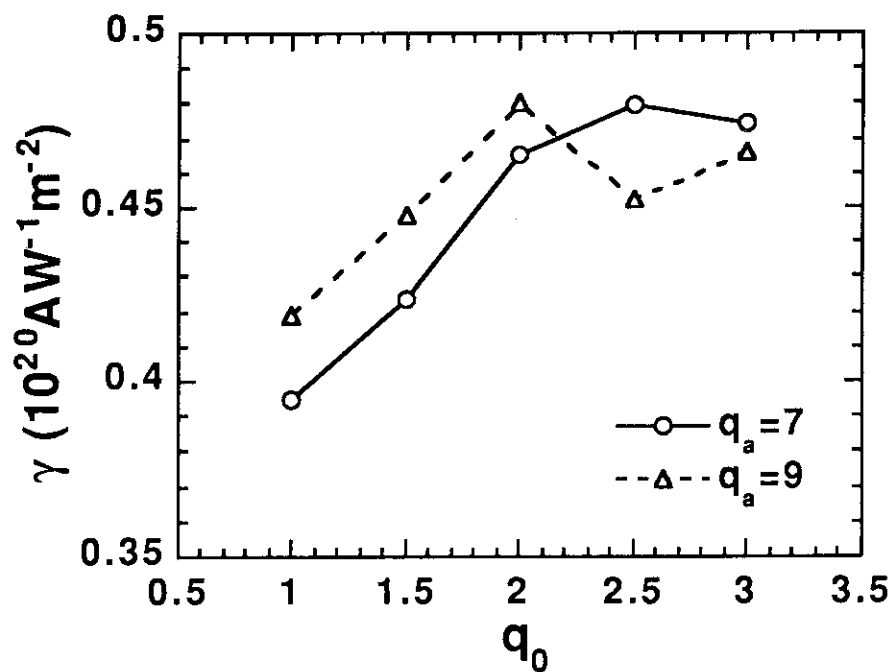


Fig. 2.4.1-7 The current drive figure of merit, γ , as a function of the central safety factor, q_0 . 20MHz, $n=5$, $\alpha_N=0.15$, in-blanket antenna (off-midplane launching), CD conditions.

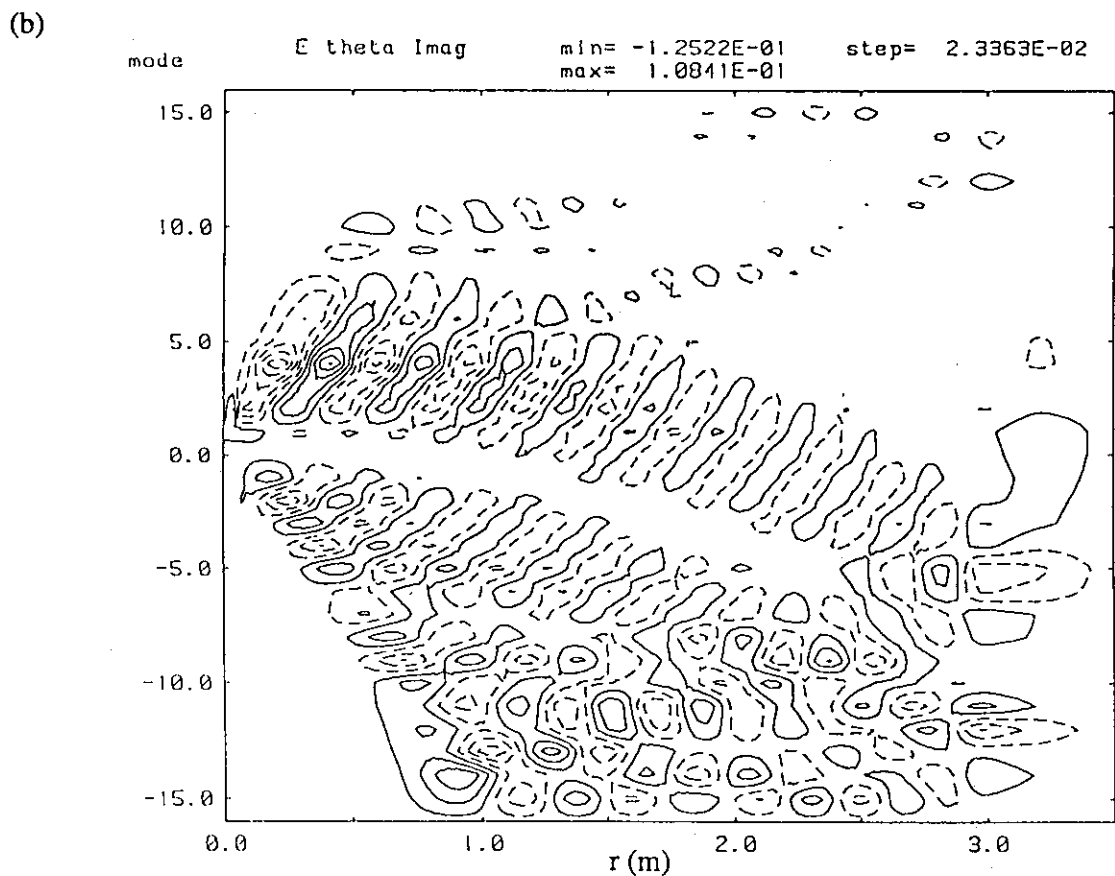
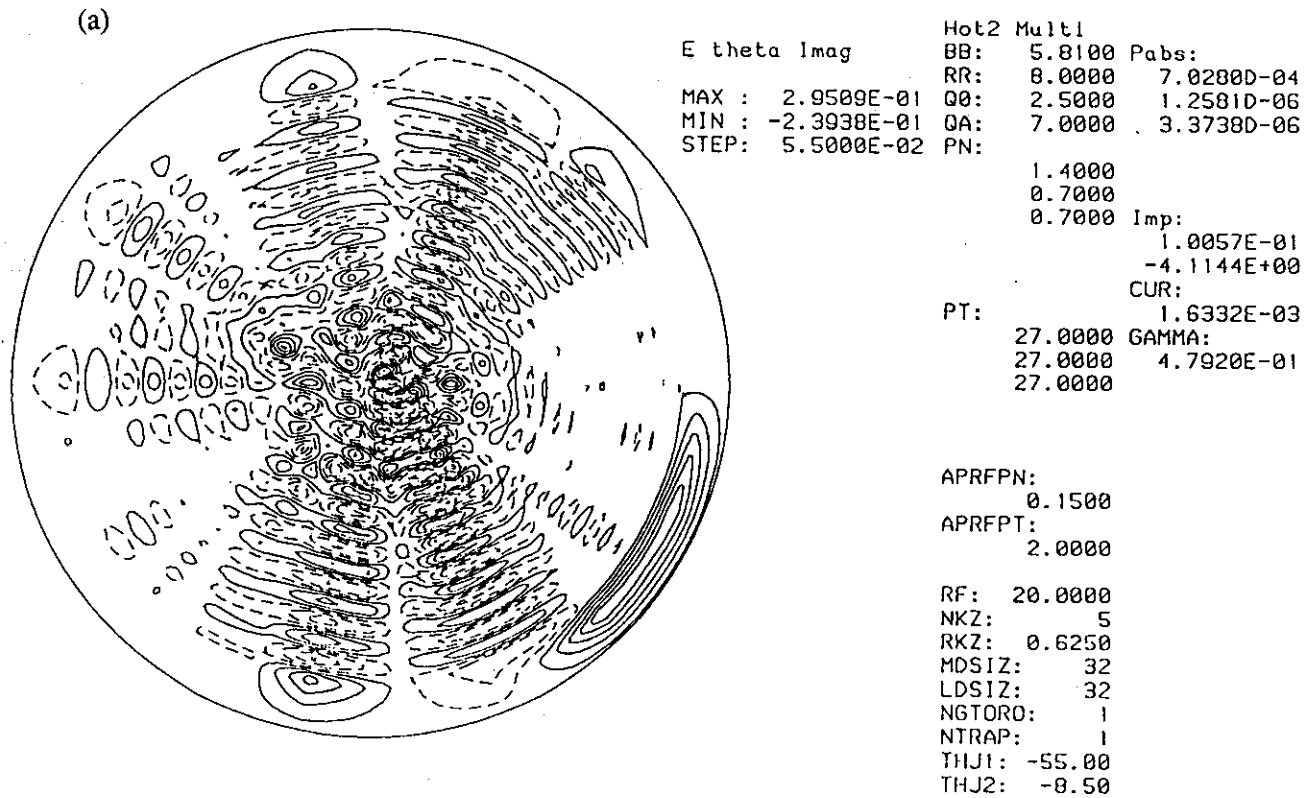


Fig. 2.4.1-8 Contour plots of the wave electric field (E_θ) (a) in the poloidal cross-section and (b) in a plane defined by the poloidal mode number and the minor radius. 20MHz, $n=5$, $q_a=7$, $q_0=2.5$, $\alpha_N=0.15$, in-blanket antenna (off-midplane launching) and CD conditions.

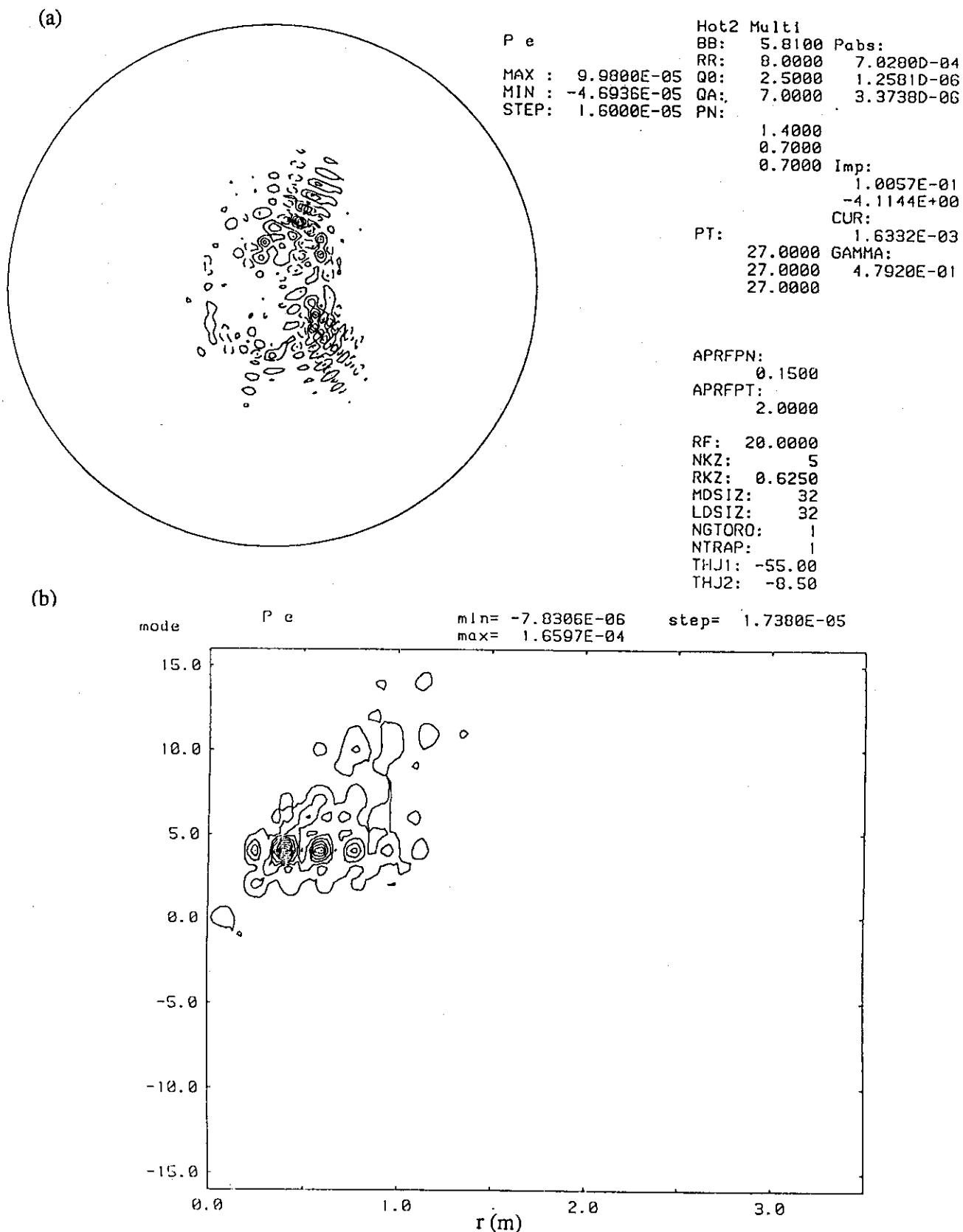
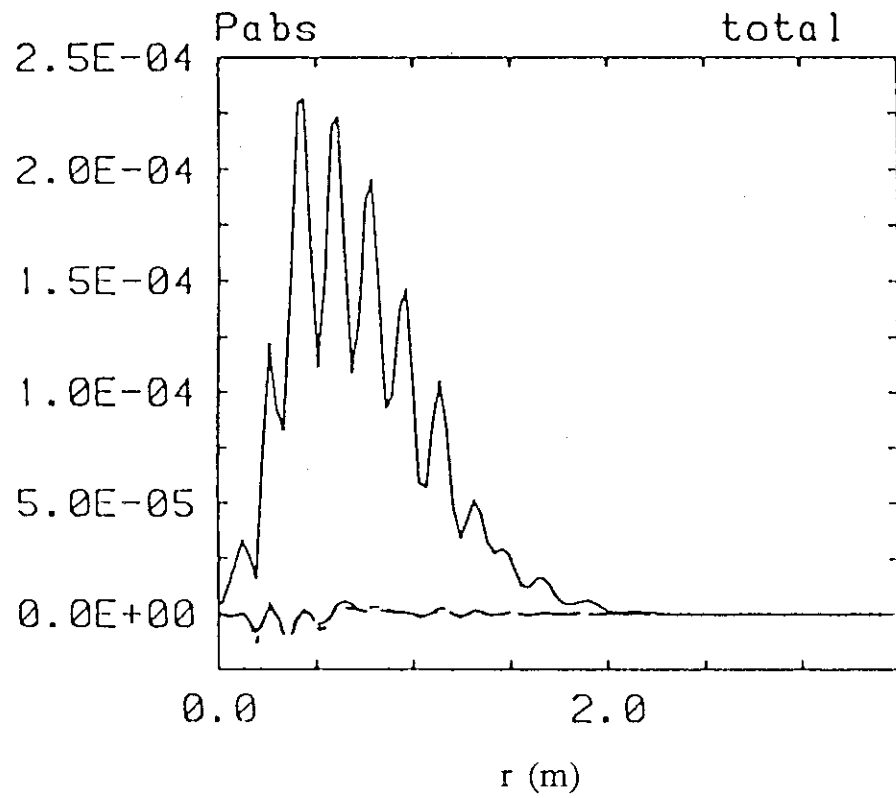


Fig. 2.4.1-9 Contour plots of the electron power absorption (P_e) (a) in the poloidal cross-section and (b) in a plane defined by the poloidal mode number and the minor radius. 20MHz, $n=5$, $q_a=7$, $q_0=2.5$, $\alpha_N=0.15$, in-blanket antenna (off-midplane launching) and CD conditions.

(a)



(b)

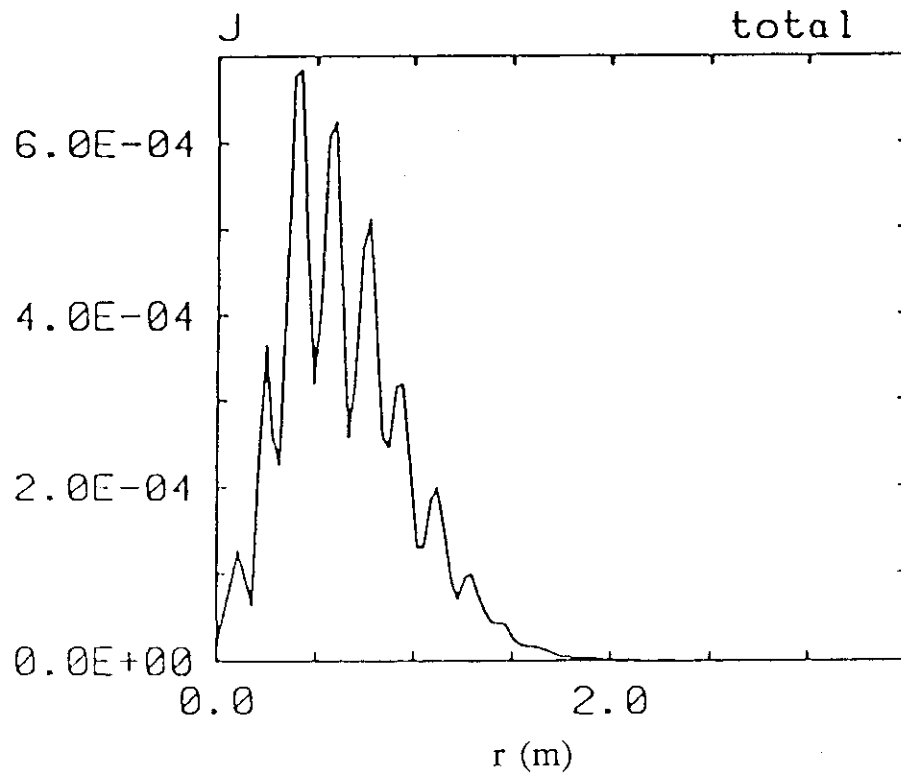


Fig. 2.4.1-10 Radial profiles of (a) the electron power absorption and (b) the driven current. 20MHz, $n=5$, $q_a=7$, $q_0=2.5$, $\alpha_N=0.15$, in-blanket antenna (off-midplane launching) and CD conditions.

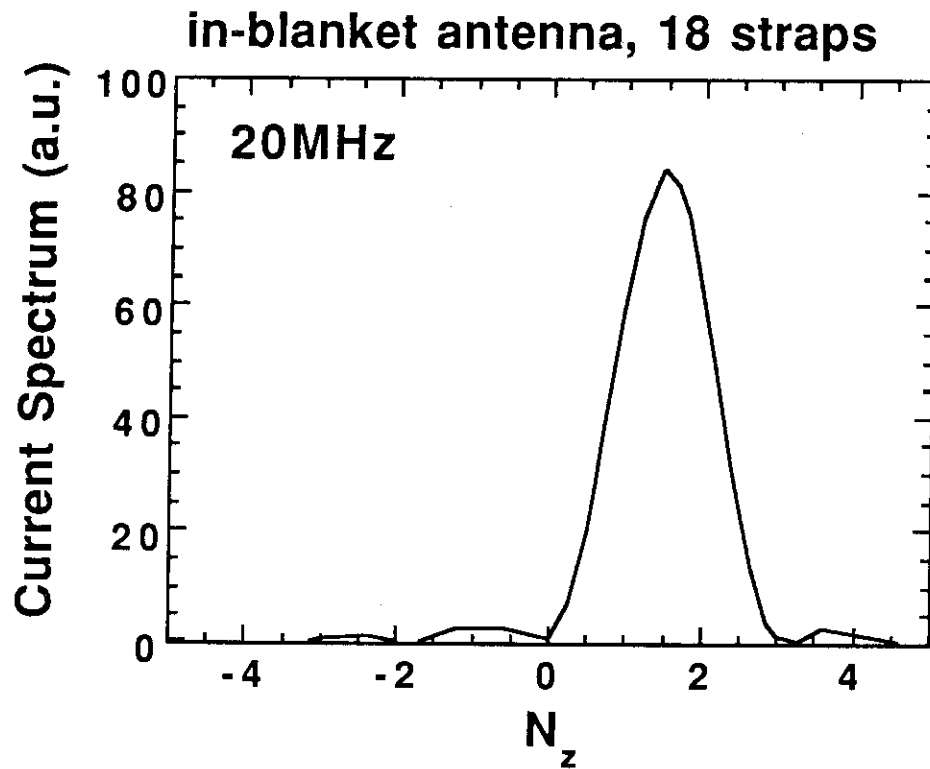


Fig. 2.4.1-11 Antenna current spectrum against the toroidal refractive index, N_z , for in-blanket antenna (18 straps) at 20MHz. Interval between adjacent straps=0.5m, width of current straps=0.26m, phase difference between adjacent straps=18°.

2.4.2 High frequency scenario

The high frequency scenario is such that the frequency is chosen to be slightly higher than the tritium second harmonic resonance frequency on axis and that fast waves launched unidirectionally are absorbed by electrons via TTMP/ELD as much as possible to drive a net current before they reach the tritium second harmonic resonance layer. Therefore, choice of the frequency and the toroidal refractive index is important to maximize the electron power absorption and the current drive efficiency. It is found that choice of the safety factor is not important for this scenario in contrast to the low frequency scenario.

Wave propagation and absorption

Analyses are done with the two-dimensional full wave code assuming a circular plasma cross-section similarly for the low frequency scenario but including fusion α particles, background ^4He and beryllium (6 species in total). For fusion α particles, we assume 1% density ratio to electrons and 2MeV central temperature with the same density and temperature profiles as those of other species. Figures 2.4.2-1~3 show the calculation results for 65MHz, $n=27$ (toroidal refractive index $N_z=2.5$), off-midplane launching and CD parameters (see Table 2.2-1). The standard values of the safety factor and the density profile index are taken to be $q_a=5$, $q_0=1$ and $\alpha_N=2$. Because of a strong damping, the wave fields are nicely converged near the center as indicated in Fig. 2.4.2-1 (a). Associated with this convergence, the poloidal mode number increases to a large number near the center as indicated in Fig. 2.4.2-1 (b). The parallel refractive index $N_{||}$ is then enhanced near the center and the electron power absorption and the current density profile are highly centrally peaked (Fig. 2.4.2-2, Fig. 2.4.2-3). Note that the power deposition and current density profiles are much more centrally peaked in this scenario than those in the low frequency scenario (see Fig. 2.4.1-3). This peaking effect is favourable for improving the current drive efficiency because of less trapped electrons near the center.

Dependence on the frequency

Dependence of the power partition and the current drive figure of merit on the frequency is shown in Fig. 2.4.2-4. The toroidal mode number is set to be 27. The optimum frequency

band for the current drive is found to be 62.5MHz - 65MHz. The triton absorption starts to increase with decreasing frequency below 62.5MHz, while deuteron/ α absorption increases rapidly with increasing frequency above 65MHz.

Dependence on the toroidal mode number

Figure 2.4.2-5 shows dependence on the toroidal mode number. The frequency is set to be 65MHz and other parameter are the same as in Fig. 2.4.2-4 but $\alpha_N=0.15$. The optimum toroidal mode number is found to be around 20~27. Namely, the optimum value of N_z is around 2~2.5. Below $n=20$ ($N_z=2$), the triton absorption quickly increases.

Dependence on the safety factor

Values of γ only slightly increase with increasing safety factor as indicated in Fig. 2.4.2-6 in contrast to the low frequency scenario. This can be explained with the strong focusing of the wave field near the center as mentioned above. The trapped particle effect is not important near the center. Hence, the current drive efficiency is not degraded even if the poloidal mode number increases rapidly near the center. Therefore, suppression of $N_{||}$ upshift via increase in the safety factor is not meaningful to improve the current drive efficiency in the high frequency scenario.

Dependence on the density profile

On the contrary, dependence on the density profile is rather stronger in the high frequency scenario than in the low frequency scenario. Figure 2.4.2-7 shows γ as a function of the density profile peaking factor, $n_{e0}/\langle n_e \rangle$. A value of γ increases by about 30% if α_N ($n_{e0}/\langle n_e \rangle$) is decreased from 2 (1.62) to 0.15 (1.08). The power deposition and the driven current profiles for $\alpha_N=0.15$ are shown in Fig. 2.4.2-8. One can see that these profiles almost coincide with those of the case of $\alpha_N=2$ (Fig. 2.4.2-3). On the other hand, some differences are found between them in the low frequency scenario as described in Sec. 2.4.1. That is the reason why γ is improved more largely for the high frequency scenario compared with the low frequency scenario.

Calculation for the high-q condition

Figures 2.4.2-9~11 show the calculation results for the high-q conditions ($q_a=7$, $q_0=2.5$ and $\alpha_N=0.15$) with 65MHz, $n=27$ (toroidal refractive index $N_z=2.5$) and off-midplane launching. Although the safety factor and the density profile index are very different from the standard conditions (Fig. 2.4.2-1~3), the wave propagation and the power absorption are quite similar. Very peaked current density profile can be predicted. The γ value is $0.44 \times 10^{20} \text{AW}^{-1} \text{m}^{-2}$, while it is $0.32 \times 10^{20} \text{AW}^{-1} \text{m}^{-2}$ for the standard case. The difference is mainly due to the density profile.

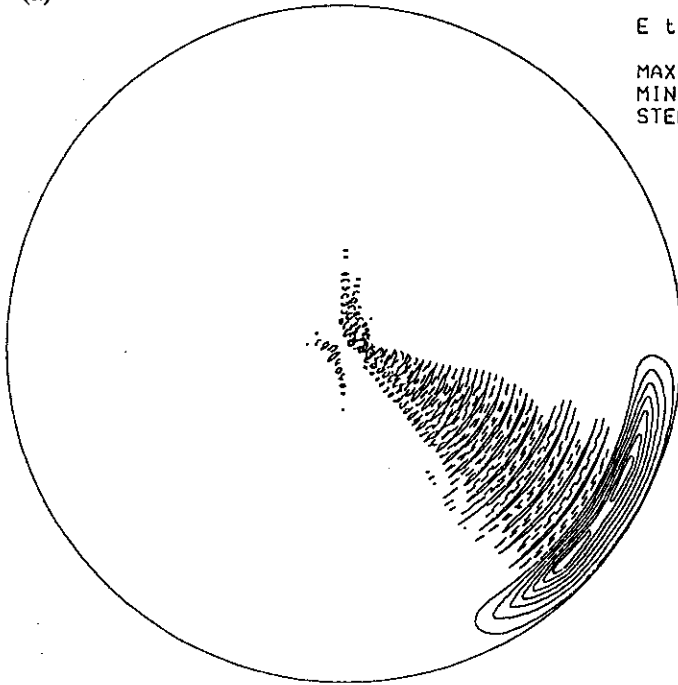
Antenna current spectrum

In these analyses, the current drive efficiency is evaluated with a single toroidal mode number. The antenna current spectrum for the 18 strap array of the in-blanket antenna is sufficiently sharp for the current drive operation at around 65MHz as shown in Fig. 2.4.2-12. Even if the antenna spectrum were taken into account, reduction of γ would be about 7%.

Comparison with the low frequency scenario

Including the antenna spectrum, the high frequency scenario is rather superior to the low frequency scenario in view of the current drive efficiency. Some other additional merits on the current drive are (1) weak dependence on the safety factor (in other words, the current drive efficiency is high even for low-q discharges), and (2) stable antenna loading because of the strong damping per pass. It is also favourable for quick switching from or to the central ion heating via triton second harmonic resonance, of which optimum conditions would be $N_z \approx 1$ and the frequency $\approx 60\text{MHz}$. In this condition, 75% of the total power is absorbed by tritons near the center.

(a)



E theta Imag

MAX : 8.7682E-01
 MIN : -2.8743E-01
 STEP: 1.2000E-01

Hot2 Multi

BB: 5.8100 Pabs:
 RR: 8.0000 1.6981D-03
 Q0: 1.0000 7.1655D-06
 QA: 5.0000 5.9741D-05
 PN: 3.1395D-06
 1.4000 1.9879D-05
 0.5180 6.1460D-05
 0.5180 Imp:
 0.1400 2.6555E-01
 0.0140 -6.9640E+00
 0.0140 CUR:

PT: 4.3265E-03
 27.0000 GAMMA:
 27.0000 3.2267E-01
 27.0000
 27.0000
 2000.0000
 27.0000

APRFPN:

2.0000

APRFPT:

2.0000

RF: 65.0000

NKZ: 27

RKZ: 3.3750

MDSIZ: 32

LDSIZ: 32

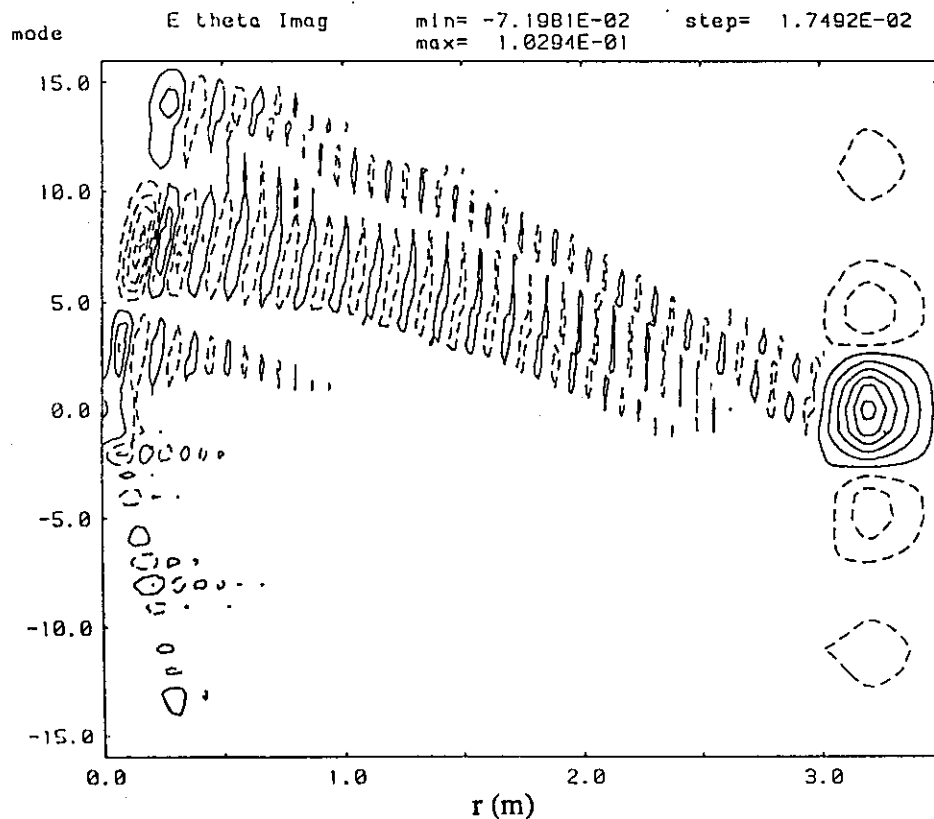
NGTORO: 1

NTRAP: 1

THJ1: -55.00

THJ2: -0.50

(b)



E theta Imag

min= -7.1981E-02
 max= 1.0294E-01

step= 1.7492E-02

Fig. 2.4.2-1 Contour plots of the wave electric field (E_θ) (a) in the poloidal cross-section and (b) in a plane defined by the poloidal mode number and the minor radius. 65MHz, $n=27$, $q_a=5$, $q_0=1$, $\alpha_N=2$, in-blanket antenna (off-midplane launching) and CD conditions.

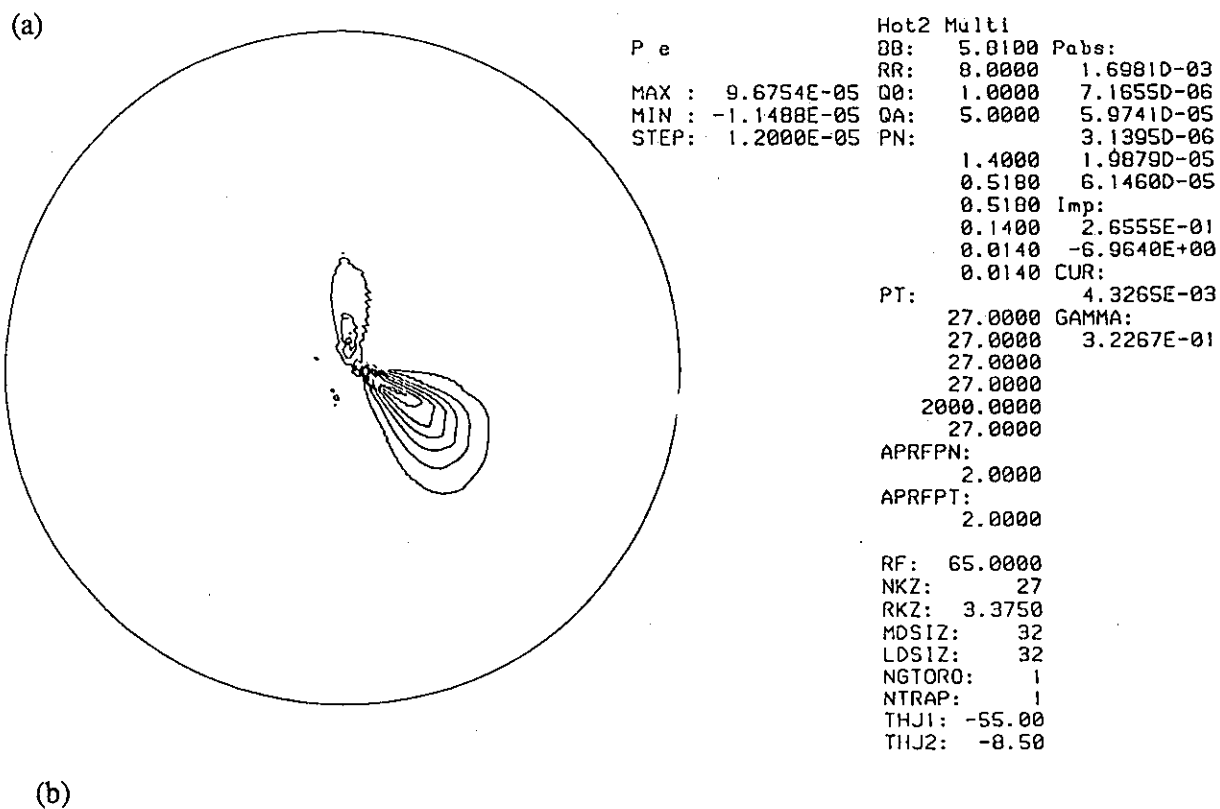
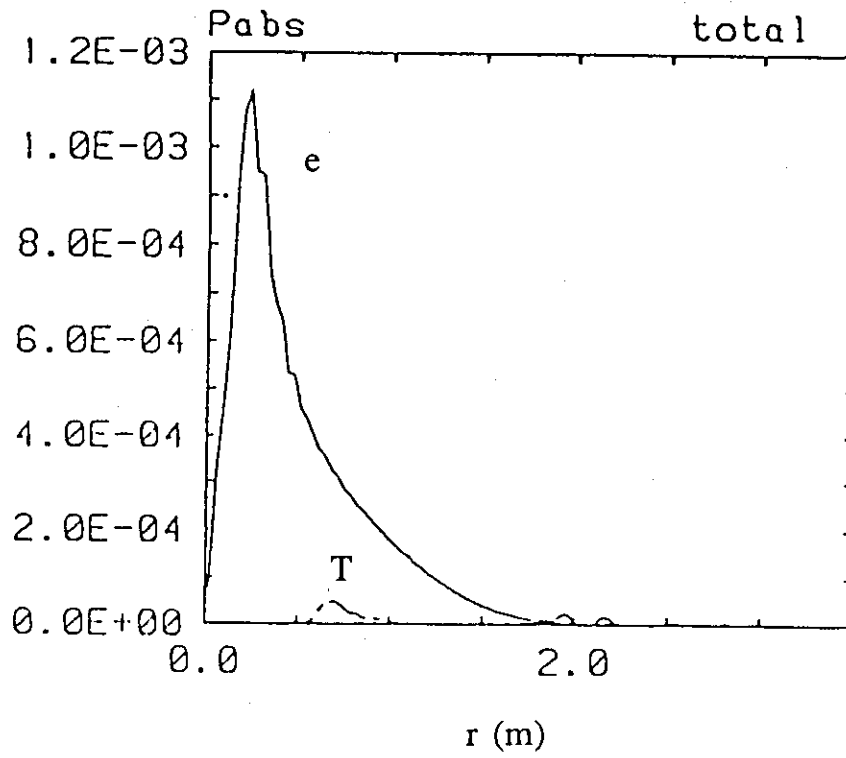


Fig. 2.4.2-2 Contour plots of the electron power absorption (P_e) (a) in the poloidal cross-section and (b) in a plane defined by the poloidal mode number and the minor radius. 65MHz, $n=27$, $q_a=5$, $q_0=1$, $\alpha_N=2$, in-blanket antenna (off-midplane launching) and CD conditions.

(a)



(b)

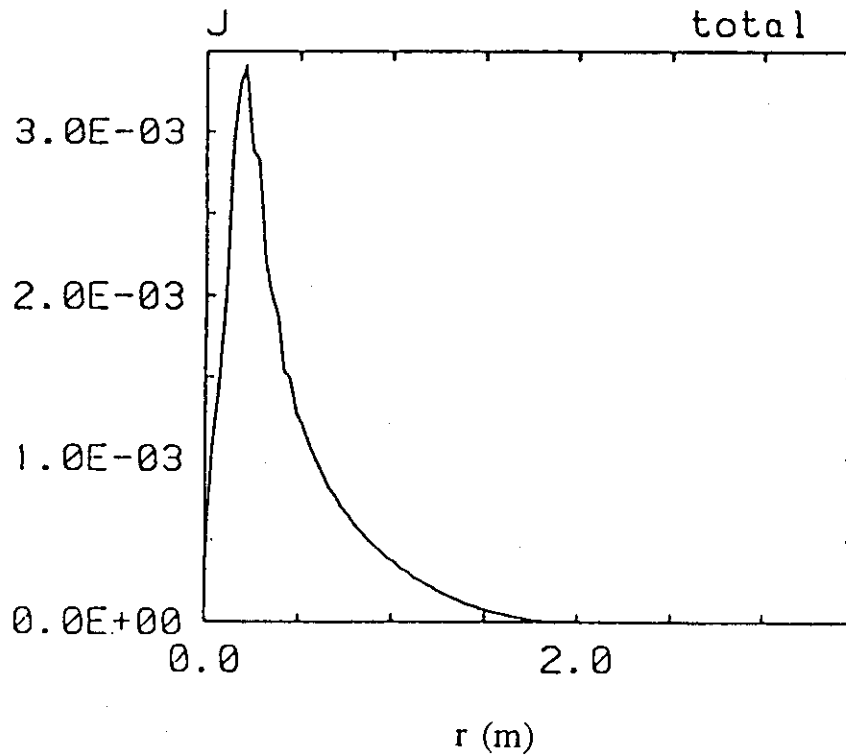


Fig. 2.4.2-3 Radial profiles of (a) the electron and ion power absorption and (b) the driven current. 65MHz, $n=27$, $q_a=5$, $q_0=1$, $\alpha_N=2$, in-blanket antenna (off-midplane launching) and CD conditions.

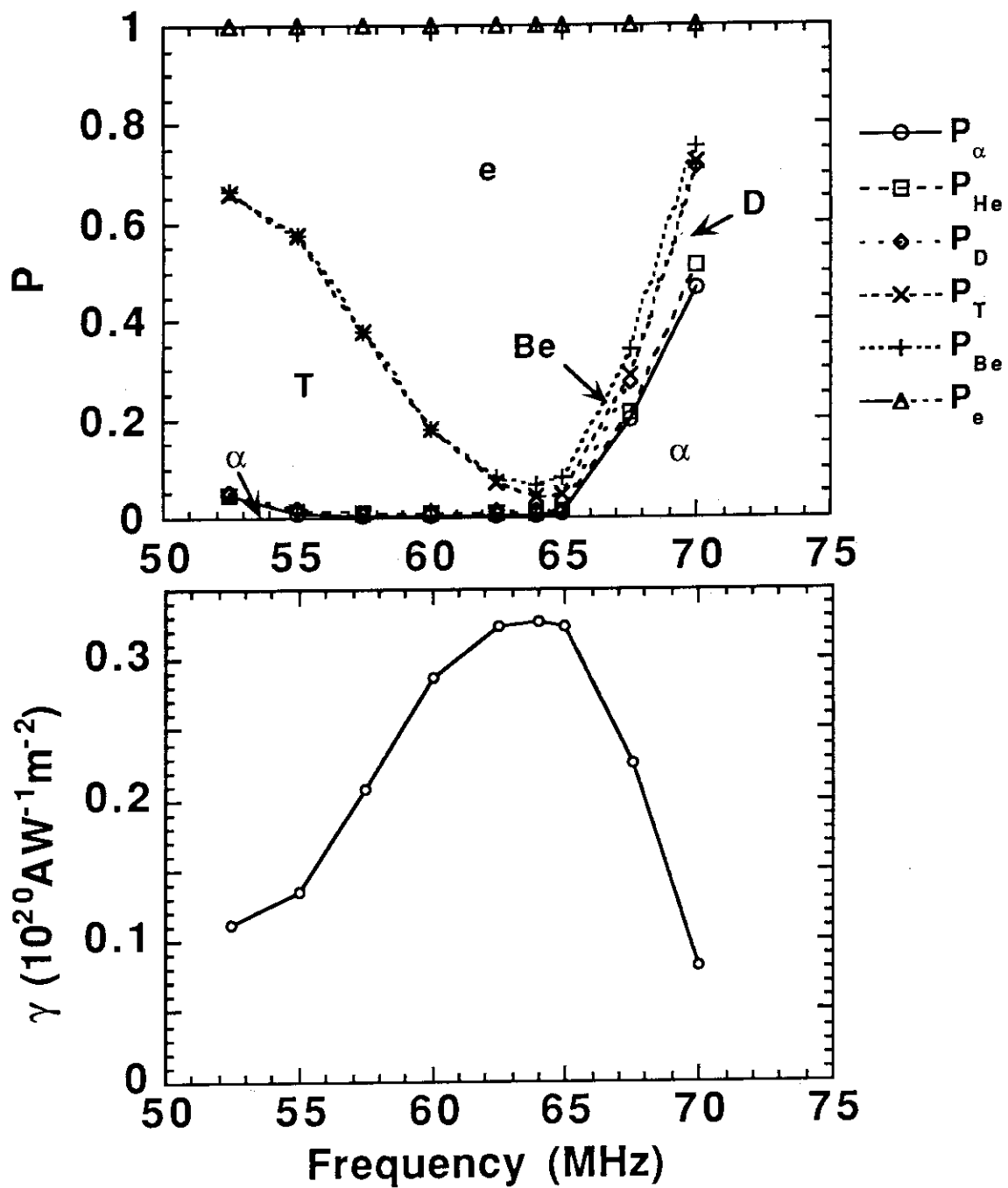


Fig. 2.4.2-4 Power partition and current drive figure of merit as a function of frequency. $n=27$, $q_a=5$, $q_0=1$, $\alpha_N=2$, in-blanket antenna (off-midplane launching) and CD conditions.

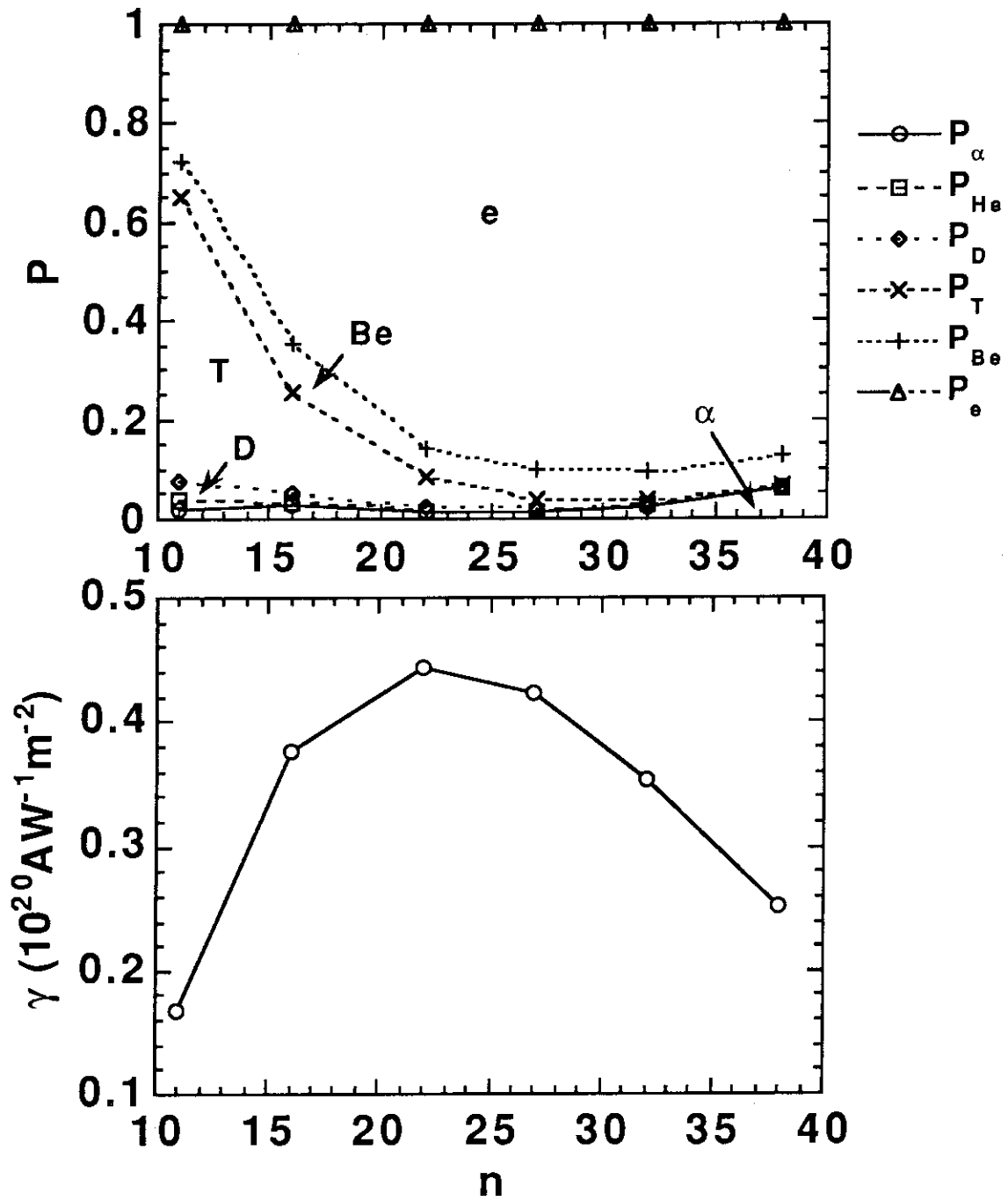


Fig. 2.4.2-5 Power partition and current drive figure of merit as a function of the toroidal mode number, n . 65MHz, $q_a=5$, $q_0=1$, $\alpha_N=0.15$, in-blanket antenna (off-midplane launching) and CD conditions.

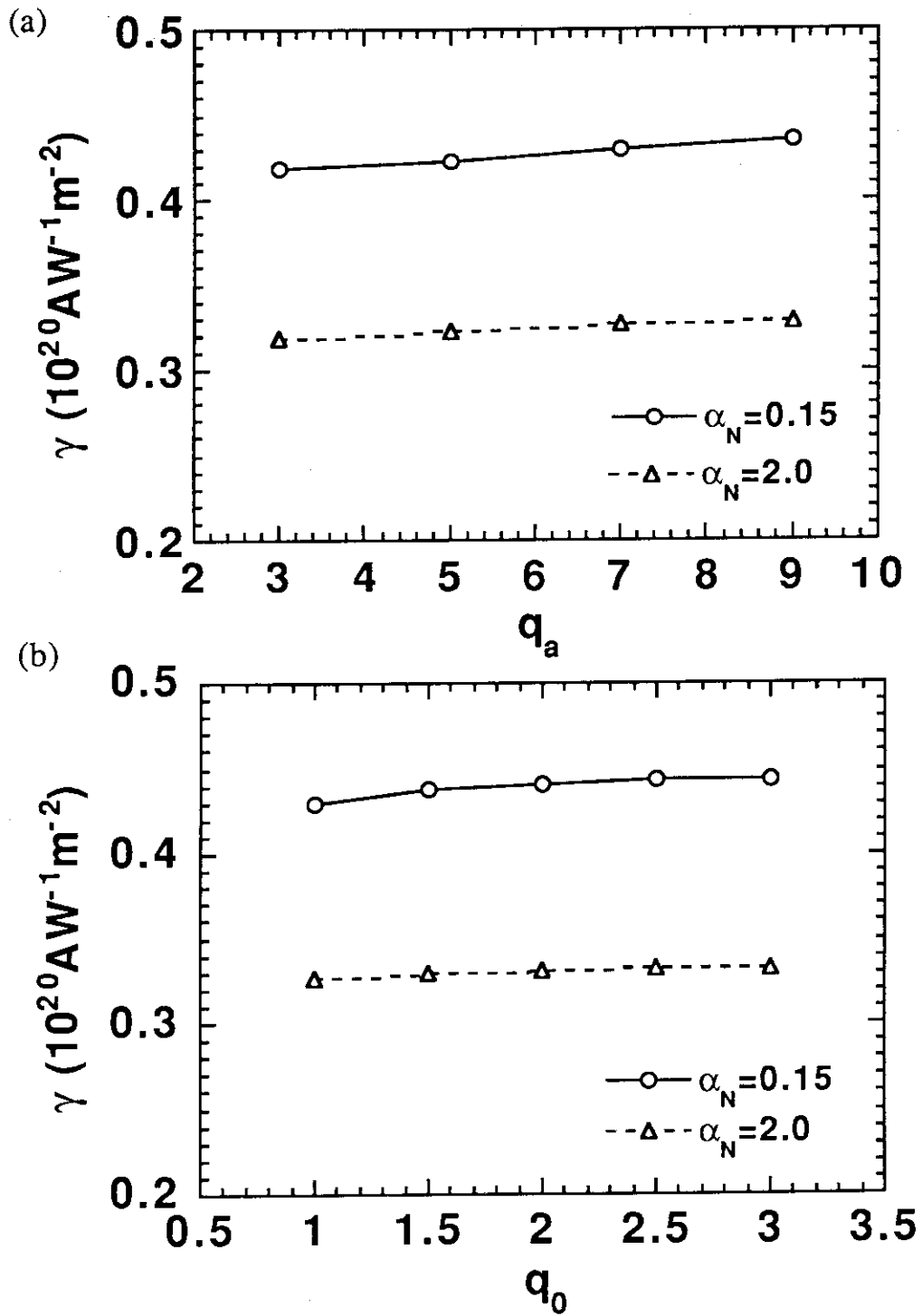


Fig. 2.4.2-6 Current drive figure of merit as a function of (a) the edge safety factor, q_a , and (b) the central safety factor, q_0 . In (a), q_0 is fixed at 1, and in (b), q_a is fixed at 7. 65MHz, $n=27$, in-blanket antenna (off-midplane launching) and CD conditions.

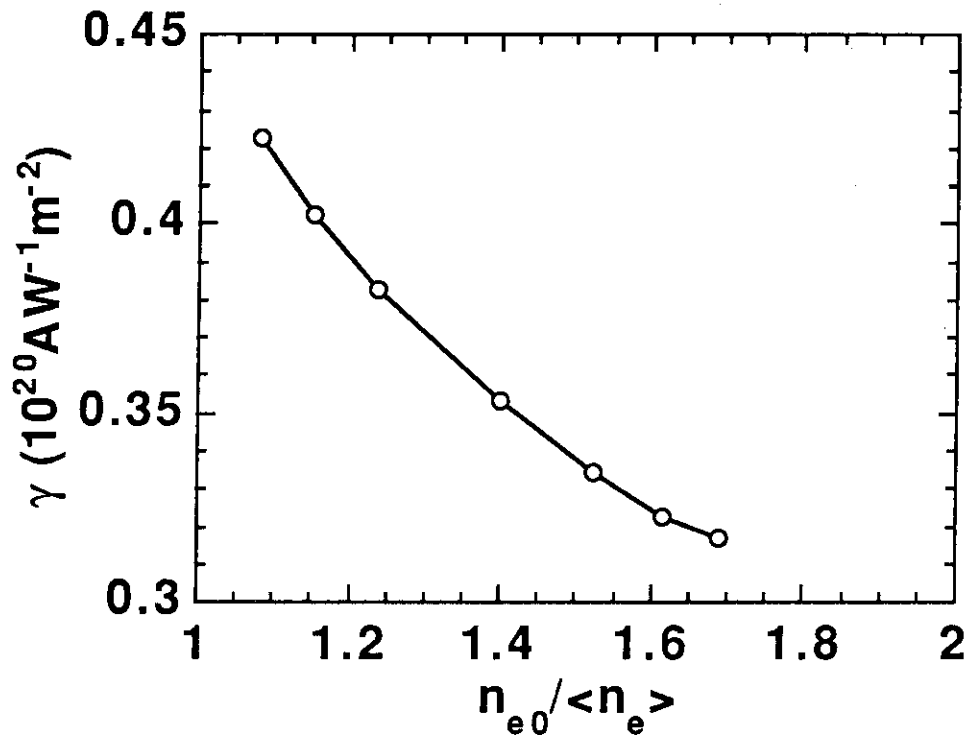
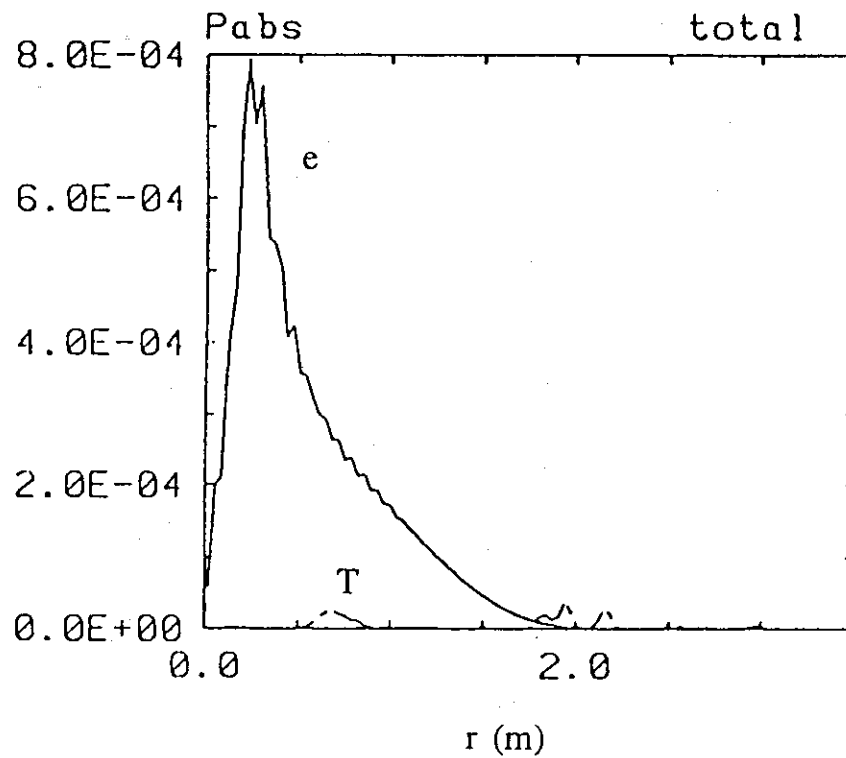


Fig. 2.4.2-7 Current drive figure of merit as a function of the electron density profile peaking factor, $n_{e0}/\langle n_e \rangle$. 65MHz, $n=27$, $q_a=5$, $q_0=1$, in-blanket antenna (off-midplane launching) and CD conditions.

(a)



(b)

(b)

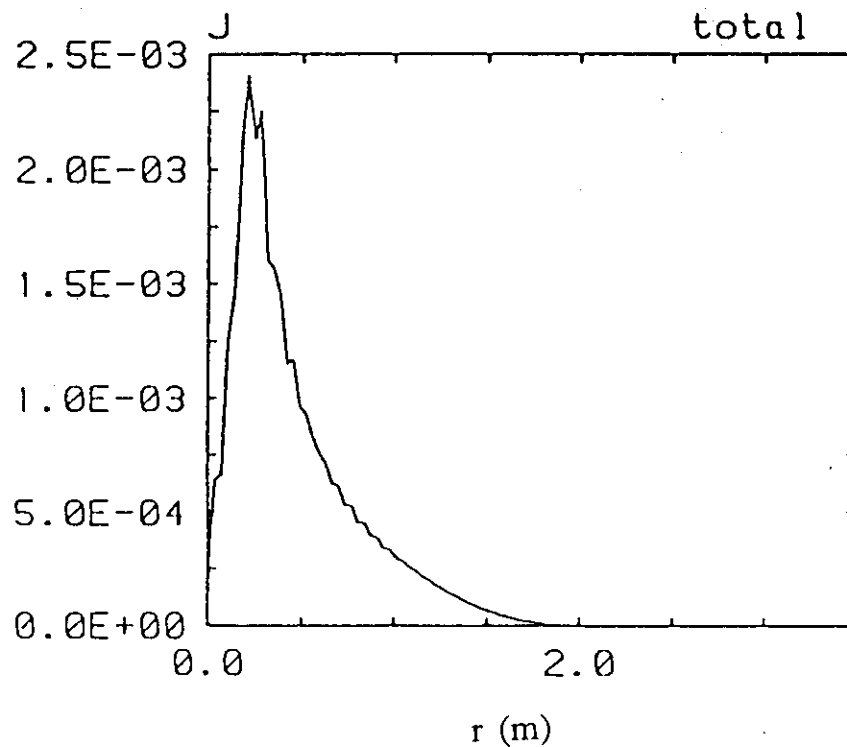
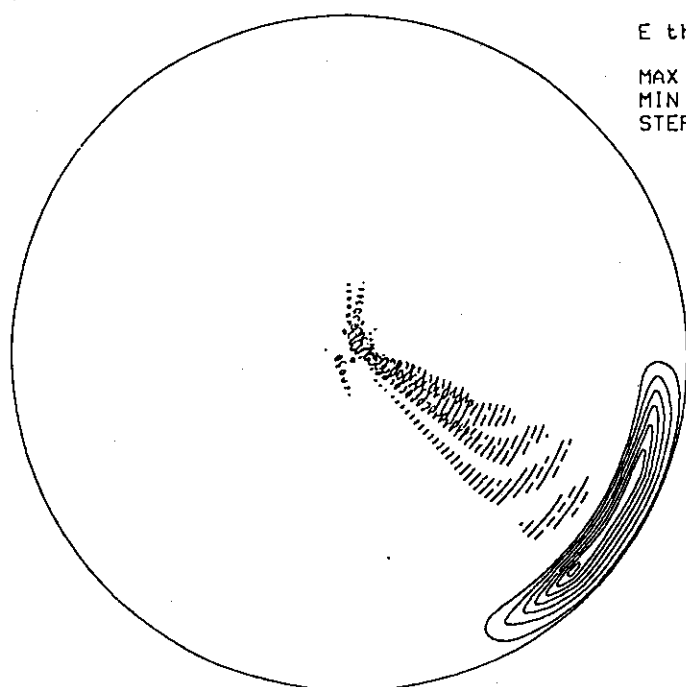


Fig. 2.4.2-8 Radial profiles of (a) the electron and ion power absorption and (b) the driven current. 65MHz, $n=27$, $q_a=5$, $q_0=1$, $\alpha_N=0.15$, in-blanket antenna (off-midplane launching) and CD conditions.

(a)



Hot2 Multi
 BB: 5.0100 Pabs:
 RR: 8.0000 1.4563D-03
 Q0: 2.5000 4.2402D-06
 QA: 7.0000 4.3862D-05
 PN: 1.5600D-06
 1.4000 2.7178D-05
 0.5180 1.0352D-04
 0.5180 Imp:
 0.1400 2.3511E-01
 0.0140 -6.9583E+00
 0.0140 CUR:
 PT: 3.5187E-03
 27.0000 GAMMA:
 27.0000 4.4334E-01
 27.0000
 27.0000
 2000.0000
 27.0000
 APRFPN:
 0.1500
 APRFPT:
 2.0000
 RF: 65.0000
 NKZ: 27
 RKZ: 3.3750
 MDSIZ: 32
 LDSIZ: 32
 NGTORD: 1
 NTRAP: 1
 THJ1: -55.00
 THJ2: -8.50

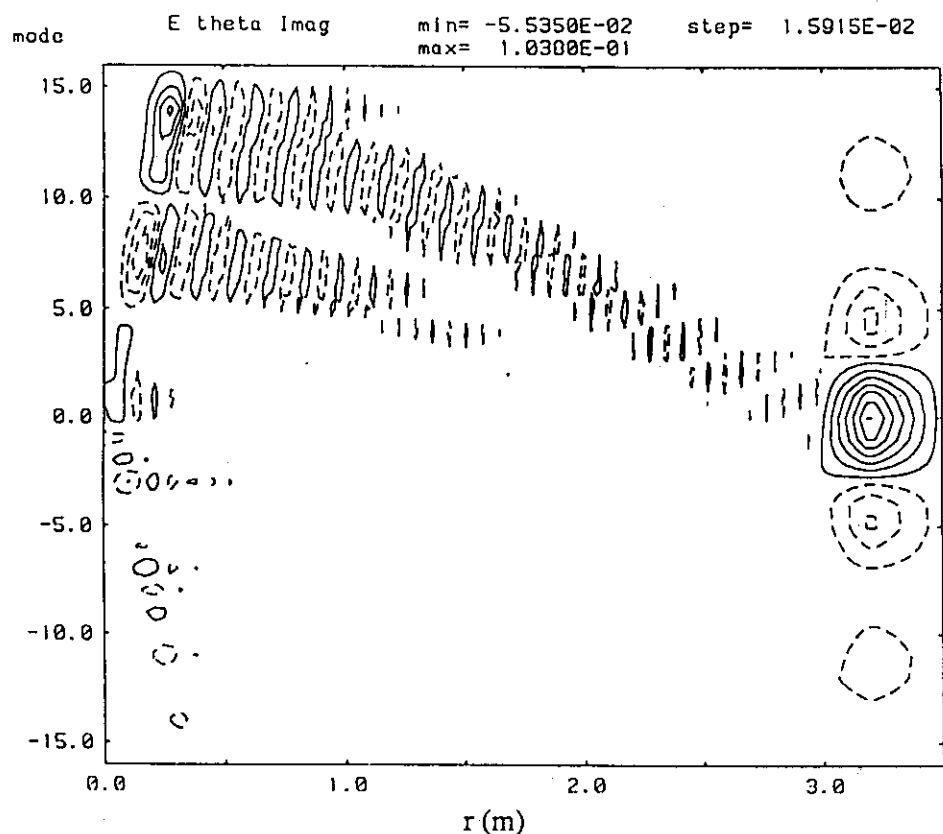
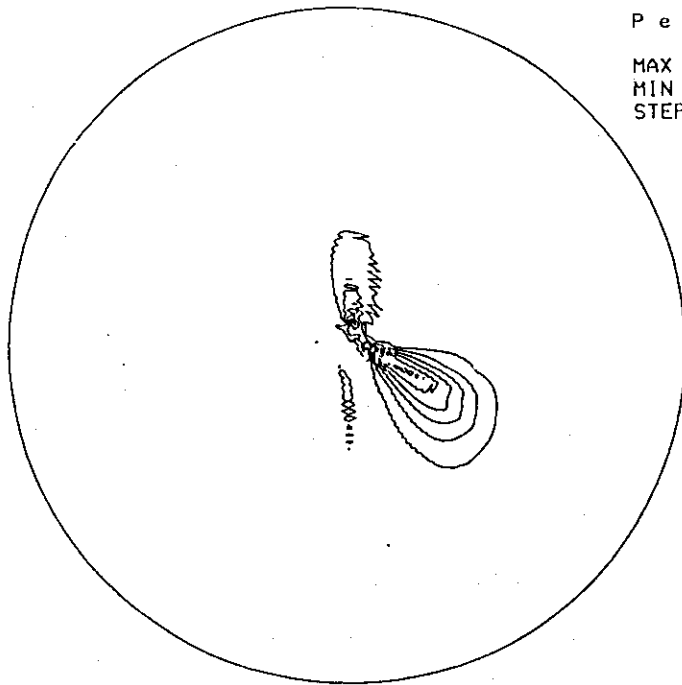


Fig. 2.4.2-9 Contour plots of the wave electric field (E_θ) (a) in the poloidal cross-section and (b) in a plane defined by the poloidal mode number and the minor radius. 65MHz, $n=27$, $q_a=7$, $q_0=2.5$, $\alpha_N=0.15$, in-blanket antenna (off-midplane launching) and CD conditions.

(a)



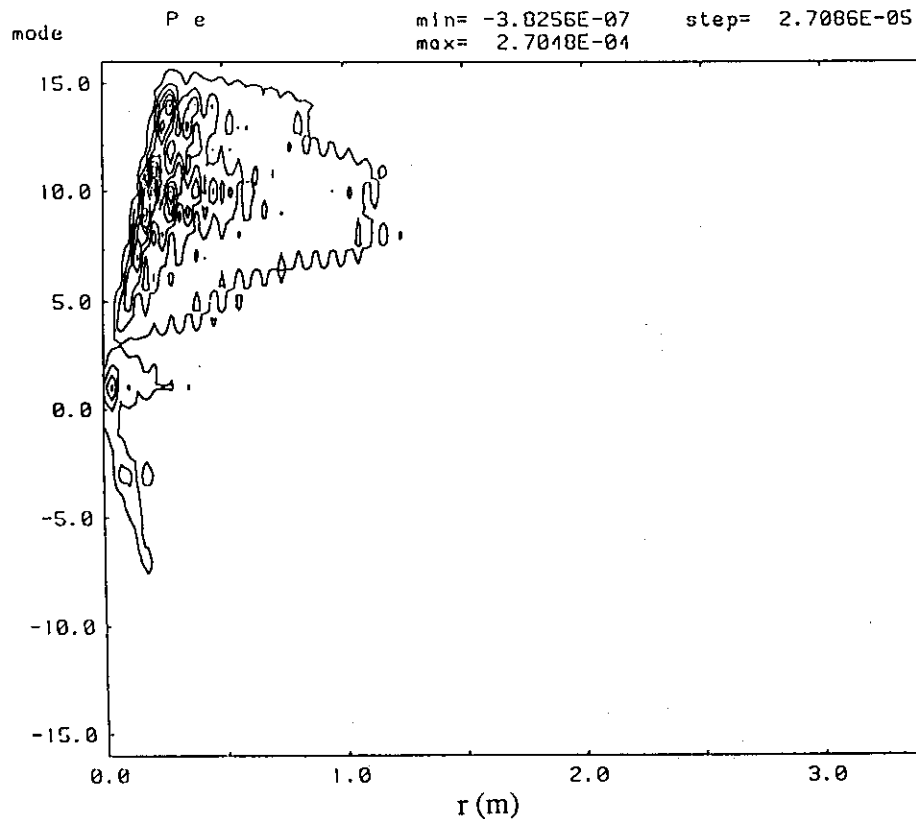
P e

 MAX : 7.0005E-05
 MIN : -1.0096E-05
 STEP: 1.0000E-05

Hot2 Multi

 BB: 5.8100 Pabs:
 RR: 8.0000 1.4563D-03
 Q0: 2.5000 4.2402D-06
 QA: 7.0000 4.3062D-05
 PN: 1.5600D-06
 1.4000 2.7178D-05
 0.5180 1.0352D-04
 0.5180 Imp:
 0.1400 2.3511E-01
 0.0140 -6.9503E+00
 0.0140 CUR:
 PT: 3.5187E-03
 27.0000 GAMMA:
 27.0000 4.4334E-01
 27.0000
 27.0000
 2000.0000
 27.0000
 APRFPN:
 0.1500
 APRFPT:
 2.0000
 RF: 65.0000
 NKZ: 27
 RKZ: 3.3750
 MDSIZ: 32
 LDSIZ: 32
 NGTORO: 1
 NTRAP: 1
 THJ1: -55.00
 THJ2: -8.50

(b)



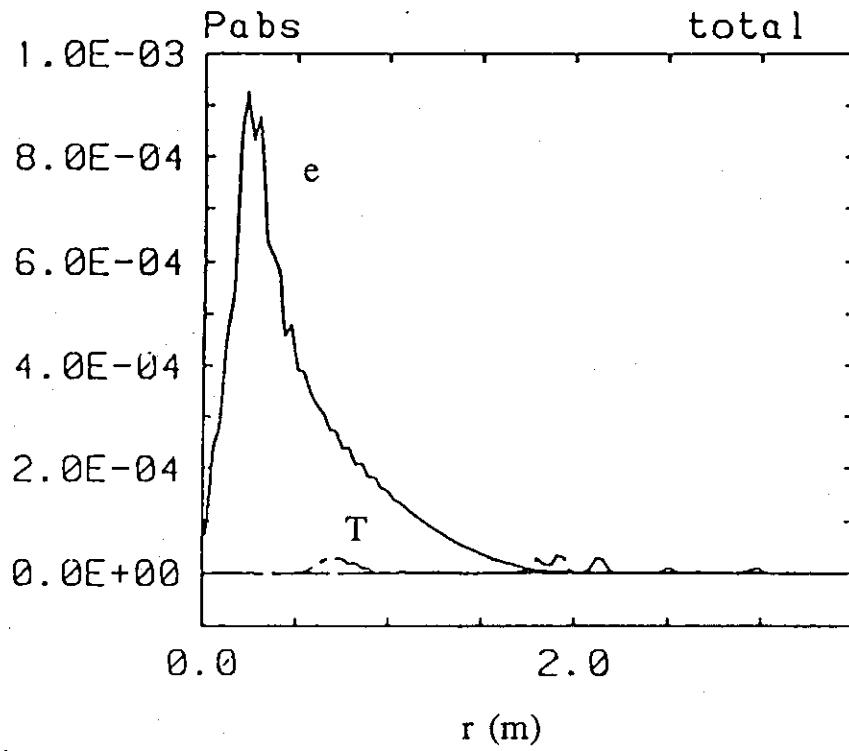
P e

 min= -3.0256E-07
 max= 2.7048E-04

step= 2.7086E-05

Fig. 2.4.2-10 Contour plots of the electron power absorption (P_e) (a) in the poloidal cross-section and (b) in a plane defined by the poloidal mode number and the minor radius. 65MHz, $n=27$, $q_a=7$, $q_0=2.5$, $\alpha_N=0.15$, in-blanket antenna (off-midplane launching) and CD conditions.

(a)



(b)

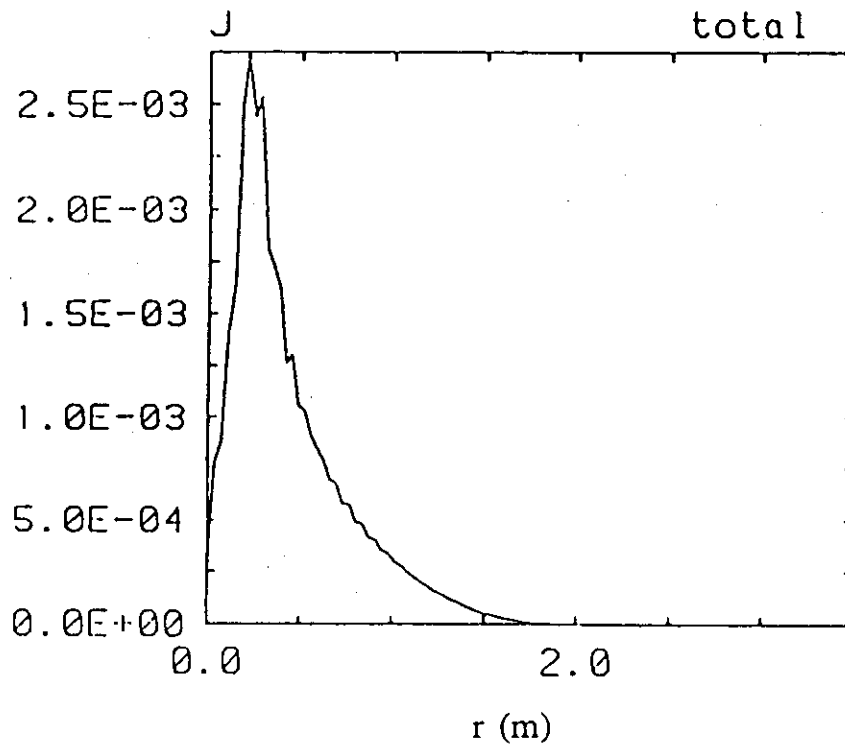


Fig. 2.4.2-11 Radial profiles of (a) the electron and ion power absorption and (b) the driven current. 65MHz, $n=27$, $q_a=7$, $q_0=2.5$, $\alpha_N=0.15$, in-blanket antenna (off-midplane launching) and CD conditions.

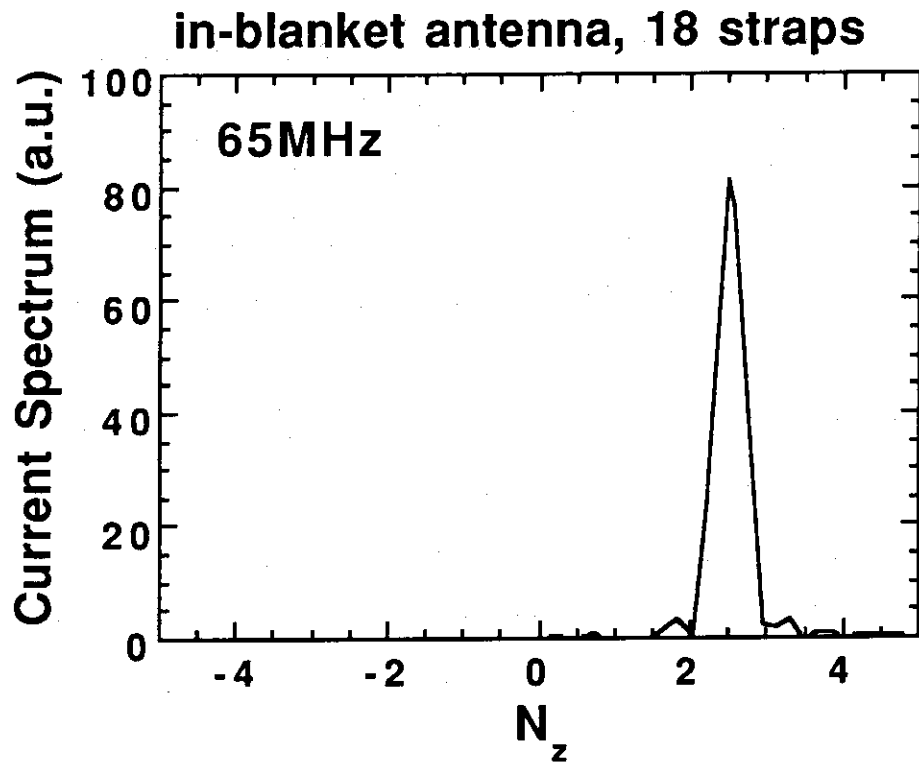


Fig. 2.4.2-12 Antenna current spectrum against the toroidal refractive index, N_z , for in-blanket antenna (18 straps) at 65MHz. Interval between adjacent straps=0.5m, width of current straps=0.26m, phase difference between adjacent straps=97.5°.

2.4.3 Summary

- (1) For the low frequency scenario (20MHz , $f < f_{cT}$), the current drive figure of merit (γ) is significantly improved with higher safety factor and with broader density profile. The highest value of γ , $0.48 \times 10^{20} \text{AW}^{-1} \text{m}^{-2}$ is obtained for $q_a=7$, $q_0=2.5$ and $\alpha_N=0.15$ with circular plasma cross-section, while γ is $0.3 \times 10^{20} \text{AW}^{-1} \text{m}^{-2}$ for $q_a=5$, $q_0=1$ and $\alpha_N=2$. However, the antenna current spectrum with 18 strap array is not sufficiently sharp at 20MHz . γ would decrease by 25% if the antenna spectrum were taken into account.
- (2) For the high frequency scenario ($\sim 65\text{MHz}$, $f \geq 2f_{cT}$), values of γ comparable with the low frequency scenario are obtained with a proper choice of the frequency and the toroidal refractive index. The optimum frequency and toroidal refractive index are $62.5\text{MHz} \sim 65\text{MHz}$ and $2 \sim 2.5$, respectively. The driven current profile is more centrally peaked than that for the low frequency scenario. The dependence on the safety factor is much weaker but that on the density profile is rather stronger than those of the low frequency scenario, because of less trapped particle effects due to better single pass absorption. The highest value of γ , $0.44 \times 10^{20} \text{AW}^{-1} \text{m}^{-2}$ is obtained for $q_a=7$, $q_0=2.5$ and $\alpha_N=0.15$ with circular plasma cross-section, while γ is $0.32 \times 10^{20} \text{AW}^{-1} \text{m}^{-2}$ for $q_a=5$, $q_0=1$ and $\alpha_N=2$. The antenna current spectrum with the 18 strap array is sufficiently sharp at 65MHz . γ would be decreased only about 7% if the antenna spectrum were taken into account.
- (3) The high frequency scenario has better current drive performance with the 18 strap array in view of the current drive efficiency and the weak dependence on the safety factor (almost equal efficiency from low- q to high- q (high β_p scenario) as well as the stable antenna loading. It is also favourable for quick switching between the current drive mode and the central ion heating mode.

2.5 In-port Antennas

2.5.1 Optimum frequency for FWCD

The high frequency scenario is considered to be a main current drive scheme for the in-port antenna, since the antenna length is too short for the low frequency scenario. In addition, the directivity is too bad for 20MHz operation with the in-port antenna, of which toroidal width is much more narrow than that of the in-blanket antenna. As discussed in Sec. 2.3, the optimum frequency for the current drive with the high frequency scenario is around 60MHz, where $2\omega_{cT}$ resonance is near on axis. Above 65MHz, the current drive efficiency would be degraded significantly because of increase in power absorption by deuterium and helium 4 at low field side edge. One should note that the antenna current spectrum of the in-port antenna is much broader than that of the in-blanket antenna and that the in-port antenna is assumed to be a midplane launching, while the in-blanket antenna is assumed to be an off-midplane launching. Then the antenna spectrum should be taken into account for evaluation of the current drive performance, and the ion edge resonance becomes important from somewhat lower frequency.

The power partition among species and the current drive figure of merit are calculated by the 1-D full wave code with full antenna spectrum for the CD conditions (see Table 2.2-1) over a frequency range of 55-70MHz. The results are shown in Fig. 2.5.1-1 and Fig. 2.5.1-2. The former is obtained for 4 strap antenna with interval between adjacent current straps $W_d=0.23m$. The latter is obtained for 8 strap antenna with $W_d=0.35m$, which will be found to be the most suitable antenna configuration for the in-port antenna later. A value of N_z corresponding to a peak of the current spectrum (N_z^c) is 2.5 in both cases. The electron absorption ratio is maximized at frequency around 57.5-60MHz, which is somewhat lower than the optimum frequency band for the in-blanket antenna (62.5MHz - 65MHz). This implies that the midplane launching is a little bit disadvantageous for the current drive in a sense that the tritium resonance should be placed close to the center. The electron power absorption is reduced below 57.5MHz and above 62.5MHz by, respectively, enhancement of the tritium absorption and that of the deuterium and helium 4 absorption. The Be absorption ratio becomes appreciable from 57.5MHz and takes the maximum value (~24%) at 62.5MHz. Then, the current drive efficiency takes the maximum value at $f=60\pm 2.5MHz$ for both in-port antenna configurations.

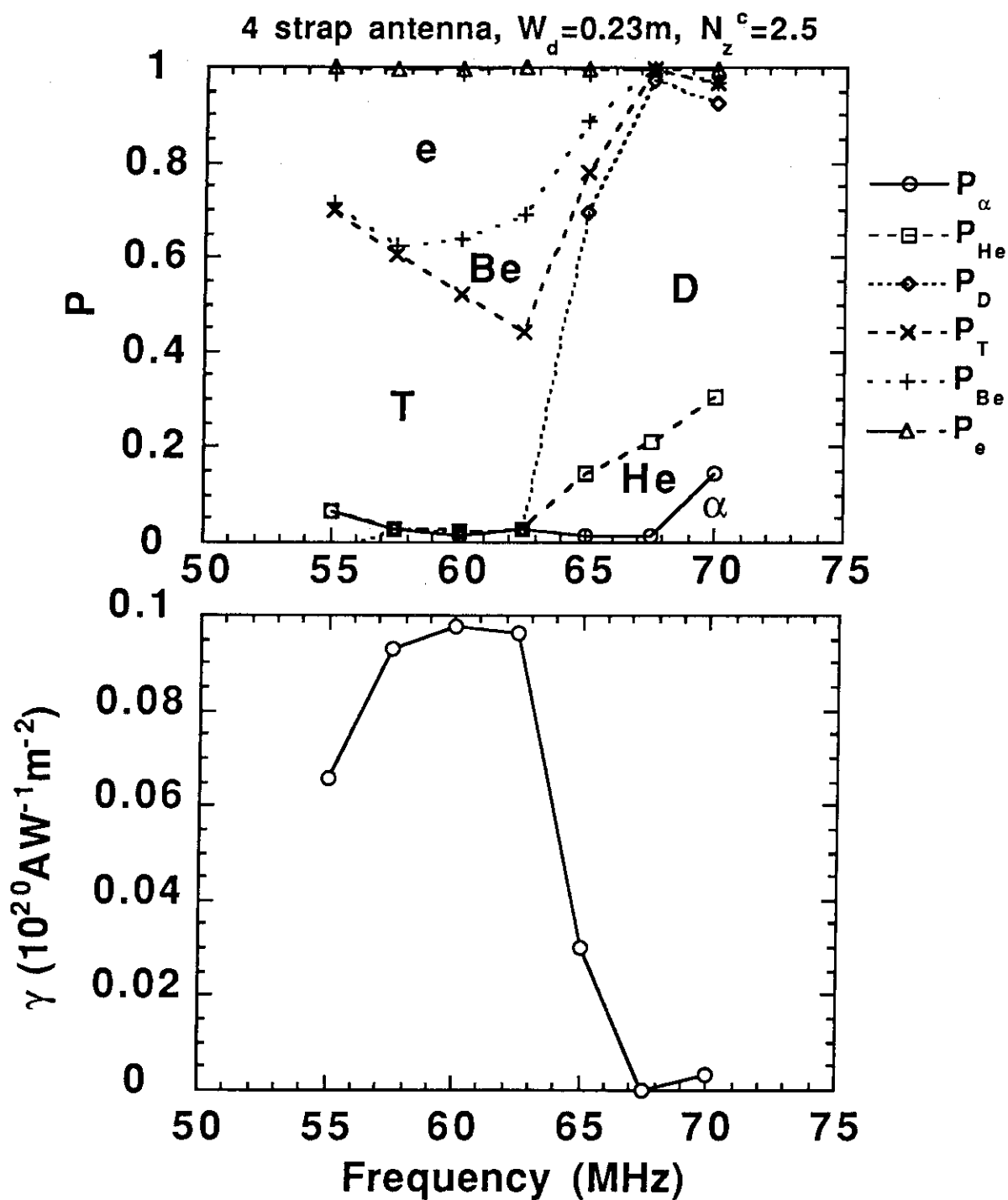


Fig. 2.5.1-1 Power partition and current drive figure of merit as a function of frequency. In-port antenna (number of current straps=4, $W_d=0.23\text{m}$), $N_z^c=2.5$, CD conditions.

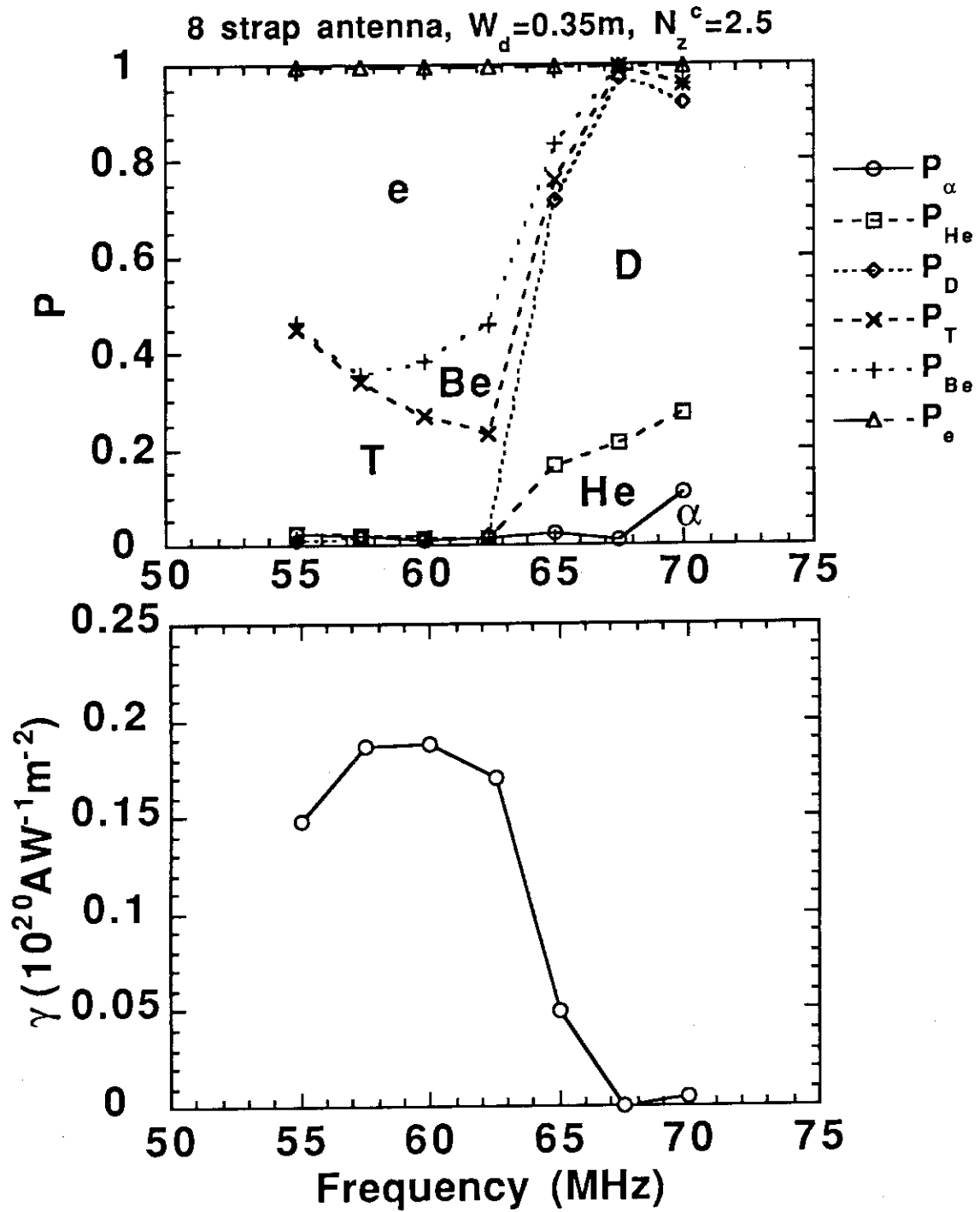


Fig. 2.5.1-2 Power partition and current drive figure of merit as a function of frequency. In-port antenna (number of current straps=8, $W_d=0.23\text{m}$), $N_z^c=2.5$, CD conditions.

2.5.2 Antenna configuration

2.5.2.1 Perpendicular access

First, we investigate optimum antenna configuration within framework of the JCT proposal. Namely we assume that an antenna plug is installed in a horizontal port of which direction is perpendicular to the toroidal direction and that an antenna box width (W_a) is 0.95m. For antenna locations and phases given by $z_j=(j-1)W_d$ and $\phi_j=(j-1)\Delta\phi$ and for constant antenna current densities, i.e. $J_j(z)=J_0$, the antenna current spectrum is given in Ref. [18] by

$$|J(k_z)| = 2J_0 \left| \frac{\sin(k_z W_z)}{k_z} \right| \left| \frac{1 - \cos N_A(\Delta\phi - k_z W_d)}{1 - \cos(\Delta\phi - k_z W_d)} \right|. \quad (2.5-1)$$

Here $\Delta\phi$, N_A and W_z represent a phase difference between adjacent current straps, number of current straps and a half width of each current strap, respectively. The dominant spectrum peak and its width are estimated to be

$$k_{p,m} = \frac{\Delta\phi - 2\pi m}{W_d} \quad \text{for } m=0, \pm 1, \pm 2, \dots \quad (2.5-2)$$

$$\Delta k_p = \frac{4\pi}{N_A W_d} \quad (2.5-3)$$

The value at the spectrum peak, $|J(k_{p,m})|$, decreases with increasing $|m|$, according to the factor $|\sin(k_{p,m} W_z) / k_{p,m}|$ in Eq. (2.5-1). Equations (2.5-2) and (2.5-3) indicate that the directivity becomes better with decreasing W_d (increasing number of current straps for fixed total antenna box width) but that the spectrum width does not change even with increasing number of current straps, since $N_A W_d$ is constant.

Figure 2.5.2-1 shows γ as a function of number of current straps in the toroidal direction, where frequency and N_z^c are 60MHz and 4.5, respectively. Here W_d is 0.4m for 2 strap antenna, 0.23m for 4 strap antenna, 0.153m for 6 strap antenna and 0.115m for 8 strap antenna. The current drive efficiency is saturated at $\gamma \sim 0.14 \times 10^{20} \text{ A W}^{-1} \text{ m}^{-2}$ even if number of current strap is increased above 4. The increase in γ from $N_A=2$ to $N_A=4$ is due to improvement

in the directivity. Figures 2.5.2-2 (a) and (b) compare the absorbed power and the driven current as a function of k_z between $N_A=2$ (a) and $N_A=4$ (b). For the case of $N_A=2$, larger negative current is produced due to poor directivity. The current drive efficiency is no longer determined by the directivity from $N_A=4$ to $N_A=8$. The saturation of γ is due to constant current spectrum width as indicated in Eq. (2.5-3). Thus, 4 strap array may be the best choice in the framework of the JCT proposal, considering power handling capability. However, W_d is only 0.23m even in this case.

Furthermore, a value of N_z^c giving the highest γ is about 4.5, as indicated in Fig. 2.5.2-3, which is apparently far from the optimum condition for FWCD in ITER. Figures 2.5.2-2 (b) and (c) compare the absorbed power and the driven current as a function of k_z between $N_z^c=4.5$ (b) and $N_z^c=2.5$ (c) for the case of $N_A=4$. The ion absorption at low- k_z (mainly by tritium and beryllium) is apparently larger for $N_z^c=2.5$ case. The ion absorption ratio is ~ 0.35 for $N_z^c=4.5$ and ~ 0.65 for $N_z^c=2.5$. On the other hand, the maximum current density is generated at similar k_z value in both cases. This implies that the choice of higher N_z^c value for better current drive efficiency is only to reduce ion absorption at low k_z . However, the antenna loading becomes reduced with increasing N_z^c . This unfavourable situation is due to relatively wide spectrum width, which is determined by a toroidal extension of the antenna array.

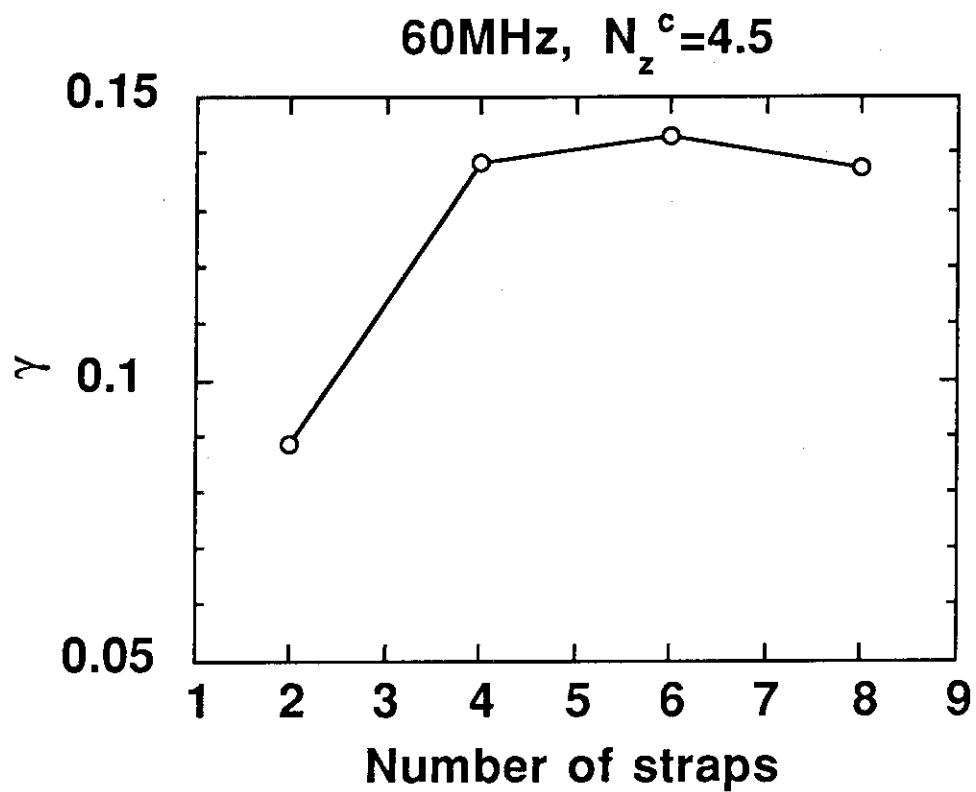
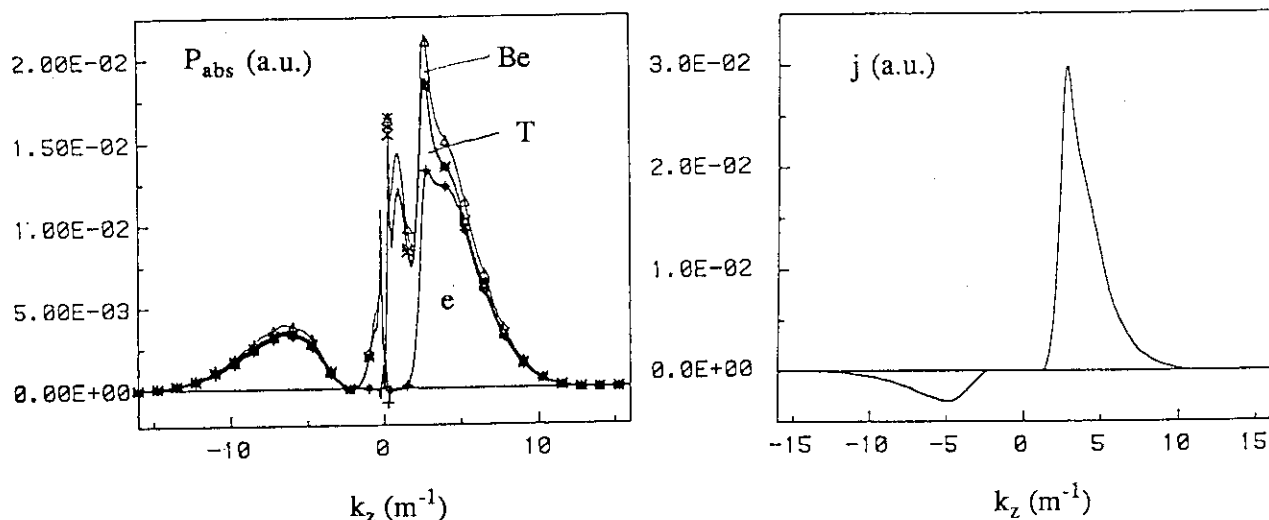
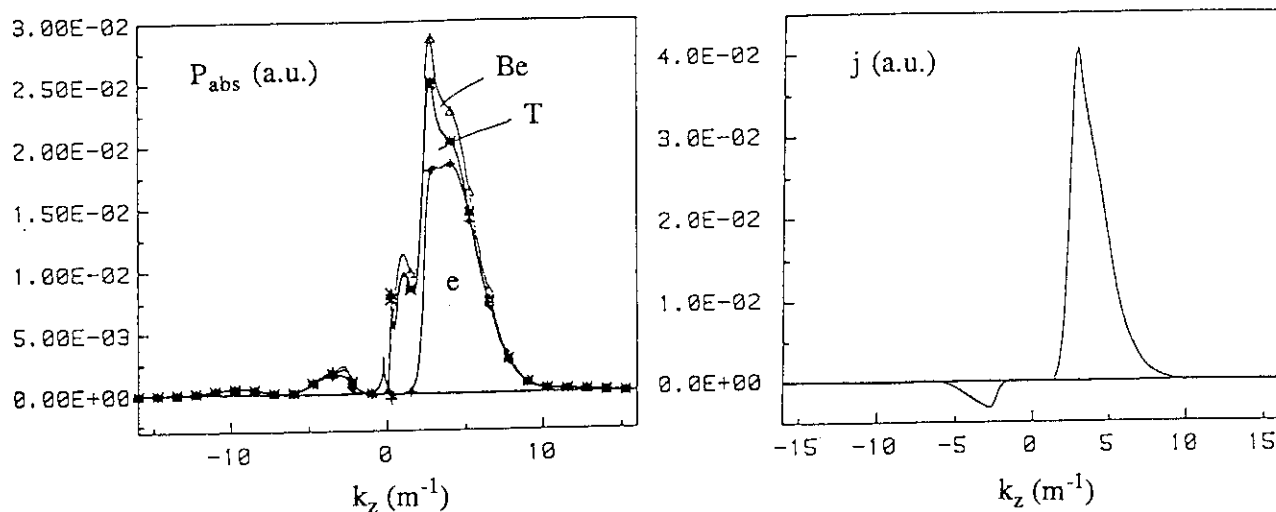


Fig. 2.5.2-1 Current drive figure of merit γ ($10^{20} \text{AW}^{-1} \text{m}^{-2}$) as a function of number of current straps in the toroidal direction. CD conditions.

(a) $N_A=2$ and $N_z^c=4.5$, $\gamma=0.089 \times 10^{20} \text{AW}^{-1}\text{m}^{-2}$



(b) $N_A=4$ and $N_z^c=4.5$, $\gamma=0.138 \times 10^{20} \text{AW}^{-1}\text{m}^{-2}$



(c) $N_A=4$ and $N_z^c=2.5$, $\gamma=0.098 \times 10^{20} \text{AW}^{-1}\text{m}^{-2}$

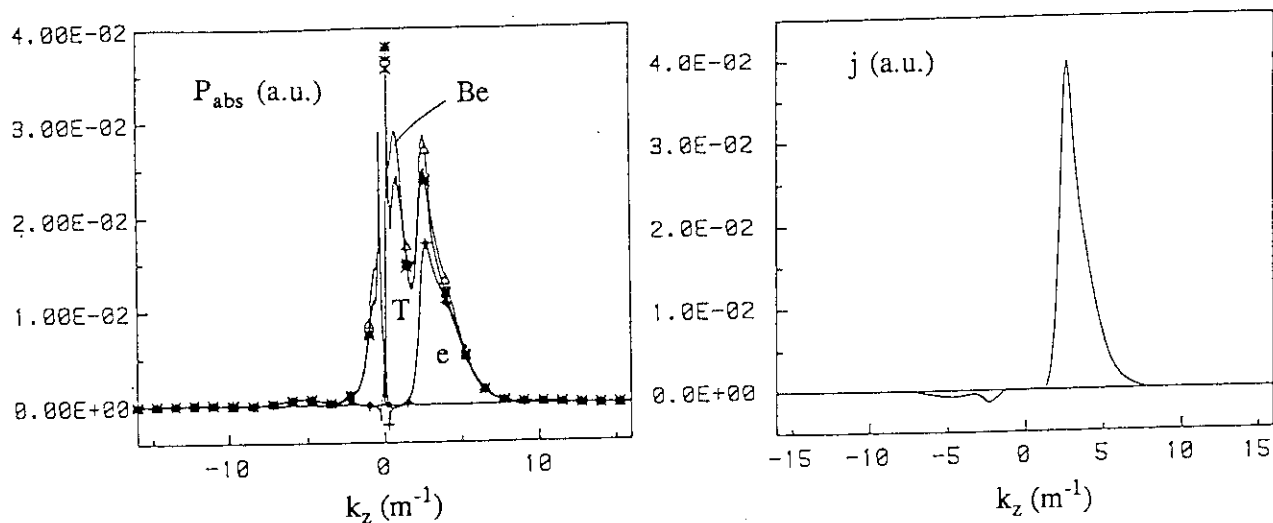


Fig. 2.5.2-2 k_z -spectra of absorbed power (left) and driven current (right). 60MHz, CD conditions.

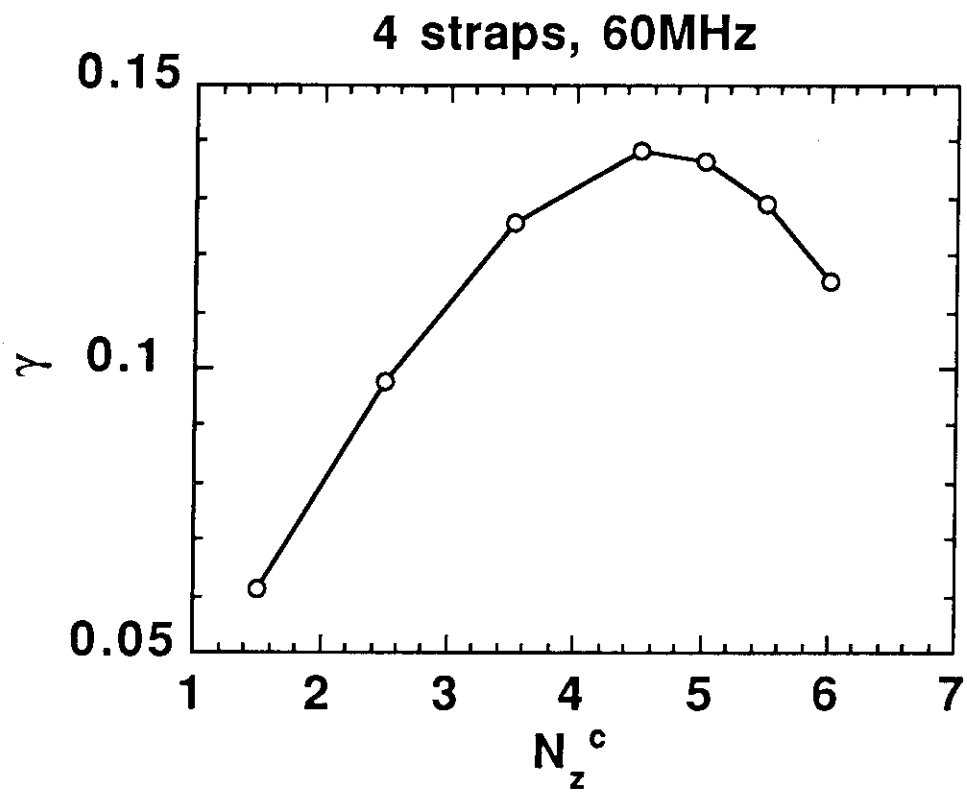


Fig. 2.5.2-3 Current drive figure of merit γ ($10^{20} \text{AW}^{-1} \text{m}^{-2}$) as a function of N_z^c . CD conditions.

2.5.2.2 Tangential access

Combination of adjacent tangential ports, whose directions are opposite each other, enables about 3m of toroidal width (W_a) of an antenna array. Figure 2.5.2.2-1 shows a concept of the in-port antenna installed in a pair of tangential ports. The two antenna plugs contact near the first wall to form a wide antenna array in the toroidal direction. 8 strap antenna is possible with a reasonable antenna element width ($W_d=0.35\text{m}$). The port width is taken as wide as possible without outside shields for the toroidal field coils. Separate shield blocks (shaded region in Fig. 2.5.2.2-1) are installed inside a port after installation of the antenna plug to ensure necessary shielding for the coils. Detailed description of the conceptual antenna structure is given in Sec. 2.5.6.

The current drive efficiency is calculated for this configuration and we obtain $\gamma=0.19\times 10^{20}\text{AW}^{-1}\text{m}^{-2}$ at $N_z^c=2.5$ as shown in Fig. 2.5.2.2-2. The absorbed power spectrum and the driven current spectrum at $N_z^c=2.5$ are shown in Fig. 2.5.2.2-3. The ion power absorption at low k_z is very small due to relatively narrow spectrum width. The value of N_z^c ($=2.5$) giving the highest current drive efficiency agrees with the single wave N_z value giving the highest current drive efficiency in this FWCD scenario. The fact indicates that the antenna current spectrum obtained by the 8 strap antenna with the tangential access is close to an ideal one.

Controllability of power partition between tritons and electrons is also much better for the 8 strap antenna than the 2 strap antenna as indicated in Fig. 2.5.2.2-4. Namely, 75% triton absorption at $N_z^c=1$ or 75% electron absorption at $N_z^c=3.5$ is possible in the former case, while in the latter case, those values are limited at 60% for triton absorption at $N_z^c=1$ or 50% for electron absorption at $N_z^c=3.5$. Fraction of the Be absorption via second harmonic resonance at low field side edge is about 10% and is almost independent of N_z^c .

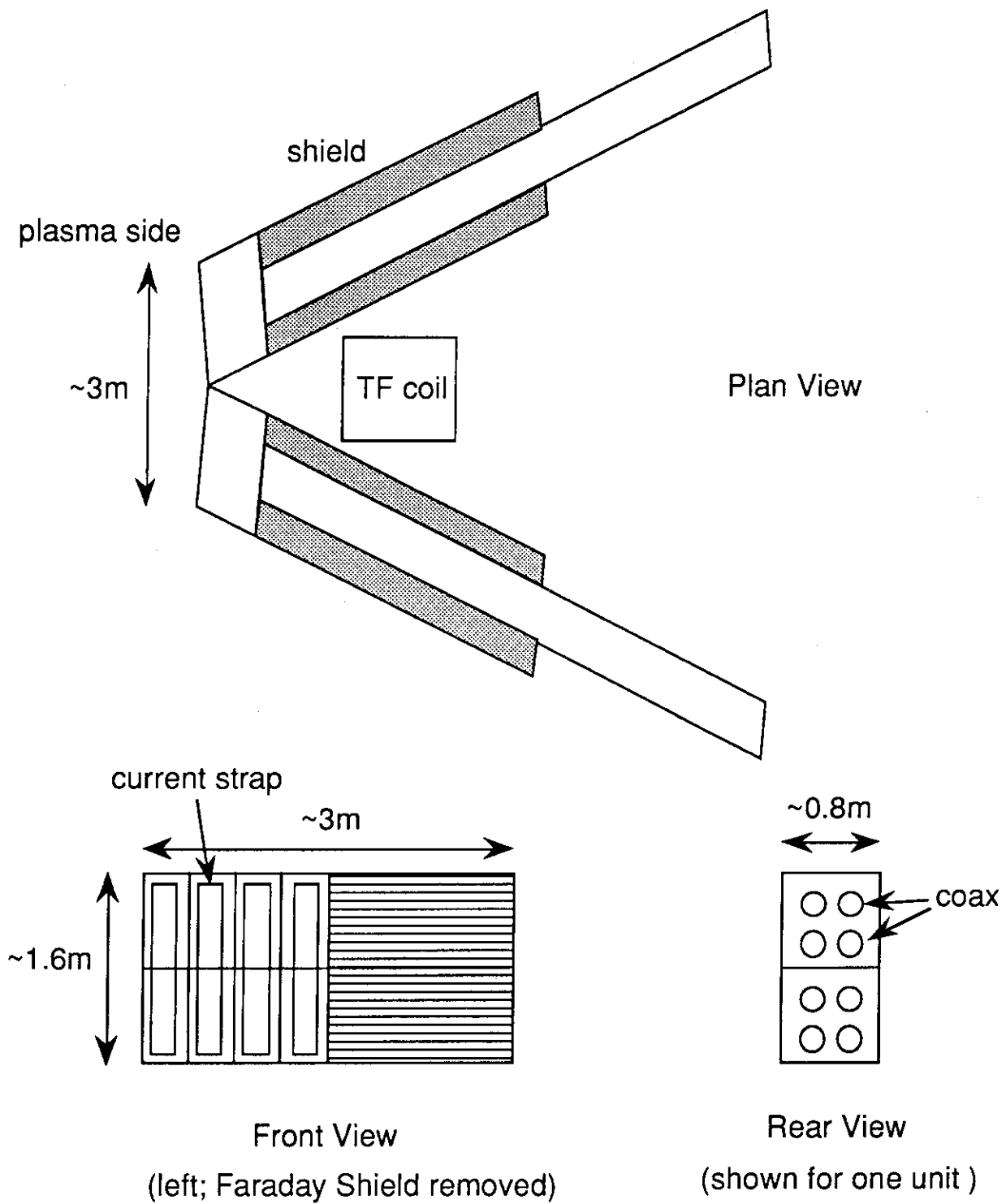


Fig. 2.5.2.2-1 Concept of the in-port antenna, which is combination of two antenna plugs installed in a pair of tangential ports to have a wide toroidal extension for better current drive and heating performance. 8 strap array is possible.

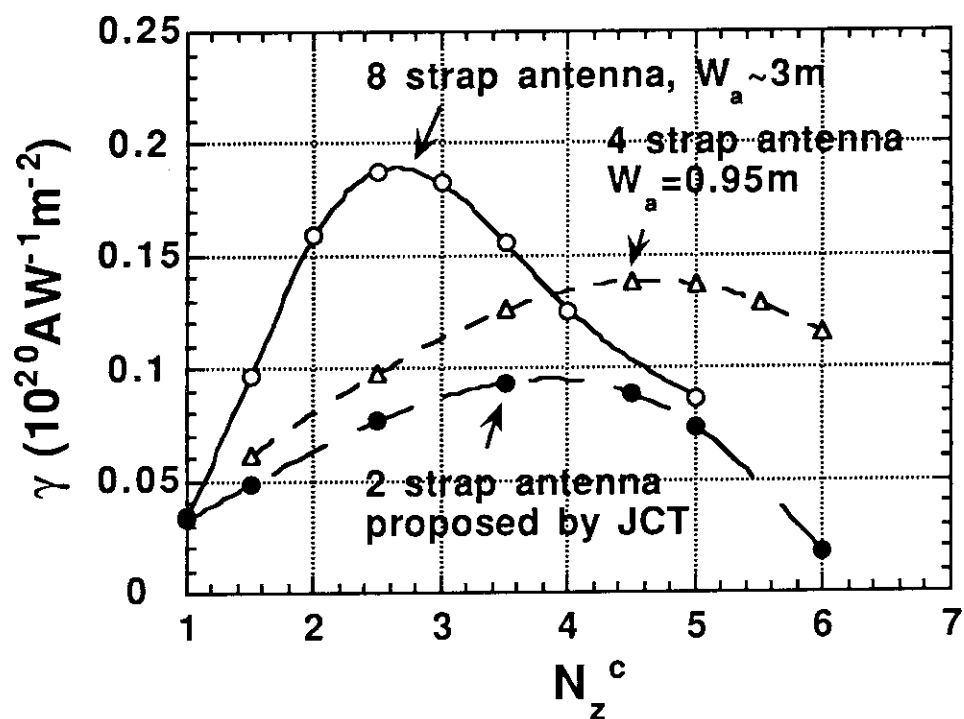


Fig. 2.5.2.2-2 Current drive figure of merit γ ($10^{20} \text{AW}^{-1} \text{m}^{-2}$) as a function of N_z^c . CD conditions.

$$N_A=8 \text{ and } N_z^c=2.5, \gamma=0.188 \times 10^{20} \text{ A W}^{-1} \text{ m}^{-2}$$

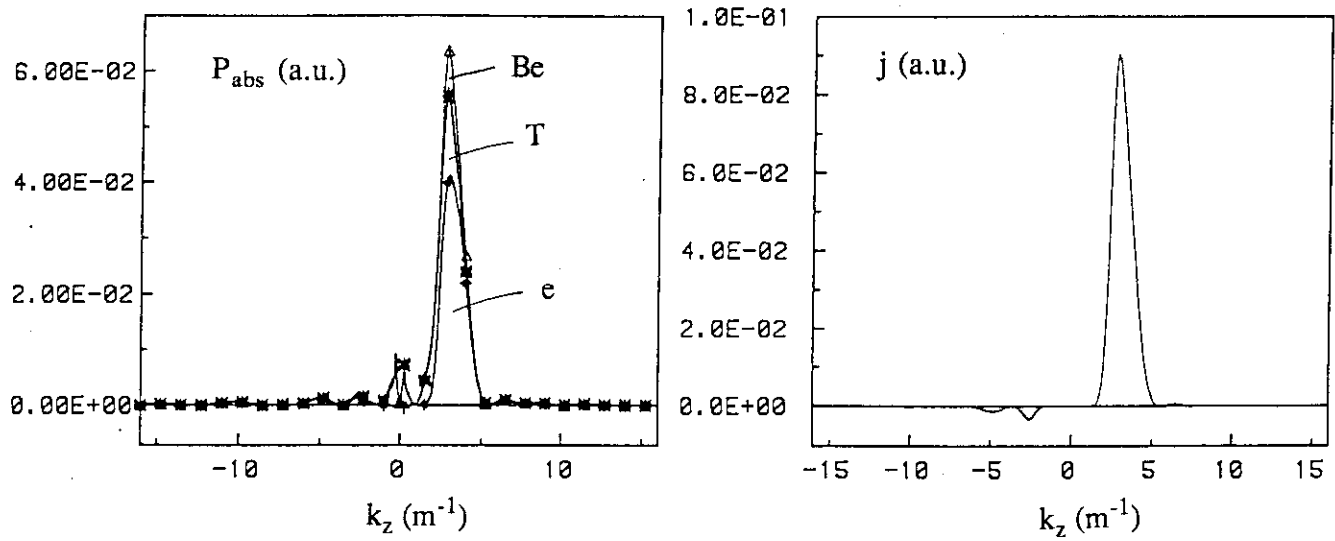


Fig. 2.5.2.2-3 k_z -spectra of absorbed power (left) and driven current (right) for 8 strap antenna with $W_a=3\text{m}$, 60MHz, CD conditions.

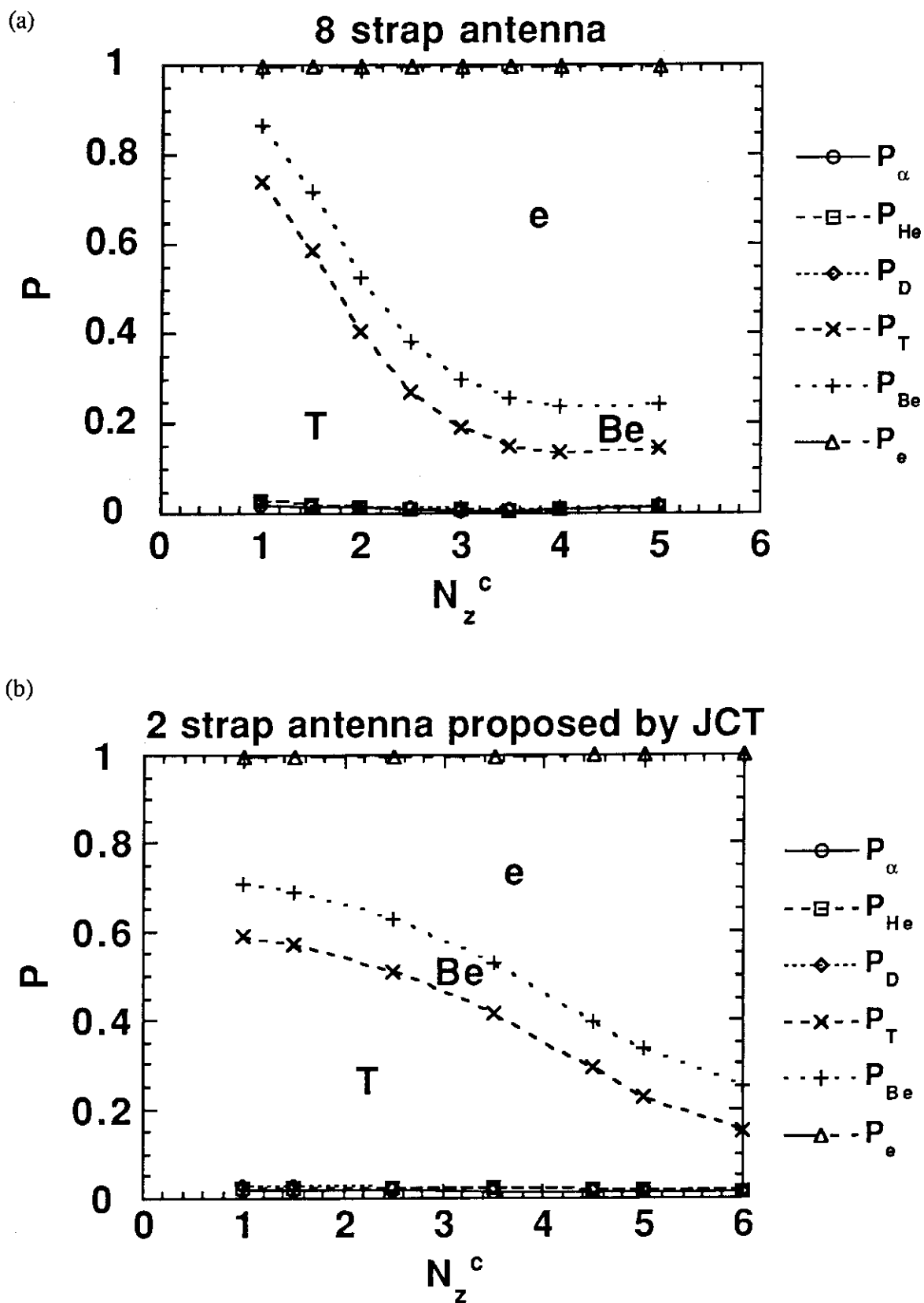


Fig. 2.5.2.2-4 Absorbed power by each species as a function of N_z^c for (a) 8 strap antenna with $W_a=3\text{m}$ and (b) 2 strap antenna with $W_a=0.95\text{m}$. Total absorbed power is normalized to be unity. 60MHz, CD conditions.

2.5.3 Current drive in OH conditions

The current drive performance of the 8 strap antenna with tangential access is also evaluated with OH conditions (see Table 2.2-2). Figure 2.5.3-1 shows the power partition among species and the current drive figure of merit as a function of N_z^c . Fraction of the ion absorption becomes larger even for higher range of N_z^c . At $N_z^c=4.5$, the electron power absorption ratio is only 40%. The highest current drive efficiency is $0.032 \times 10^{20} \text{AW}^{-1} \text{m}^{-2}$ (driven current = 0.83MA with 50MW injection power), which is obtained at $N_z^c=4.5$. However, for CD conditions, the optimum value of N_z^c is 2.5. Therefore, dynamical control of N_z^c is necessary if current drive is required from the OH phase. If not, the central ion heating mode automatically shifts over the central current drive mode in a course of a discharge, setting N_z^c to be 2.5 at 60MHz.

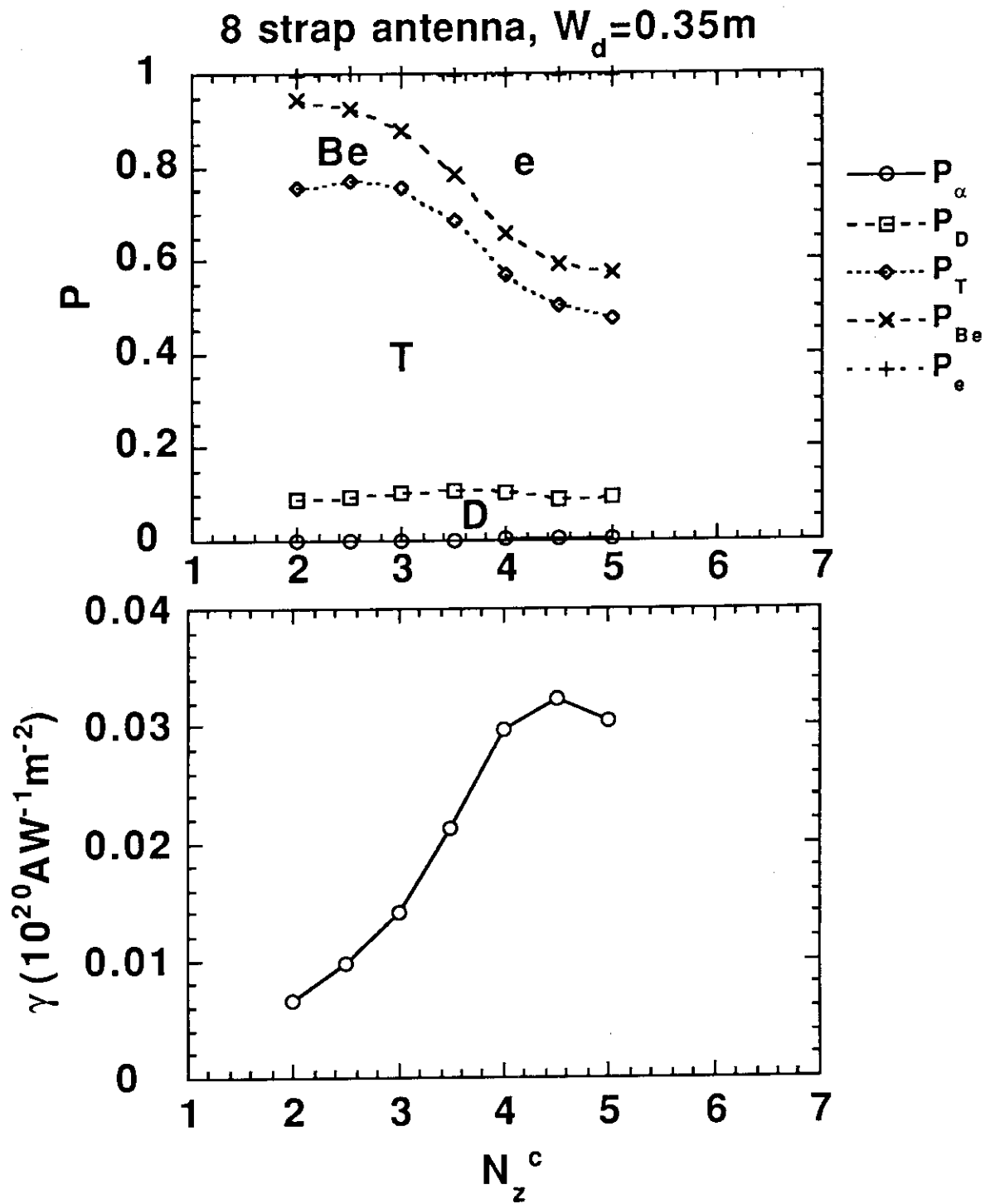


Fig. 2.5.3-1 Power partition and current drive figure of merit as a function of N_z^c . Number of current strap is 8, $W_d=0.35\text{m}$ and $f=60\text{MHz}$. OH conditions.

2.5.4 Effect of triton tail formation

We have also analyzed wave absorption with the one-dimensional full wave code incorporating a Fokker-Planck code [15] to check the effect of triton tail formation on the power partition between electrons and ions. The upper part of Fig. 2.5.4-1 shows power partition among species including triton tail ions as a function of frequency with fixed value of refractive index N_z at 2.5. It is found that the power absorption by triton tail is not so large at 60MHz, which is the optimum frequency for the current drive, i.e., about 25% of the power absorbed by thermal tritons. However, the lower part of Fig. 2.5.4-1 indicates that the triton tail absorption becomes important for N_z below about 2. This is due to relative reduction in power absorption by thermal tritons for low N_z value. The result suggests that the antenna current spectrum should be as sharp as possible to avoid enhancement of ion absorption due to the triton tail formation and to maximize the current drive efficiency.

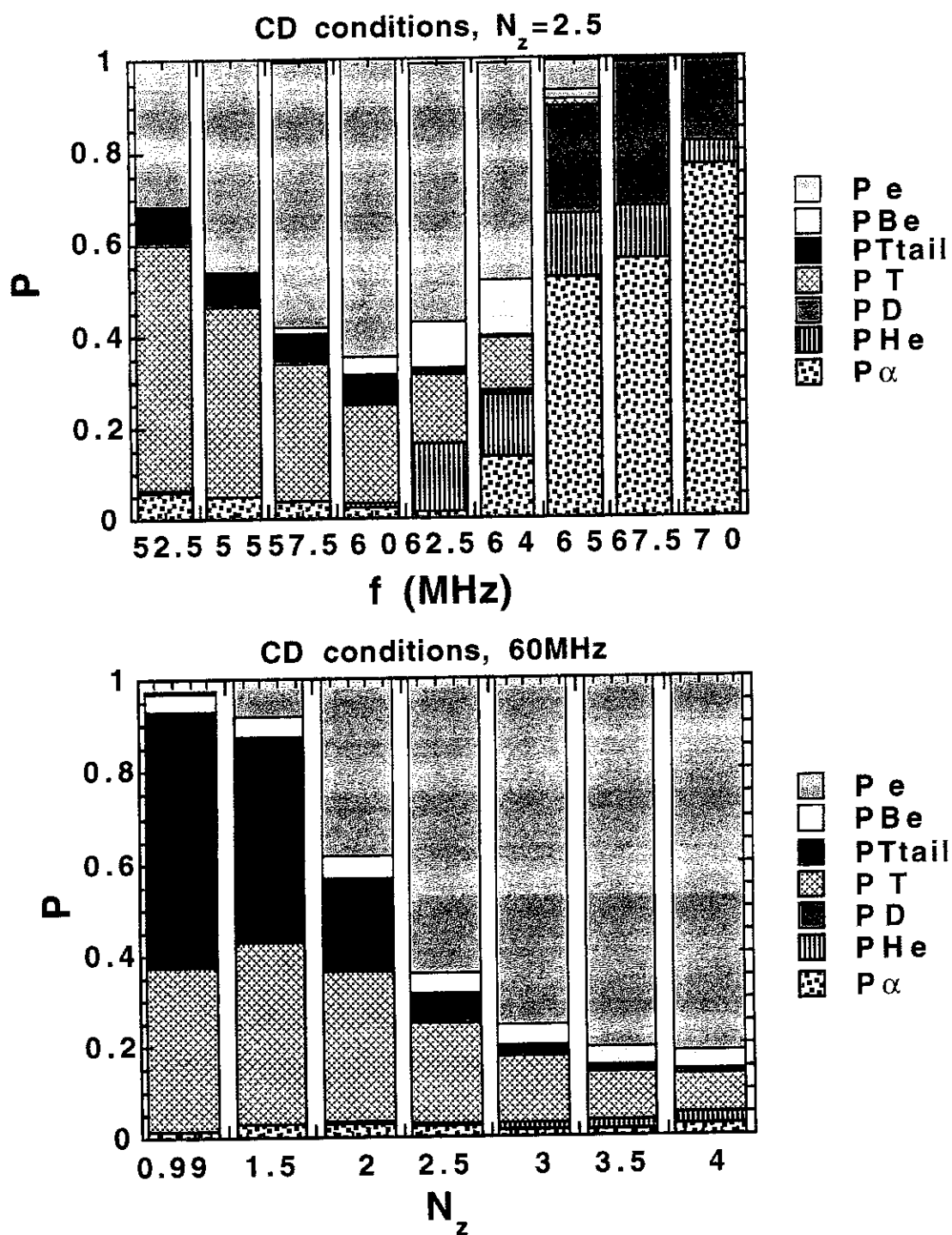


Fig. 2.5.4-1 Power partition among species including triton tail ions as a function of frequency (upper graph) and toroidal refractive index N_z (lower graph). CD conditions.

2.5.5 Two-dimensional calculation

Wave propagation and absorption are calculated by the two-dimensional full wave code taking the ITER plasma equilibrium into account. The equilibrium of ignition phase is used here. The central and edge safety factors are 1.0 and 3.7, respectively. A major radius position of the magnetic axis is 8.53m, where the toroidal field is 5.67T. The temperature and density profiles are artificially assumed to be the same as given for the CD parameters (see Table 2.2-1). The density profile of fusion alphas is determined from the density and temperature profiles of the background plasma. An average energy of the slowing down distribution of α particles is used as the temperature of α particles (the central value is 1.88MeV). The poloidal angle of the in-port antenna is assumed to extend from -15° to 15° .

Power deposition and driven current profiles

Figures 2.5.5-1~3 show the calculation results for 60MHz and the toroidal mode number, $n=26$ ($N_z=2.4$). The wave fields are strongly converged toward the magnetic axis (Fig. 2.5.5-1). The waves are heavily damped near the center by the electron absorption (Fig. 2.5.5-2). The rest of the wave power is then absorbed by the triton second harmonic resonance, since the triton resonance layer is located about 0.4m inside from the magnetic axis. Fractions of power absorption by electrons and tritons to the total absorbed power amount to 83% and 16%, respectively. Absorption by other ion species is negligibly small (e.g., 0.01% by Be). This result on the power partition is considerably different from that of the 1-D calculation which is shown, for example, in Fig. 2.5.1-2. For 1-D case, 62% by electrons, 25% by tritons and 11% by berylliums. The reason why the triton absorption is reduced in the 2-D calculation is the outward shift of the magnetic axis as mentioned above. The reason why the Be absorption is reduced in the 2-D calculation is that the Be cyclotron resonance layer on the low field side shifts more outside due to the poloidal field. Those effects are not taken into account in the 1-D code. The power deposition and driven current profiles averaged over the magnetic surface are indicated in Fig. 2.5.5-3. The current density profile is very peaked near the center similarly as for the in-blanket antenna (see Fig. 2.4.2-8).

Dependence on the toroidal mode numbers

Figure 2.5.5-4 shows the power partition and the current drive efficiency as a function of the toroidal mode number, n . Optimum range of the toroidal mode number for the current drive is 20~30 ($N_z=2\sim 2.8$). The maximum current drive efficiency is obtained at $n\approx 26$ ($N_z\approx 2.4$). The electron power absorption is almost constant ($\sim 90\%$) above $n\sim 30$. It decreases rapidly with decreasing n below $n\sim 20$. Power absorption by fusion α 's and berylliums is negligibly small over a wide range of n ($n=5\sim 54$).

Current drive efficiency

The current drive figure of merit is evaluated with the 2-D calculation results, taking the antenna current spectrum into account. The antenna current spectrum for the 8 strap antenna (JAERI proposal, tangential access) is shown in Fig. 2.5.5-5. The estimated γ is $0.33\times 10^{20}\text{AW}^{-1}\text{m}^{-2}$, which is much higher than that obtained by the 1-D code ($0.19\times 10^{20}\text{AW}^{-1}\text{m}^{-2}$). Even if the improved absorption ratio of the electrons in the 2-D calculation mentioned above is taken into account, γ value by the 2-D code is about 30% better than that obtained by the 1-D code. The reason may be explained by the focusing effect of the wave propagation in the 2-D calculation.

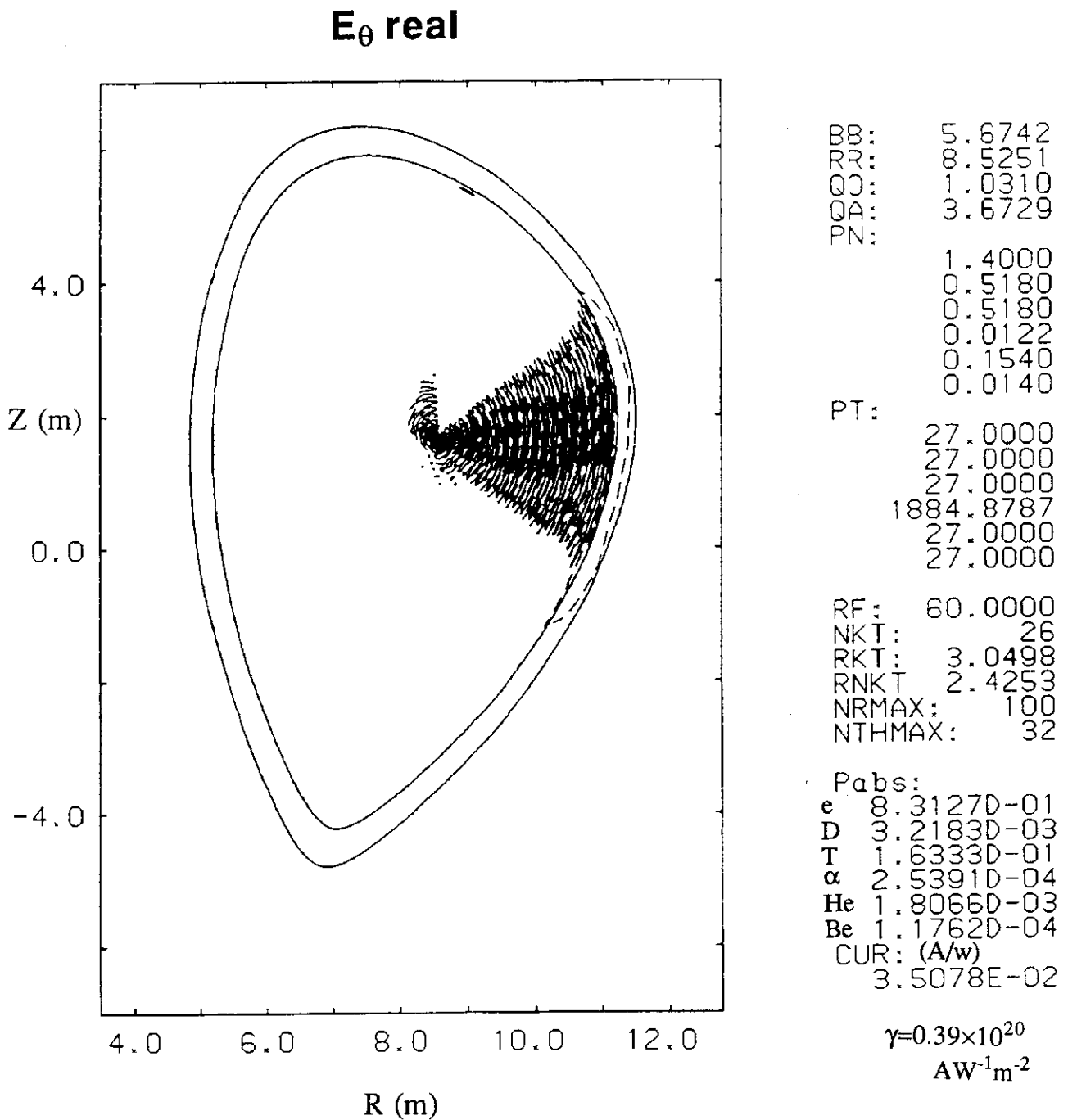


Fig. 2.5.5-1 Contour plots of the wave electric field (E_θ) in the poloidal cross-section for the ITER equilibrium in ignition. 60MHz, $n=26$, in-port antenna (midplane launching) and CD conditions.

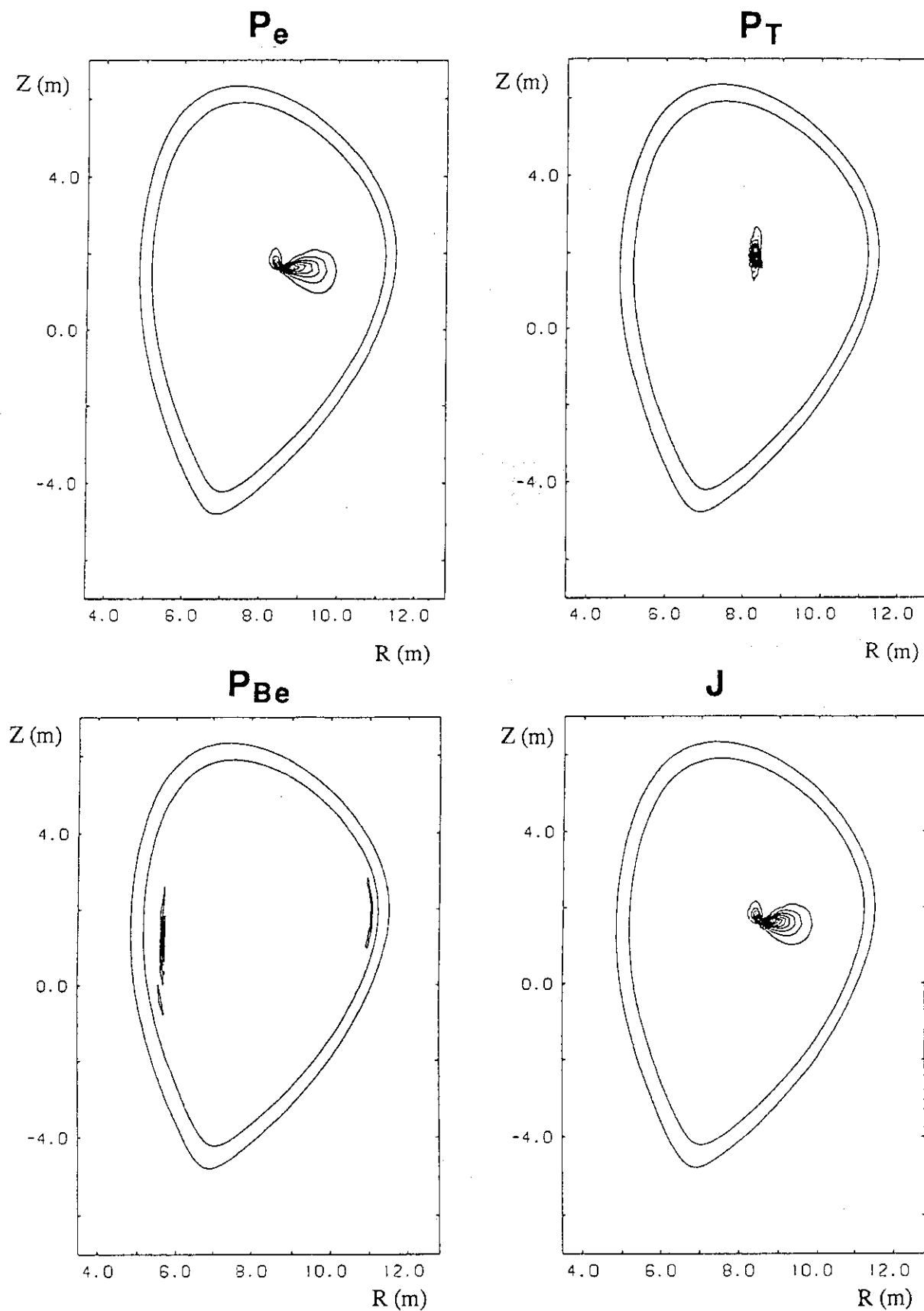
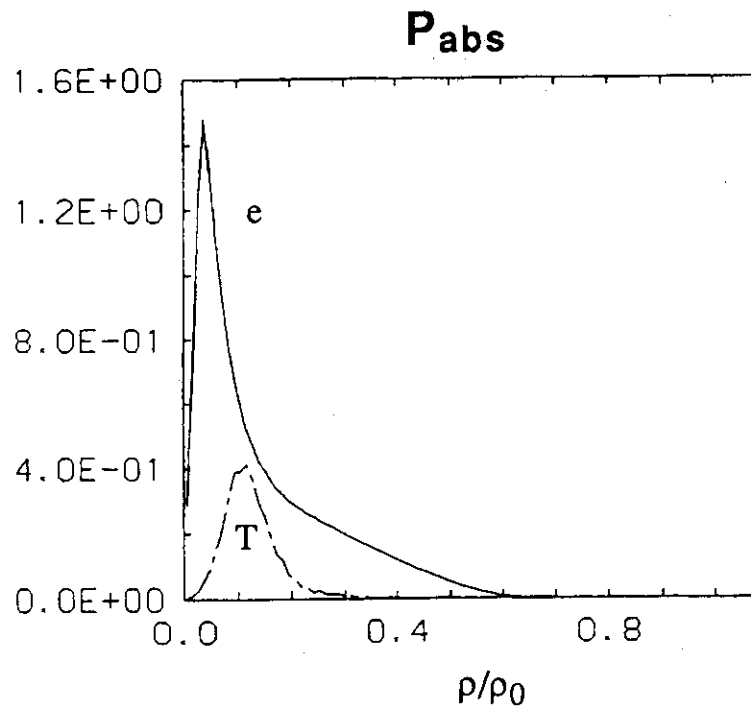


Fig. 2.5.5-2 Contour plots of the electron power absorption (P_e) in the poloidal cross-section for the ITER equilibrium in ignition. 60MHz, $n=26$, in-port antenna (midplane launching) and CD conditions.

(a)



(b)

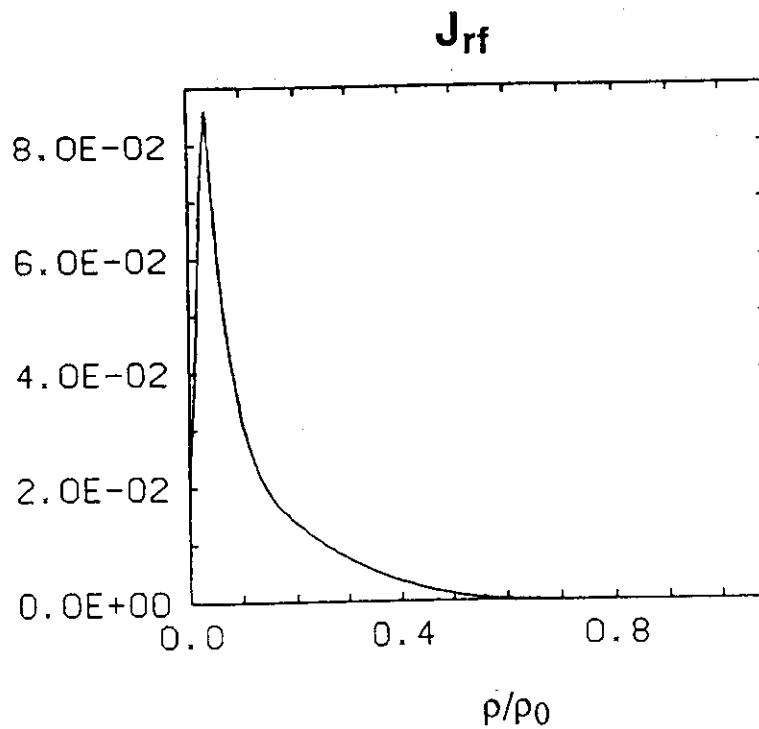


Fig. 2.5.5-3 Radial profiles of (a) the electron and ion power absorption and (b) the driven current for the ITER equilibrium in ignition. 60MHz, $n=26$, in-port antenna (midplane launching) and CD conditions.

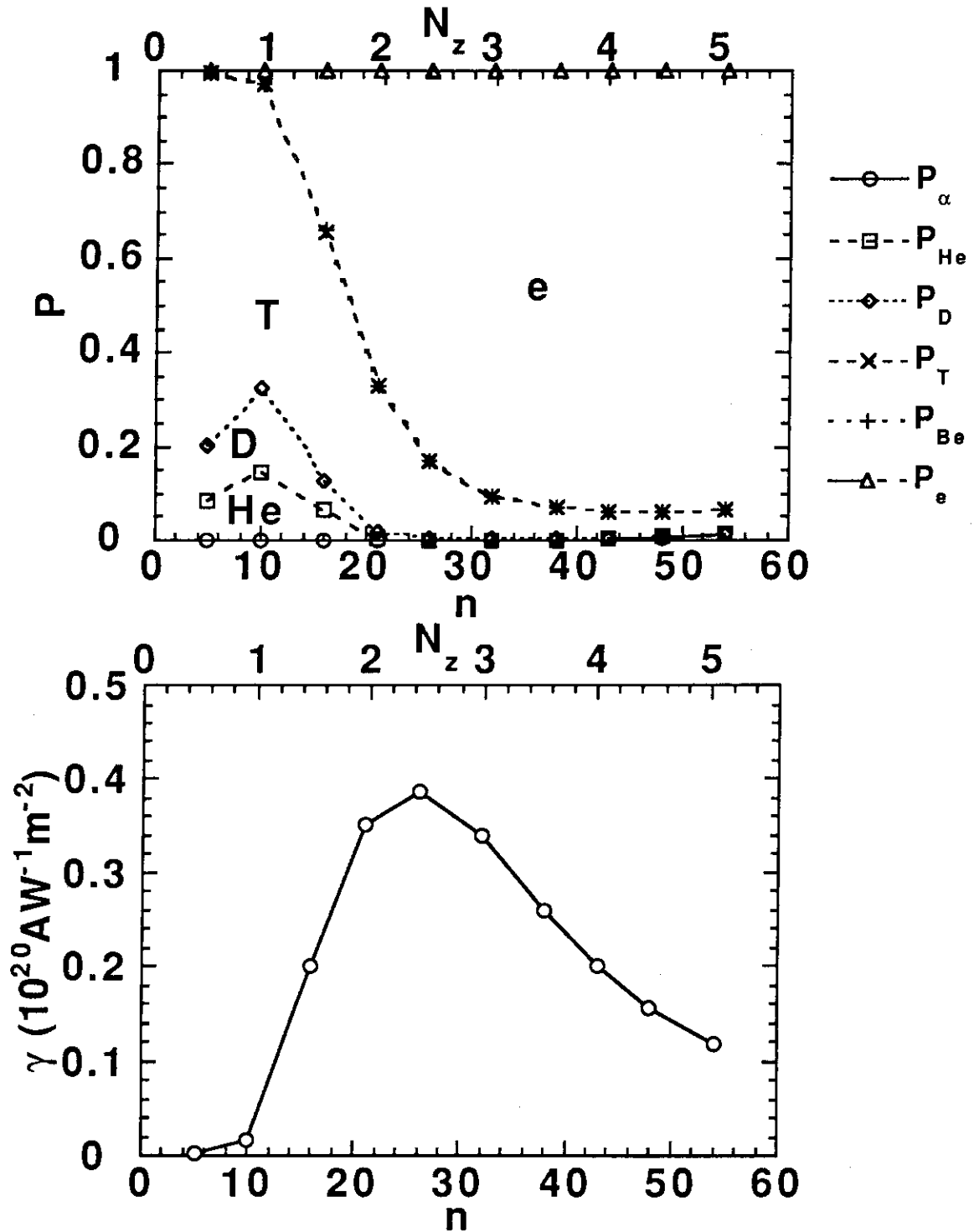


Fig. 2.5.5-4 Power partition and current drive figure of merit as a function of the toroidal mode number, n (or the toroidal refractive index, N_z), calculated by the 2-D full wave code taking ITER equilibrium into account. 60MHz, in-port antenna, CD parameters.

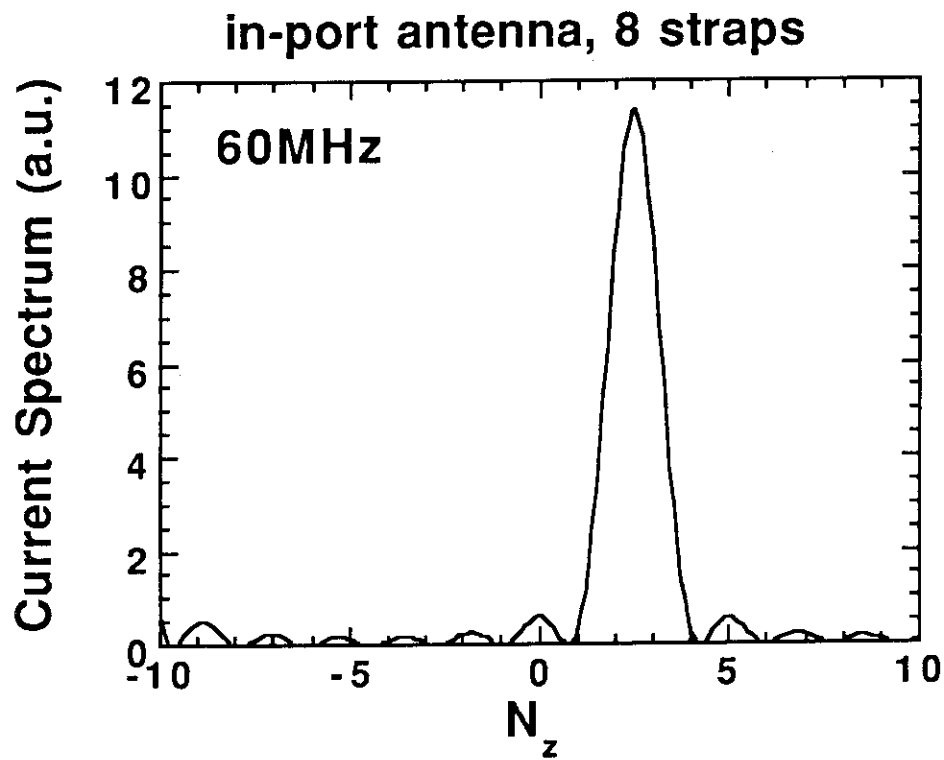


Fig. 2.5.5-5 Antenna current spectrum against the toroidal refractive index, N_z , for in-port antenna (tangential access, 8 straps) at 60MHz. Interval between adjacent straps=0.36m, width of current straps=0.18m, phase difference between adjacent straps=64.8°.

2.5.6 Concept of antenna structure

An in-port antenna designed for the ITER ICRF system is shown in Figs. 2.5.6-1(a), (b) and (c). As mentioned in Sec. 2.5.2, we need a port as wide as possible in order to have a coherent N_{\parallel} spectrum which is effective to the current drive. So that we have made conceptual design of the in-port antenna for a wide tangential port with the toroidal width of 1.5 m and a tangential angle of 74° or -74° (actually almost perpendicular) proposed from Japan. The in-port antenna consists of 8 current straps (4 current straps in the toroidal direction and 2 current straps in the poloidal direction), an open type of Faraday shield and an antenna casing. Then, the 8 current straps with two antennas can be aligned near the radial position of the first wall in the toroidal direction by providing two adjacent tangential ports in mirror symmetry, which leads to form a more coherent N_{\parallel} spectrum. Main antenna material is stainless steel, and some part of its surface where rf current flows is plated with copper. Also, plasma facing surfaces are coated with low Z materials such as Be.

The toroidal interval between adjacent current straps is 0.36 m so as to have $N_{\parallel\text{peak}} = 2.5$ for phase difference between adjacent current straps, 65° at 60 MHz. The poloidal length of the current straps is 0.69 m which is shorter than $\lambda/4$ with considering the wavelength reduction (60 - 70 %) by the additional capacitance due to Faraday shield bars. The gap between the current strap and the side plate of the casing or the septum is 0.08 m, parallel to the magnetic field. This value may be set as widely as possible to couple rf power of 2 MW into the plasma from one current strap. The perpendicular gap between the current strap and the upper plate of the casing is 0.03 m which is designed from a viewpoint of not only the voltage stand-off but also the impedance matching between the current strap and the radial feeder section. The distance between the current strap and the back plate is in a range of 0.2 - 0.55 m, because it has to be optimized so as to obtain sufficient coupling resistance from further coupling calculations. The current strap is double structure to flow the coolant of water in its inside. Its support points are a short-circuited plate and a ridged waveguide support. The cut-off frequency of the ridged waveguide support is about 47 MHz. It is possible that its cut-off frequency is reduced by 20 - 30 % by extending its height (poloidal length) to about 0.7 m and its arm length to about 0.5 m if its mechanical strength is sufficient. The radial length of the

ridged waveguide support is fairly shorter than the wavelength so that its electric discontinuity is expected to be small. An 8-inch coaxial line with the characteristic impedance, $30\ \Omega$ is connected to the other side of the ridged waveguide support.

The Faraday shield is composed of bars not parallel to the total magnetic field but parallel to the toroidal magnetic field. So that it is not tilted to the horizontal plane, because the tilted Faraday shield can not function its merit of reduced impurity generation in a wide range of q values, and further such merit is not found definitely in the experiments on the DIII-D tokamak if low- Z material is applied for the Faraday shield [19]. The diameter of the bar is 0.05 m. The poloidal interval between the bars is about 0.1 m and the radial gap between the bar and the current strap is about 0.02 m. These values are chosen so as to set the wavelength reduction to be a desirable value. The septa are slotted to radiate rf magnetic field effectively. They also are a kind of support for Faraday shield bars. The bar is round at the corners to reduce the thermal stress, and the additional poloidal bar supports are provided near the corners to reduce the mechanical stress to the bars due to the electromagnetic force induced by plasma disruption.

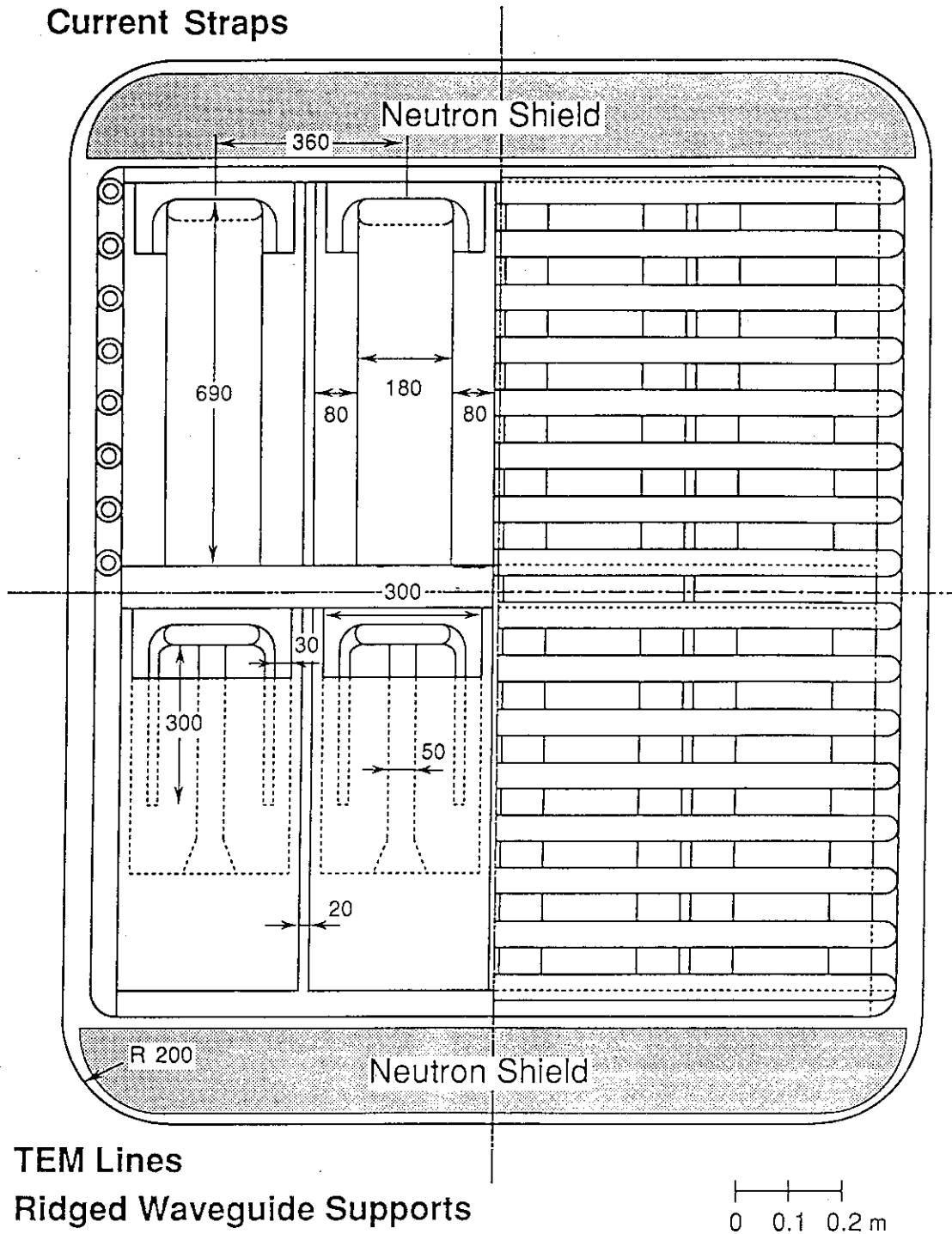


Figure 2.5.6-1(a) Front view of ITER in-port antenna.

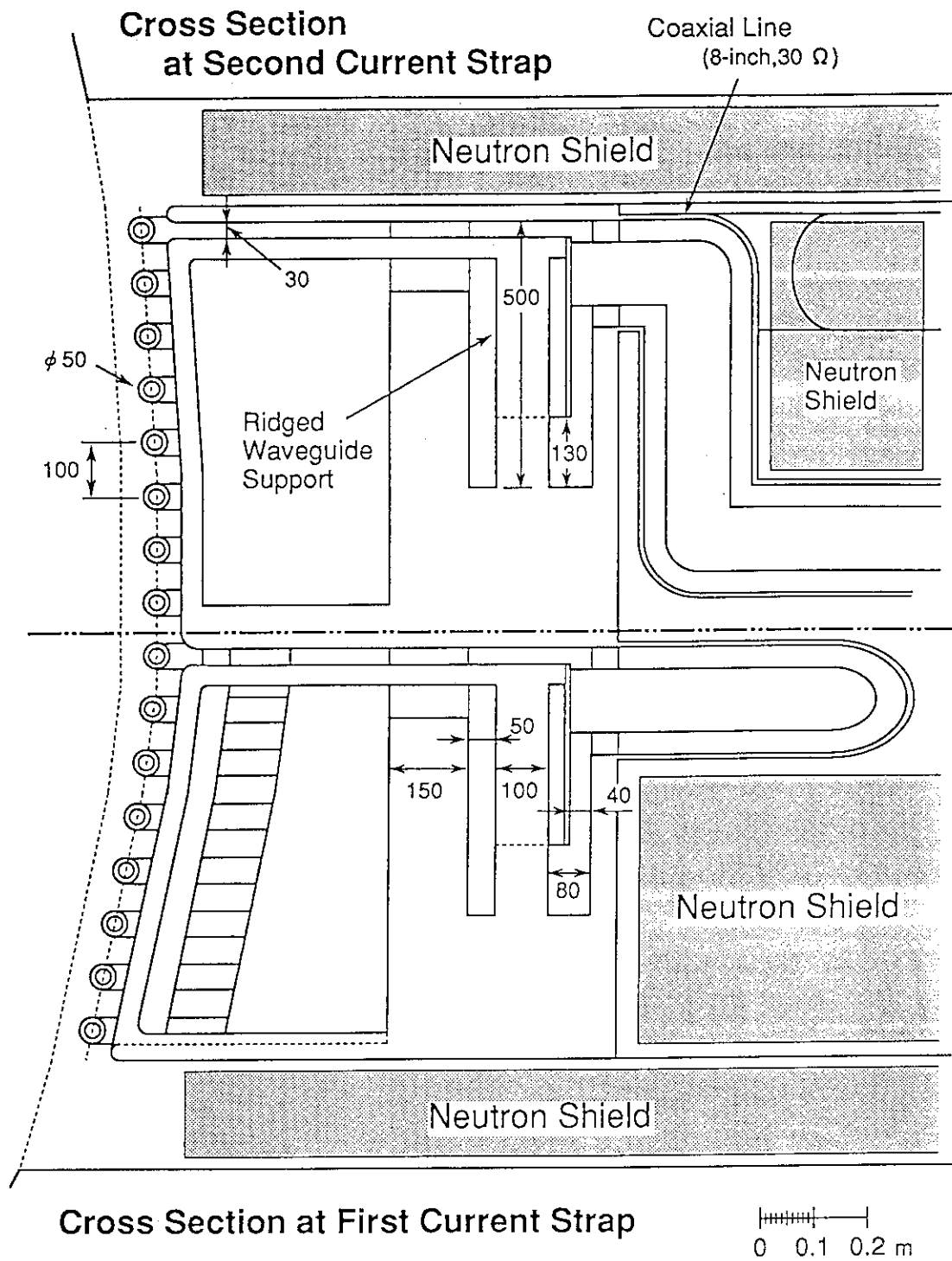


Figure 2.5.6-1(b) Poloidal cross section of ITER in-port antenna.

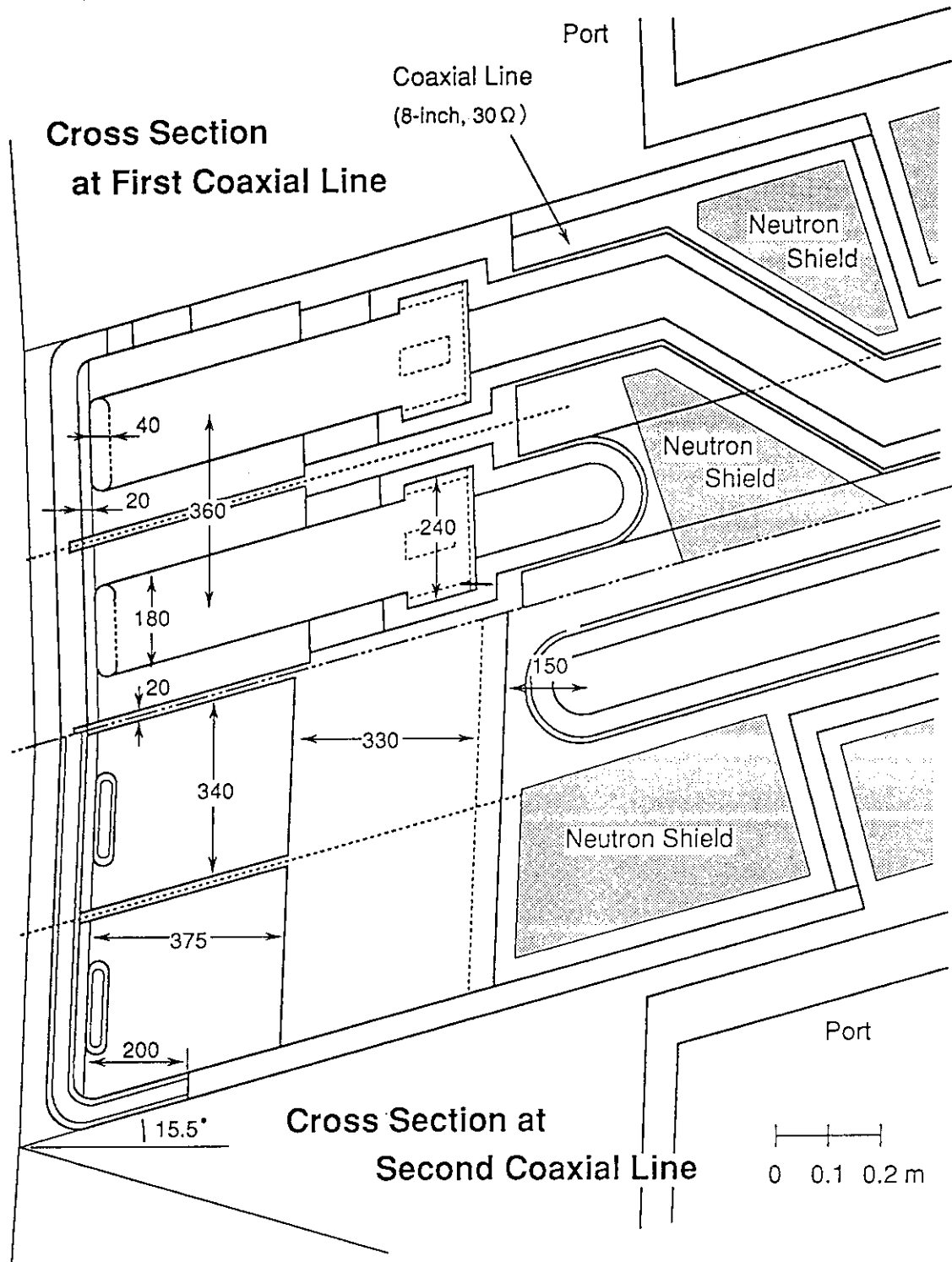


Figure 2.5.6-1(c) Toroidal cross section of ITER in-port antenna.

2.5.7 Antenna-plasma coupling calculation

The antenna-plasma coupling is one of the most important points for designing FWCD antenna in ITER. The coupling properties of the 8×2 antenna array which is installed in two adjacent ports are evaluated by the coupling code with a cold dispersion relation and a slab plasma model [20]. The antenna model and the electron density profile for the coupling calculation are shown in Fig. 2.5.7-1. The electron density profile is assumed to be

$$n_e(r) = (n_e(0) - n_{eb}) \left\{ 1 - \left(\frac{r}{R_a} \right)^2 \right\}^2 + n_{eb} \text{ inside the separatrix } (r < R_a),$$

and

$$n_e(r) = n_{eb} \exp \left(- \frac{r - R_a}{\lambda_e} \right) \text{ in the scrape-off layer } (R_a < r < R_b),$$

where $n_e(0)$ is a central electron density ($1.4 \times 10^{20} \text{ m}^{-3}$), n_{eb} is an edge electron density which is 0.43 times of central density and λ_e is an e-folding length of the electron density profile in the scrape-off layer (2 cm). The antenna length, the toroidal interval of antenna array and the current strap width are assumed to be 69 cm, 36 cm and 18 cm, respectively. The characteristic impedance of the transmission line and the frequency is 30 Ω and 60 MHz, respectively.

Figure 2.5.7-2 shows the dependence of loading resistance on the toroidal refractive index corresponding to a peak of the antenna current spectrum (N_z^c). The loading resistance increases with decreasing N_z^c and the optimum N_z^c value for fast wave current drive with high efficiency is low value, that is 2.5, so that the coupling properties are much better than the conventional FWCD antenna in present tokamaks. The 8×2 antenna array has a high directivity and a sharp N_z spectrum, as shown in Fig. 2.5.7-3. However, the dependence of coupling on the frequency is not so wide band due to using a half wavelength resonance for obtaining high loading resistance as shown in Fig. 2.5.7-4. The dependence of coupling on the distance between antenna and return wall is shown in Fig. 2.5.7-5. The maximum loading resistance can be obtained at the distance between antenna and return wall of 57 cm, which may be about half wavelength resonance along the current strap. Figure 2.5.7-6 indicates that the loading resistance is not sensitive to the electron density, as long as over the cut-off density of excited N_z spectrum. It is very effective for heating at the low electron density regime in the ITER ignition scenario.

The wide Faraday shield/separatrix separation during FWCD operation is important for realistic ITER design. The loading resistance of an antenna is demanded to be over $4.2\ \Omega$ for the coupled power of 100 MW, where the stand-off voltage is assumed to be 30 kV. Figure 2.5.7-7 shows the dependence of loading resistance on the separatrix-Faraday shield distance. The loading resistance at the Faraday shield/separatrix separation of 10 cm is about $6\ \Omega$ per an antenna, where the Faraday shield thickness is 6 cm and the Faraday shield/current strap separation is 1 cm. If we can use the back Faraday shield (new concept [21]), the full power operation (100 MW) can be available with the Faraday shield/separatrix separation of 19 cm.

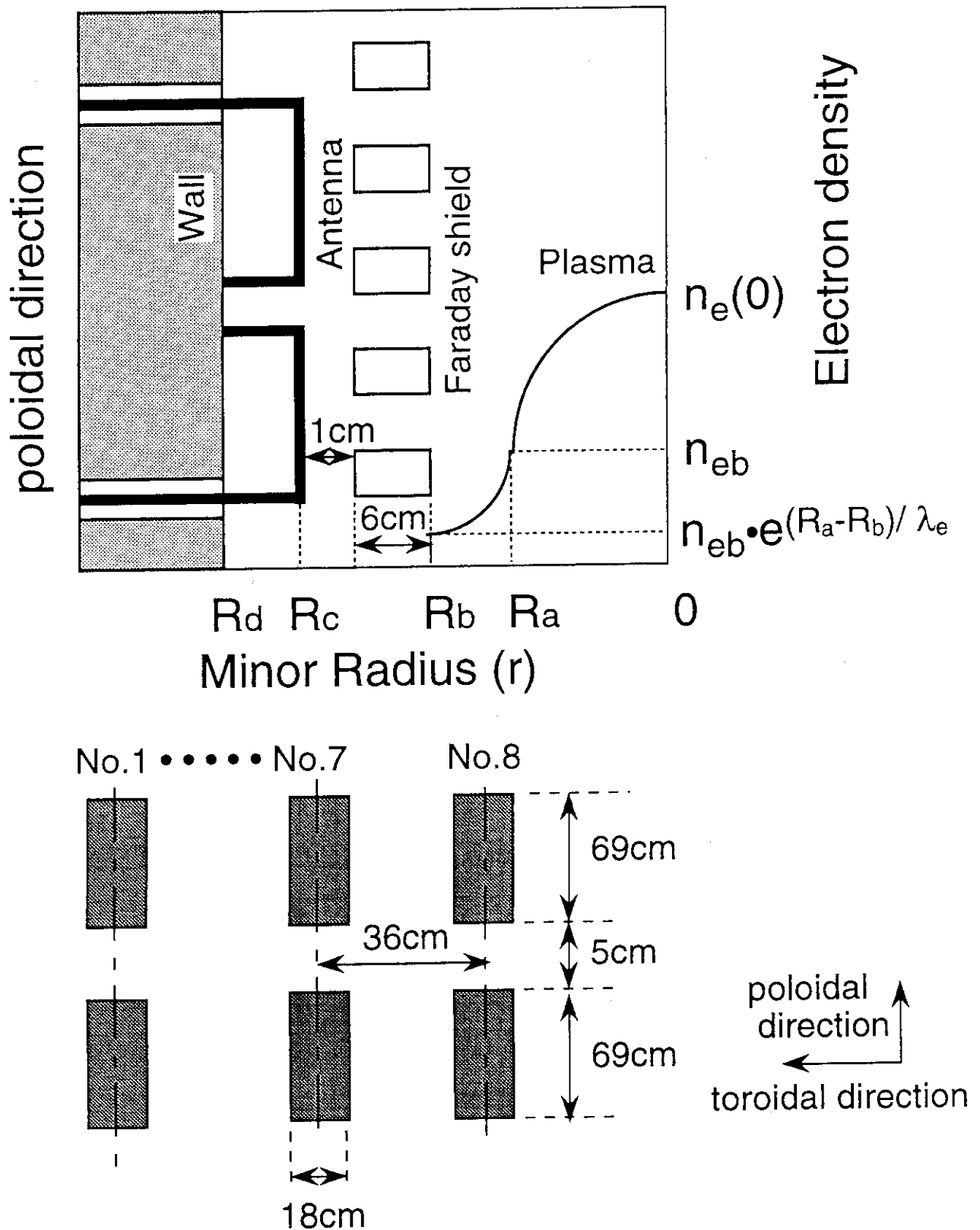


Fig.2.5.7-1 Antenna model and electron density profile for coupling calculation

$$R=8.1\text{ m}, B_t(0)=6\text{ T}, R_a=3\text{ m}, R_b=3.1\text{ m}, Z_0=30\Omega$$

$$n_e(0)=1.4 \times 10^{20}\text{ m}^{-3}, n_{eb}=0.43 \cdot n_e(0), \lambda_e=2\text{ cm}$$

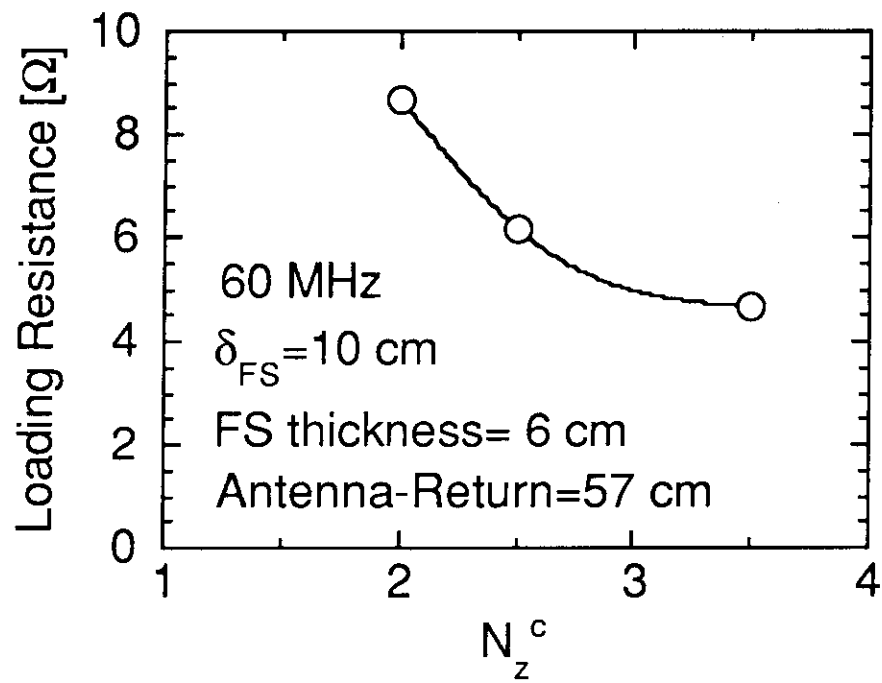


Fig. 2.5.7-2 Dependence of loading resistance on the toroidal refractive index (N_z^c)

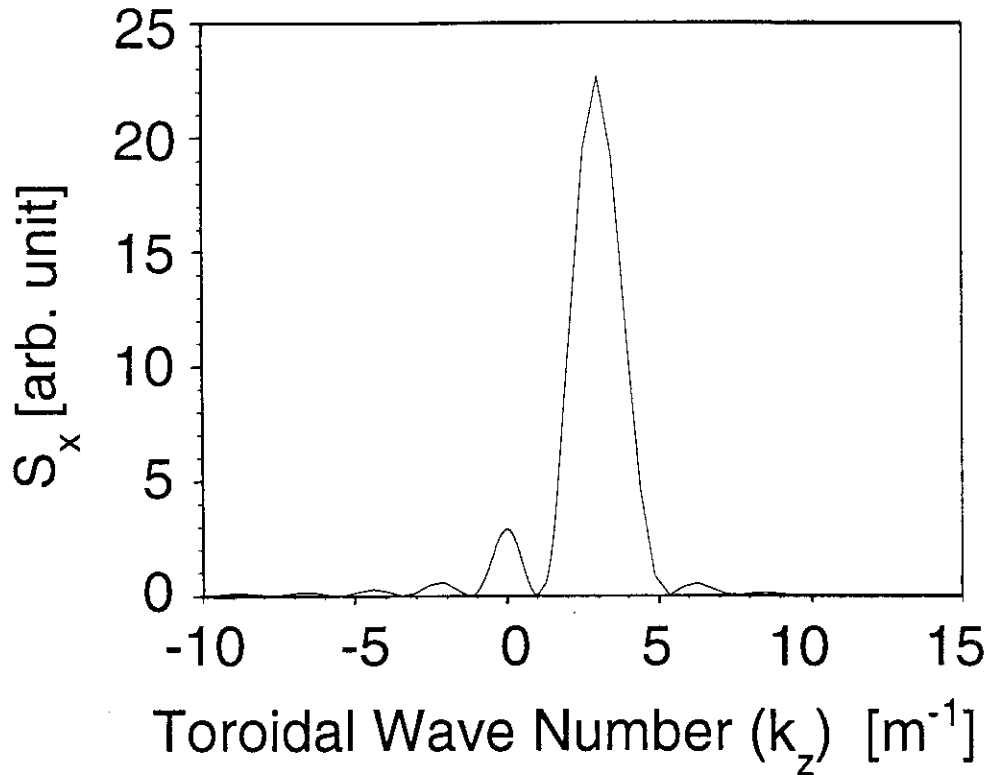


Fig. 2.5.7-3 Coupled N_z spectrum of 8×2 antenna array, $k_z = 1.26 \cdot N_z$.

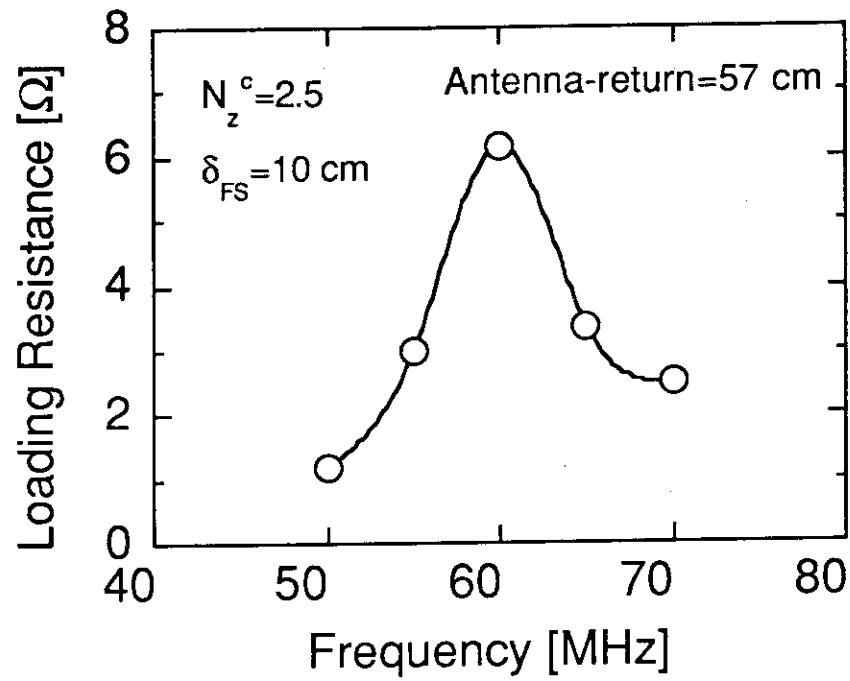


Fig. 2.5.7-4 Dependence of loading resistance on the frequency

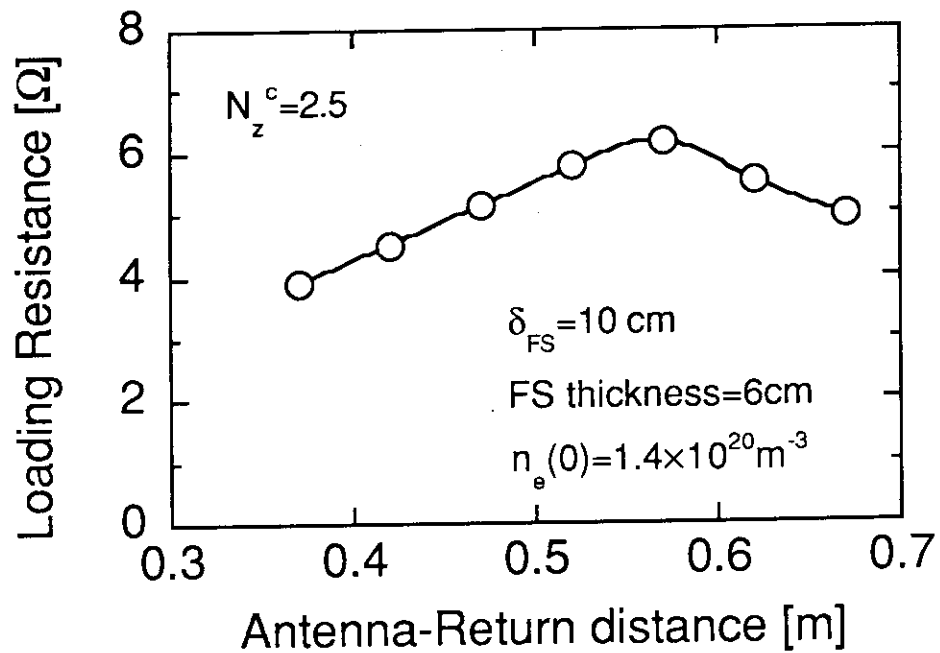


Fig.2.5.7-5 Dependence of coupling on the distance between the antenna and the return wall

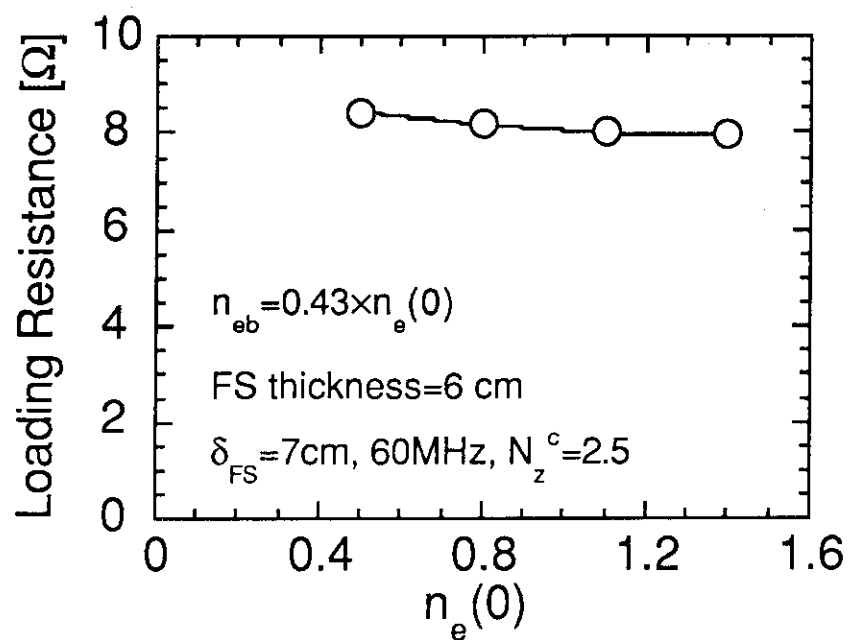


Fig.2.5.7-6 Dependence of the loading resistance on the central electron density ($n_e(0)$).

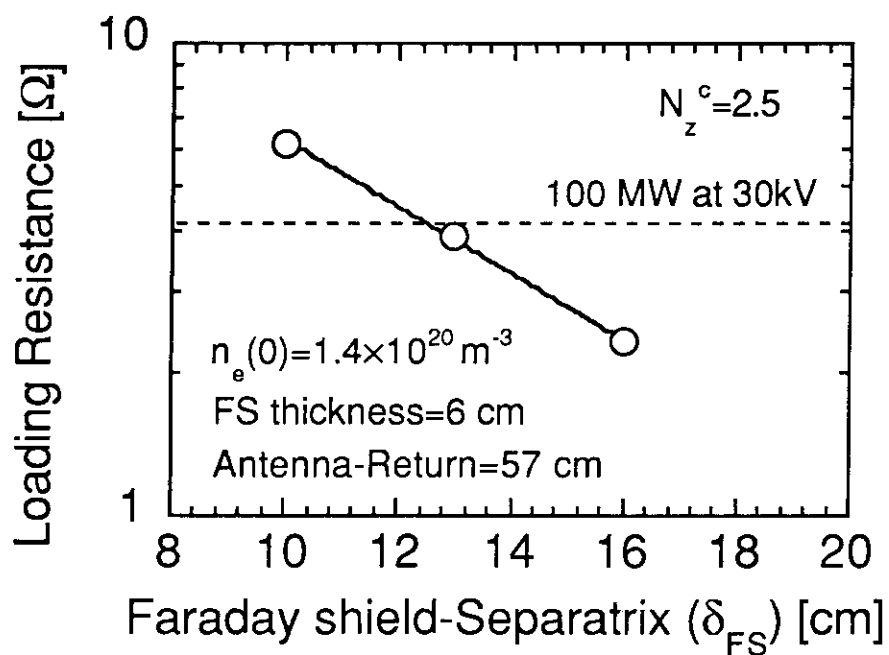


Fig.2.5.7-7 Dependence of the loading resistance on separatrix-Faraday shield distance.

2.5.8 Summary

- (1) Optimum frequency for the high frequency scenario with the in-port antenna of midplane launching is 60 ± 2.5 MHz.
- (2) Antenna box width of 0.95m with perpendicular access, which was the condition proposed by JCT, gives unsatisfactory performance for FWCD.
- (3) Combination of two antenna plugs installed in adjacent tangential ports, of which directions are opposite each other, enables 3m of total toroidal width of an antenna array within framework of the in-port antenna concept.
- (4) 8 strap antenna with 3m total toroidal width gives γ of $0.19 \times 10^{20} \text{AW}^{-1} \text{m}^{-2}$ by 1-D calculation ($0.33 \times 10^{20} \text{AW}^{-1} \text{m}^{-2}$ by 2-D calculation) at $N_z^c = 2.5$ and 60MHz and also good controllability in heating.
- (5) In OH conditions, N_z^c value optimum for CD is about 4.5. If current drive is required from the OH phase, dynamical control of the toroidal phasing (N_z^c) is necessary. If not, the ion heating mode automatically shifts over the current drive mode in a course of a discharge, setting N_z^c to be 2.5 at 60MHz.
- (6) Enhanced power absorption by the triton tail formation is important for $N_z \leq 2$. The antenna current spectrum should be as sharp as possible to avoid enhanced ion absorption due to the tail formation and to maximize the current drive efficiency.
- (7) Power absorption and driven current profiles are calculated by the 2D full wave code with ITER plasma equilibrium. Electron power absorption ratio and the current drive efficiency of the 2-D calculation are larger than those of the 1-D calculation because of the outward shift of the magnetic axis and the focusing effect of the wave propagation.
- (8) Conceptual drawing of the 8×2 strap antenna structure (4×2 straps/module) is proposed. The antenna structure is consistent with the radiation shielding and is free from ceramics inside the cryostat employing two ridged waveguide supports per line for the internal conductor.
- (9) $\lambda/2$ resonance of the antenna may be necessary to have a good coupling performance. In this condition, the loading resistance is $\sim 6\Omega$ for $\delta_{FS} = 10\text{cm}$ and $\sim 3\Omega$ for $\delta_{FS} = 15\text{cm}$ with

$\lambda_e=2\text{cm}$, where the loading resistance over 4.2Ω is demanded for 100MW injection with 6 ports assuming the stand-off voltage of 30kV.

3. Concluding Remarks

Detailed study on the current drive performance has been made both for the in-blanket antenna and the in-port antenna. The low frequency scenario with the in-blanket antennas suffers from the $N_{||}$ upshift because of a weak damping per pass and an insufficient directivity even with the 18 strap array. The current drive efficiency cannot be so high. γ is $0.27 \times 10^{20} \text{AW}^{-1} \text{m}^{-2}$ for the standard CD conditions ($q_a=5$, $q_0=1$ and $\alpha_N=0.15$) including the antenna current spectrum. γ may be improved with increasing safety factor at the expense of the damping per pass but γ is at most $0.36 \times 10^{20} \text{AW}^{-1} \text{m}^{-2}$ for $q_a=7$, $q_0=2.5$ and $\alpha_N=0.15$. On the other hand, the high frequency scenario shows better current drive performance because of a strong damping per pass and much more narrow current spectrum, in spite of a loss of certain amount of power to ions ($\sim 20\%$). γ of $0.4 \times 10^{20} \text{AW}^{-1} \text{m}^{-2}$ is obtained for the standard CD conditions ($q_a=5$, $q_0=1$ and $\alpha_N=0.15$) including the antenna current spectrum.

The in-port antenna with 'tangential access' is proposed, aiming at compatibility of high performance on the current drive and easy maintenance. The high frequency scenario is employed for the in-port antenna inevitably. 8 strap array with total toroidal extension of about 3m, which may be a minimum requirement for efficient current drive in ITER, is possible with reasonable power injection capability. A total injection power of 100MW is possible using 6 ports with $\delta_{FS} \sim 12\text{cm}$, $\lambda_e=2\text{cm}$ and the stand-off voltage of 30kV. A value of γ is calculated to be $0.19 \times 10^{20} \text{AW}^{-1} \text{m}^{-2}$ by 1-D code or $0.33 \times 10^{20} \text{AW}^{-1} \text{m}^{-2}$ by 2-D code taking account of realistic ITER plasma equilibrium in ignition. Thus the current drive efficiency comparable with that of the in-blanket antenna using the low frequency scenario can be obtained. More detailed design study on such a promising in-port antenna is to be carried out continuously in 1995.

$\lambda_e=2\text{cm}$, where the loading resistance over 4.2Ω is demanded for 100MW injection with 6 ports assuming the stand-off voltage of 30kV.

3. Concluding Remarks

Detailed study on the current drive performance has been made both for the in-blanket antenna and the in-port antenna. The low frequency scenario with the in-blanket antennas suffers from the $N_{||}$ upshift because of a weak damping per pass and an insufficient directivity even with the 18 strap array. The current drive efficiency cannot be so high. γ is $0.27 \times 10^{20} \text{AW}^{-1} \text{m}^{-2}$ for the standard CD conditions ($q_a=5$, $q_0=1$ and $\alpha_N=0.15$) including the antenna current spectrum. γ may be improved with increasing safety factor at the expense of the damping per pass but γ is at most $0.36 \times 10^{20} \text{AW}^{-1} \text{m}^{-2}$ for $q_a=7$, $q_0=2.5$ and $\alpha_N=0.15$. On the other hand, the high frequency scenario shows better current drive performance because of a strong damping per pass and much more narrow current spectrum, in spite of a loss of certain amount of power to ions ($\sim 20\%$). γ of $0.4 \times 10^{20} \text{AW}^{-1} \text{m}^{-2}$ is obtained for the standard CD conditions ($q_a=5$, $q_0=1$ and $\alpha_N=0.15$) including the antenna current spectrum.

The in-port antenna with 'tangential access' is proposed, aiming at compatibility of high performance on the current drive and easy maintenance. The high frequency scenario is employed for the in-port antenna inevitably. 8 strap array with total toroidal extension of about 3m, which may be a minimum requirement for efficient current drive in ITER, is possible with reasonable power injection capability. A total injection power of 100MW is possible using 6 ports with $\delta_{FS} \sim 12\text{cm}$, $\lambda_e=2\text{cm}$ and the stand-off voltage of 30kV. A value of γ is calculated to be $0.19 \times 10^{20} \text{AW}^{-1} \text{m}^{-2}$ by 1-D code or $0.33 \times 10^{20} \text{AW}^{-1} \text{m}^{-2}$ by 2-D code taking account of realistic ITER plasma equilibrium in ignition. Thus the current drive efficiency comparable with that of the in-blanket antenna using the low frequency scenario can be obtained. More detailed design study on such a promising in-port antenna is to be carried out continuously in 1995.

Acknowledgment

We would like to express our appreciation to Dr. G. Bosia of the ITER Joint Central Team (JCT) and Dr. T. Nagashima of JAERI (a former division head of JCT) for support and cooperation throughout this work. Thanks are also due to members of JAERI Home Team Design Group for helpful discussion. This work was done as a part of the ITER design task (Task agreement number: G 51 TD 02, ID number: D89).

References

- [1] V. Parail, et al., ITER Documentation Series, No. 32, IAEA, Vienna (1991).
- [2] V. P. Bhatnagar, et al., Nucl. Fusion, **34** (1994) 886.
- [3] The ITER Director, "Auxiliary Heating and Current Drive Systems" (ITER TAC Meeting No.4, January, 1994).
- [4] G. Bosia, et al., Proc. 15th Int. Conf. on Plasma Phys. and Controlled Nuclear Fusion Research (Seville, 1994), IAEA, Vienna, paper IAEA-CN-60/E-P-8 (to be published).
- [5] H. Kimura, et al., "Conceptual Design of Fusion Experimental Reactor (FER/ITER) -Ion Cyclotron Wave System-", Japan Atomic Energy Research Institute Report, JAERI-M 91-094 (1991).
- [6] T. Nagashima, et al., Fusion Engineering and Design, **5** (1987) 101.
- [7] T. Fujii, et al., Fusion Engineering and Design, **19** (1992) 213.
- [8] T. Fujii, et al., Proc. 16th Symp. on Fusion Technology, (London), **2** (1990) 1171.
- [9] T. Fujii, et al., Proc. 14th Symp. on Fusion Engineering, (San Diego), **1** (1991) 107.
- [10] S. Moriyama, et al., Proc. 17th Symp. on Fusion Technology, (Rome), **1** (1992) 584.
- [11] M. Saigusa, et al., Fusion Engineering and Design, **24** (1994) 47.
- [12] T. Fujii, et al., Fusion Engineering and Design, **26** (1995) 377.
- [13] D. A. Ehst, et al., Nucl. Fusion, **31** (1991) 1933.
- [14] A. Fukuyama, S. Nishiyama, K. Itoh and S.-I. Itoh, Nucl. Fusion, **23** (1983) 1005.
- [15] K. Hamamatsu, M. Azumi, Y. Kishimoto et al., Nucl. Fusion, **29** (1989) 147.
- [16] A. Fukuyama, K. Itoh and S.-I. Itoh, Comp. Phys. Rep. **4** (1986) 137.
- [17] T. Nakazato, et al., Nucl. Fusion, **32** (1992) 1209.
- [18] Y. Kishimoto, et al., Nucl. Fusion, **27** (1987) 550.
- [19] R. Prater, et al., Proc. IAEA Tech. Comm. Meeting on RF Launchers for Plasma Heating and Current Drive, JAERI-Conf 94-001 (JAERI, 1994) 125.
- [20] H. Kimura, et al., "Design Study of an ICRF Coupler for JT-60", Proc. 4-th Joint Varenna-Grenoble Int. Symp. on Heating in Toroidal Plasmas (Rome), **2** (1984) 1128.
- [21] M. Saigusa, et al., Proc. IAEA Tech. Comm. Meeting on RF Launchers for Plasma Heating and Current Drive, JAERI-Conf 94-001 (JAERI, 1994) 49.